Fatigue behaviour of metallic components obtained by topology optimization for additive manufacturing

Bernardo Garrett Neuparth Moura de Oliveira

Dissertation submitted to

Faculdade de Engenharia da Universidade do Porto

Masters Dissertation

Supervisor: Prof. Abílio de Jesus

Co-Supervisor: Dr. João Pereira

Co-Supervisor: MSc. Felipe Fiorentin

U. PORTO
FEUP FACULDADE DE ENGENHARIA
UNIVERSIDADE DO PORTO

Integrated Masters in Mechanical Engineering

June 2019

Resumo

A tecnologia do fabrico aditivo tem vindo a assistir a um desenvolvimento exponencial e diversas técnicas têm vindo a ser associadas a esta com vista à obtenção de melhores propriedades mecânicas. Uma das vertentes mais indicadas a esta evolução é o fabrico aditivo metálico uma vez que as aplicações decorrentes desta tecnologia pressupõem exigências mecânicas superiores, porém estão associadas a um elevado custo. A otimização topológica representa uma oportunidade de economizar material associando-o diretamente às forças a que uma peça é submetida.

A otimização topológica permite a utilização de variados algoritmos sendo que, nesta dissertação, a opção foi seguir o *Solid Isotropic Material with Penalization* com o intuito de obter uma peça mais leve e adequada à aplicação da mesma. Os resultados obtidos foram então suavizados para diminuir as zonas de concentração de tensões. Com a ajuda de software de simulação de fabrico aditivo foi também possível simular as distorções e tensões residuais resultantes da construção durante e após o processo de fabrico. É também realizada uma análise de fadiga que conjuga, não só, a simulação da peça em softwares de elementos finitos como a simulação da construção da peça. Foi possível demonstrar que através de uma criteriosa seleção dos parâmetros de processamento aditivo, é possível obter tensões residuais favoráveis à resistência à fadiga do componente mecânico otimizado.

Abstract

The world have, on recent times, witnessed an exponential development of the Additive manufacturing technology. At the same time, different techniques have been associated to this technology in order to achieve better mechanical properties. One of the most suitable fields (modes) on this evolution is the metal addictive manufacturing, since the enforcements resulting of this technology imply superior mechanical requirements, nevertheless it involves high costs. The topology optimization represents an opportunity to save material associating it directly to the forces that a part is submitted to.

Topology optimization allows the use of various algorithms and, in this dissertation, the option was to follow the Solid Isotropic Material with Penalization in order to obtain a lighter piece and suitable for its application. The obtained results were then smoothed to reduce the stress concentration areas. With the help of additive manufacturing simulation software, was also possible to simulate distortions and residual stresses resulting from the building during and after the manufacturing process. In this work a fatigue analysis that combines not only the simulation of the part in finite element software as the simulation of the part construction is carried out. It was demonstrated that controlling the additive manufacturing parameters it is possible to generate favourable residual stresses that produced better fatigue performance of the bracket selected.

Acknowledgements

I would like to thank my thesis advisor Prof. Abílio de Jesus of the Faculty of Engineering at University of Porto. He consistently allowed this thesis to be my own work and steered me in the right direction providing guidance and support, as well as recommendations and new ideas to improve this dissertation.

I would also present the expression of my sincere gratitude to Dr. João Carlos Pereira for his support and availability during the thesis. The knowledge and experience shared was fundamental for the competition of this dissertation.

I am also very grateful to Felipe Fiorentin for his time and experience provided. Our discussions, in order to overcome difficulties, were essential for this thesis. I would also thank his essential contribution for the additive manufacturing simulation.

To Tiago Silva who was very helpful during this process, specially, during the topology optimizations.

To Roya Darabi for her help for the help to achieve a good method for the fatigue analysis.

I am also very thankful to my parents who always showed how much they believe and support me in this final step of my master degree.

To my girlfriend, a special appreciation for the care, support and concern at all times.

I would also thank my friends for their help and care during the process.

The project ADD.Strength entitled “Enhanced mechanical proprieties in additive manufactured components”, co-financed by COMPETE 2020 through FEDER and FCT funds, is fully acknowledged.

Contents

List of tables

List of Figures

Abbreviations

AM – Additive Manufacturing

BESO – Bidirectional Evolutionary Structural Optimization

DED - Directed Energy Deposition

EBM – Electron Beam Melting

ESO - Evolutionary Structural Optimization

FCT – Fundação para a Ciência e a Tecnologia

FCRC - Flight Crew Rest Compartments

FE – Finite Element

FEM - Finite Element Analysis

HCA - Hybrid Cellular Automata

HCF – High Cycle Fatigue

INEGI – Instituto de ciência e inovação em engenharia mecânica e engenharia industrial

LCF – Low Cycle Fatigue

MAM – Metal Additive Manufacturing

MMA - Method of Moving Asymptotes

MPa – Mega Pascal

OC - Optimality Criteria

PBF – Powder Bed Fusion

R – Stress Ratio

R% - Reduction percentage

SIMP - Solid Isotropic Material with Penalization

SL – Sheet Lamination

SLM - Selective Laser Melting

SLS – Selective Laser Sintering

SQP – Sequential Quadratic Programming

SR – Stress Range

SS – Stainless Steel

STEP - Standard for the Exchange of Product model data

STL – Standard Triangle Language

TO – Topology Optimization

UTAF - Unidade de Tecnologias Avançadas de Fabrico

Symbol	**Description**	**Unit**
$\mathbf{T}$	Temperature	K
$\mathbf{t}$	Time	s
$\mathbf{q}$	Heat flux	W/m^2
$\mathbf{r}$	Reference coordinate	
$\mathbf{C_p}$	Material specific heat capacity at constant pressure	Kj/KgK
$\mathbf{Q}$	Body heat source	J
$\boldsymbol{\rho}$	Material density	Kg/m^3
$\boldsymbol{\varepsilon_e}$	Elastic strain	
$\mathbf{Q_{CD}}$	Heat conduction loss	J
$\mathbf{Q_{CV}}$	Heat convection loss	J
$\mathbf{Q_R}$	Heat radiation loss	J
$\mathbf{n}$	Vector normal to surface	
$\mathbf{h}$	Heat transfer coefficient	W/m^{2}K
$\boldsymbol{\sigma}$	Stefan-Boltzmann constant	W/m^{2}K^4
$\boldsymbol{e}$	Emissivity	
$\mathbf{T_0}$	Environment temperature	K
$\mathbf{T_2}$	Surface temperature	K
$\mathbf{c}$	Strain energy	J
$\mathbf{K}$	Stiffness	N/m
$\mathbf{U}$	Displacement vector	m
$\mathbf{F}$	Loading vector	N
$\mathbf{V^*}$	Target volume	m^3
$\boldsymbol{V_e}$	Design volume	m^3
$\boldsymbol{u^e}$	Element displacement vector	m
$\boldsymbol{k_0\,;\,k^e}$	Initial and Element stiffness matrixes	N/m
$\boldsymbol{p}$	Penalty factor	
$\boldsymbol{x_e}$	Design variable	
$\boldsymbol{N_e}$	Number of elements	
$\boldsymbol{i}$	Center-to-center distance	
$\boldsymbol{\gamma}$	Small positive number to avoid division by zero	
$\boldsymbol{H_{ei}}$	Weight factor	
$\boldsymbol{\lambda}$	Lagrangian multiplier on fixed amount of material	

$\boldsymbol{\alpha}$	Lagrangian multiplier on equilibrium constraint	
$\boldsymbol{\beta}$	Lagrangian multiplier on bound’s constraint	
L	Resulting stationary point	
$\mathbf{S^{vm}}$	Von Mises stresses	MPa
$\mathbf{S_a}$	Alternating stress	MPa
$\mathbf{S_m}$	Mean Stress	MPa
$\mathbf{S_{min}}$	Minimum Stress	MPa
$\mathbf{S_{max}}$	Maximum Stress	MPa
N	Fatigue life	
$\mathbf{N_D}$	Fatigue limit cycles	
$\mathbf{D_i}$	Damage	
$\mathbf{S_f}$	Fully reversed fatigue strength	MPa
$\mathbf{S_0}$	Yield Strength	MPa
$\mathbf{S_u}$	Ultimate tensile strength	MPa
$\boldsymbol{\varepsilon_a}$	Elastic strain	
E	Young Modulus	GPa
$\boldsymbol{\varepsilon_p}$	Plastic strain	
n’	Cyclic strain hardening exponent	
$\mathbf{K_1}$	Axial Stiffness	N/m
$\mathbf{K_{2-3}}$	Shear Stiffness	N/m
$\mathbf{K_{5-6}}$	Rotational Stiffness	N/m
D	Flexibility of the fastener	
$\mathbf{t_1, t_2}$	Thickness of plate 1,2	mm
a	Coefficient depending on fastener type	
$\mathbf{b_1,b_2}$	Coefficients depending on the joint plates material	
L	Length	mm

1 Introduction

Nowadays, the modern high-tech industries claim the fundamentals of the next industrial revolution called Industry 4.0. This revolution presupposes a reduction of waste while maximizing the material usage, among other goals. By introducing two trends as additive manufacturing (AM) and topology optimization (TO), enables the accomplishment of these goals.

Since the metals are the most frequent materials in engineering, many efforts have been made to reach mechanical properties close to the conventionally counterparts. Right now, the additive manufacturing industry has much to develop to meet the industry's expectations. Therefore, problems associated with costs, production speed, mechanical behaviour, surface quality and homogeneous microstructure have to be resolved [1].

This technology allows a faster production of prototypes, finished products and possible enhancements of the design of certain products; also, it may lead to lower stock needs of raw materials and reduction of costs associated with transports and logistics.

Structural optimization improves even more additive manufacturing benefits since there is a symbiosis between these two processes. Both of these methods aim at providing freedom to the designers and the topology optimization algorithms are adapted to simulate structures with complex shapes optimizing them to the desired mechanical constraints. Light weight designs are a reality when these technologies are combined, reducing the amount of required work but increasing the importance of the product development because it will be a more iterative work, regarding the stress analysis and the possible changes that can occur. The Figure 1 illustrates this new product development panorama [2].

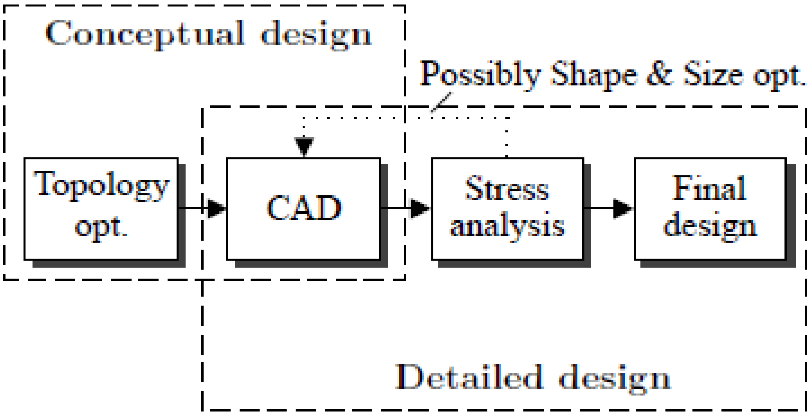

Figure 1 - Product development process [2].

1.1 Project Framework and motivation

This research topic is related with the fatigue behaviour assessment of metallic components obtained by topology optimization for additive manufacturing. The dissertation integrates a FCT project related with metal additive manufacturing, namely the ADD.Strength project entitled "Enhanced mechanical properties in additive manufactured components". ADD.Strength is a funded FCT project integrated in UTAF unity of INEGI. This project aims at investigating different configurations, such as residual stresses resulting from the part construction and fatigue behaviour of optimized components for additive manufacturing trying to quantify stress concentrations and their effect on fatigue resistance; analyse residual stress generated during additive manufacturing processes and their influence on the mechanical properties. Ultimately, the ADD.Strength project aims at designing additively produced components with favourable (e.g. compressive) residual stresses for fatigue behaviour improvement. Topological optimization generally leads to slender components with notches. Notches are generally fatigue hot spots, so the generation of compressive residual stresses at those hot spots by selecting appropriate AM build strategies will be a valuable outcome of the research.

1.2 Project objectives

This dissertation has the following objectives:

- State of the art characterization about topology optimization processes related to fatigue resistance and metal additive manufacturing;
- Definition of a case study for topological optimization using finite-element analysis;
- Additive manufacturing building simulation of the resulting parts from topology optimization and fatigue analysis under cyclic loading;
- Analysis and discussion of the results.

1.3 Layout of the dissertation

The document layout follows a chapter structure and the references are presented after the last chapter. In Chapter 2, a literature review regarding the metal additive manufacturing, structural optimization and fatigue analysis is addressed. In Chapter 3, the methodology used during the topology optimization, the treatment of the extracted file, reverse engineering as well as the final analysis, both static and fatigue is discussed. In Chapter 4, the additive manufacturing simulation of the designed part is performed. The principles of the software, as well as its input parameters are presented. In Chapter 5, results of the static and fatigue analysis as well as the contribution of the AM simulation results, obtained in the previous chapter, are presented. The conclusions and future works are shown in Chapter 6, where considerations towards the results of the topology optimization and the impact of the simulations on the stress distribution of the new parts are commented. In addition, conclusions about the fatigue behaviour of the case study component are summarized.

2 Background Theory

2.1 Metal Additive manufacturing

Additive manufacturing does not cover a single, but a range of different technologies. These technologies not only can explore the freedom of new designs but also can process pieces using different materials. Currently, it has been mostly used with polymers and metals, despite composites and ceramics are increasing their relevance too.

The focus of this thesis is the Metal Additive Manufacturing (MAM). The current processes for metals encompass methods such as Binder Jet, Powder Bed Fusion (PBF), Sheet Lamination (SL) and Directed Energy Deposition (DED) processes.

Powder Bed Fusion is one of the most popular MAM process. It uses a heat source to selectively melt thin layers of metal powder welding one layer to the previous, forming a solid component. The heat source (laser or electron beam) differentiates this category into Selective Laser Melting (SLM) or Selective Laser Sintering (SLS) and Electron Beam Melting (EBM).

2.1.1 SLM

One of the most MAM used technologies is the Selective Laser Melting (SLM) which offers the opportunity to generate components with complex shapes, time saving and versatility. During this process, a layer of powder is deposited onto a substrate and is spread by a wiper, roller or blade. After that, a laser melts this powder according to specific parameters (laser power, beam diameter, modulation and scan strategy) established by the software. The melted material solidifies and retracts. After that, a new powder layer is deposited. This process is repeated layer upon layer until the part is completed. The remaining (unmelted) powder is removed from the building chamber and can be recycled[3-5].

The first SLM machine was developed by Fockele and Schwarze (F&S) in cooperation with Fraunhofer institute in 1999 and it was commercialized by MCP HEK Gmbh in 2004. Figure 2 presents a diagram for a better understanding of the SLM process. For most machines, one of the limitations has been the part size restriction to 250 x 250 x 325 mm^3 Recently, machine manufactures are trying to increase build rates and volumes[6].

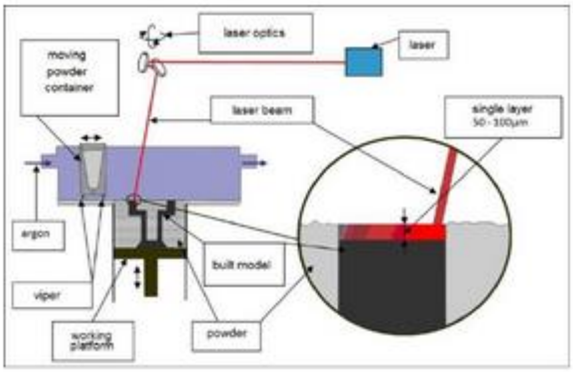

Figure 2 - Schematics of a SLM Machine[7]

The process parameters are the key factor to distinguish the way how some parts are built. The main parameters, which will be explained in sequence, are [4, 5, 7]:

- Laser type
- Atmosphere
- Temperature
- Powder
- Other process parameters

Laser type

The selection of the laser type is crucial since the absorption of each type of laser is different for distinct materials. Each type of laser has a different wavelength from each other and the absorption varies, as the Figure 3 illustrates.

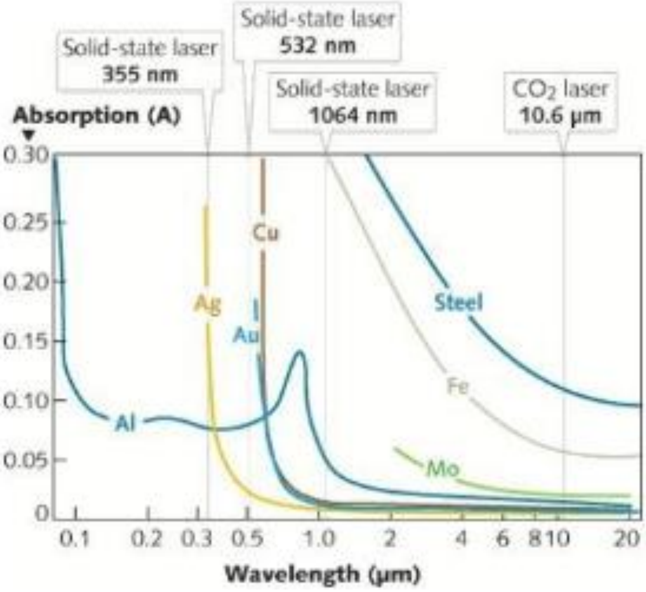

Figure 3 – Laser Absorption for several materials in different wavelengths[7]

Atmosphere

The risk of oxidation is very high for high temperatures with the presence of oxygen. This factor can affect the mechanical properties of the part. Therefore it is important to apply highly pure gases as well as a careful selection of the chemical composition of the atmosphere to avoid oxidation on vulnerable materials. The oxidation can lead to the appearance of inclusions. Other type of problems are the appearance of pores occasioned by particles of oxygen and carbon monoxide that creates gas bubbles, which cannot be expelled. For protecting the SLM processes nitrogen, helium or argon are often used.

Temperature

The chamber temperature can be set between 22°C and 300°C, depending on the machine. The properties of metal like the flowability and layer creation improve with the increase of chamber temperature.

The base plate can be preheated up to 400ºC to reduce thermal gradients and internal stresses[8]. The powder can be also preheated with the same aims [9].

Powder

The size of the powder particles recommended is between the 20µm and 100µm and the grain cannot be bigger than the layer thickness. Smaller particles are more easily melted, while the opposite can lead to lack of fusion, resulting in pores or heterogeneity. For a better deposition, particles must be spherical in order to avoid gaps that can also cause pores. The use of recycled powder tends to increase the particles diameter and loose spherical formats due to the micro fusions between the particles and other contaminations.

The format and size of the particles are highly dependent of the manufacturing method used to obtain the powder.

Other process parameters

There are other important parameters such as the laser power, scanning speed, hatch spacing and layer thickness that have to be optimized for proper process performance. These parameters are illustrated in the Figure 4. The laser power can be set between 200W and 1 kW. Other parameters must be set, just as beam diameter, laser modulation, scan strategy and contour strategy.

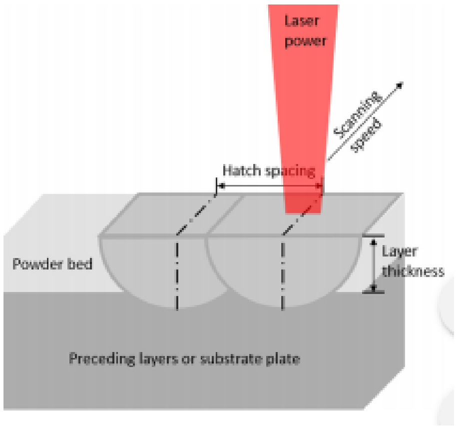

Figure 4- Process parameters: Laser Power, Hatch spacing, Scanning speed and Layer thickness[4]

Investigations related to the mechanical properties of the AM parts [10] show that, comparing the microstructure of the Ti6Al4V alloy produced by SLM with the wrought material, the elongation is a little bit higher for wrought alloy and the residual stresses for the SLM technology must be taken into consideration. Parts produced by SLM are near full density and have good mechanical properties, the thermal stresses that these parts are subjected can cause distortions and cracks. During SLM, balling phenomenon may occur, which can be divided into ellipsoidal balls with dimensions of about 500 µm and spherical balls with dimension of about 10 µm, which can increase the surface roughness that leads to post-treatment such as polishing. This balling phenomenon occurs when the liquid phase breaks up into a row of spheres due to insufficient input laser energy density. The trapped gases, unmelted powder and oxidized particles lead to porosity in the component.

SLM manufacturing process allows a wide range of materials processing such as titanium alloys (e.g.Ti-6Al-4V), stainless steel, nickel-based alloys (Inconel) and aluminium alloys [11, 12].

2.1.2 EBM

Alternatively to SLM, the Electron Beam Melting (EBM) can also be used as a MAM process. This takes place in a vacuum chamber to avoid the interactivity between the electrons and the atmosphere. This vacuum environment also keeps the chemical composition of the metals which is very useful for reactive materials. The power of the electron beam gun could be adjusted by changing the voltage and the beam diameters. This process involves preheating of the powder which reduces the temperature gradient and consequently avoids distortions and cracks.

The EBM system was developed by Arcam. It is divided in two parts. The upper column, which contains the electron generating part at 60 kV accelerating potential, and the build chamber, which includes the build tank, powder feeders and raking systems. At present time the focus of this technology has been the production of titanium near-net-shape parts for medical implants and aerospace applications. The benefits of this process using titanium are easily understandable due to high reactivity of this material [5, 6].

2.2 Integration of Topology Optimization with Additive Manufacturing

Topology optimization and Additive Manufacturing are independent but there is an interest of matching these technologies for several reasons:

- The results of Topology Optimization are very complex and could be almost impossible to reproduce using traditional manufacturing processes.
- The use of material is an inherent characteristic of the fabrication cost of additive manufacturing and it is possible to reduce this cost due to Topology Optimization.

Despite these advantages, the topology optimized parts, as well as the majority of the AM parts, require supports, which are difficult to remove. The material cost and other post-fabrication operations are factors that must be considered. The minimization of the support structures has been also studied using new sensitivities approaches [13].

Smith *et al* [14] found some geometrical discrepancies between an optimized solution and its respective printed part, which suggest that many parameters of additive manufacturing are not considered during the topology optimization and most of them have a high progression margin.

2.2.1 Metal Additive Manufacturing Process Simulations

The majority of the simulation studies are focused on the SLM process, with EBM being given less attention. The scope of the majority of studies is the temperature field assessment [15].

Full-build simulation of laser powder bed fusion processes enables analysis of thermal-induced stresses and distortion from the melting of the powder feedstock by the laser. Recently, several commercial codes have given users an increasing number of tools to aid in understanding laser powder bed fusion builds, including tools from 3DSIM(Flex and ExaSIM), MSC (Simufact Additive), Dassault Systemes (3DEXPERIENCE), Autodesk (Netfabb) and ESI GROUP[16].

For simulating the mechanical and thermal behaviour from AM processes, it is necessary to use a non-linear finite element method to convert the physics equation (energy balance to thermal problems and stress equilibrium for mechanical problems) to a weak formulation that results in a nodal solution vector of temperatures or displacements.

The non-linearity is explained, for the mechanical part, by the presence of plasticity and temperature dependence. For the thermal part, the temperature dependency of the material properties unleashes this non-linearity.

Assuming a unidirectional relationship between the thermal and mechanical behaviours that is often applicable to AM processes, the decoupled or weakly couple modelling methodology is used.

The governing equation (Eq. 2.1) for thermal equilibrium is the energy balance and the boundary conditions depend on the heat input model and the boundary losses associated with convection, radiation, fixturing losses and powder considerations has to be considered.

$$\rho C_p \frac{dT}{dt} = -\nabla q(r,t) + Q(r,t) \tag{2.1}$$

where T is temperature, t is time, q is the heat flux, r is the reference coordinate, C_p is the heat capacity at constant pressure, ρ is the material density and the body heat source is Q.

For the mechanical model (Eq. 2.2), the governing equation is the stress equilibrium equation:

$$\nabla * \sigma = 0 \tag{2.2}$$

For elastic problems the stress and elastic strain fields are related by (Eq. 2.3):

$$\sigma = C\epsilon_e \tag{2.3}$$

where C is the fourth order material stiffness tensor and ϵ_e is the elastic strain[17].

The main challenges of these simulations can be abbreviated in the following issues:

- Material addition
- Heat input
- Thermal Losses
- Distortion and Residual Stresses
- Temperature Dependent Material Properties
- Microstructural Changes
- Simulation Time

Material Addition

Introducing new material into the model entails new equations. These equations can be accounted by two methods: The Quiet method and the Dead-Alive method. The Quiet method uses the outset solution matrices and apply material scaling factors in order to remove and add material into the model. The Dead-Alive method adds new equations to the matrices.

Heat Input

The heat source for the AM processes can be a laser, electronic beam or an arc torch and it is the principal source of thermal strains, residual stresses and distortion due to the generated thermal gradients. The main difficulty associated with this challenge is the evaluation of the amount of heat absorbed and reflected by the base material.

Thermal Losses

The thermal losses are usually associated with thermal conduction, free and forced convection and thermal radiation. These factors are the keys to control the thermal gradients, respecting the first law of thermodynamics. The thermal conduction is the main task of a thermal finite element model. The convection is normally calibrated by analytical means and for the radiation it is used a FE technique for avoiding non linearities.

The general energy balance represented below (Eq. 2.4) in a closed system without heat generation, as well as the boundary conditions for the free surfaces of the part.

$$q \ = Q_{CD} + Q_{CV} + Q_R \tag{2.4}$$

where q, Q_{CD}, Q_{CV} and Q_R are the heat quantities for heat flux, conduction, convection and radiation losses, respectively, and the boundary conditions (Eq. 2.5),

$$k\frac{\partial T}{\partial n} - \ \dot{q}_s + h(T - T_0) + \sigma e(T^4 + T_2^4) = 0 \tag{2.5}$$

where n is the vector normal to the surface, $\dot{q}_s$ is the rate of the heat input, h is the heat transfer coefficient, σ is the Stefan-Boltzmann constant and e is the emissivity, T is the point temperature, T_0 is the environment temperature and T_2 is the surface temperature.[15, 17]

Distortion and Residual Stresses

The distortion and residual stresses in additive manufacturing, resulting from rapid heating and cooling cycles, is not completely understood, causing some doubts in the computational model predictions[18]. The thermal gradients created by the application of high energy on cool surfaces will incur thermal expansion and will create stresses within the part during manufacture, which often exceed the yield strength and can form plastic strains, resulting on distorted parts. The key to avoid this distortion is in the design, where it is possible to predict and reduce distortions and residual stresses. This is an important issue, because if this stage does not prevent these problems, it will increase the manufacturing cost, since will be necessary machining to achieve dimensional accuracy and heat treatment to relieve residual stresses. Finite element modelling can reduce the experimentation to optimize process parameters and reveal the transient thermal and deformation history. The finite element analysis of welding is one of the principal bases of these methods considering the similarities between the processes[19].

Temperature Dependent Material Properties

The most important properties that affect the thermal characteristics of the process are the density, thermal conductivity, specific heat capacity, thermal expansion coefficient and emissivity. These properties are used during a mechanical analysis either coupled or uncoupled with thermal analysis and can affect the residual stresses and distortion. These material properties reveal temperature dependence and are the source of non-linearity of the thermal model. Eliminating this temperature dependence leads to a faster convergence of the model despite being a worst reproduction of the real phenomenon.

Microstructural Changes

Additive manufacturing generated microstructures are often more complex than the conventionally processed counterparts. This happens due to the introduction of spatially and temporally mobile heat sources, which can result in microstructural heterogeneity. The microstructure changes can be grain growth, recrystallization, changes in precipitates, phases and micro-constituents. For modelling this type of changes, it is necessary to develop models that include microstructure of the materials and how they affect the material properties. This predictive modelling of microstructures includes: material property changes, anisotropy in material properties, cooling rate, thermal gradients and phase transformation[20].

Simulation Time

Due to the transient nature of the analysis, computational costs are generally very high. There are some strategies to evade this problem. Applying coarser meshes further away of the heat source, lowering the total number of elements, less time steps and replacing the moving heat source with a heat source applied simultaneously to the whole material layer of simulating multiple layers deposition are some strategies to reduce computational time [15].

2.3 Structural Optimization

The traditional and still dominant way of performing a structural optimization is characterized by:

- Design variables that define the parameters, properties, or elements that will be subject and can be changed during the optimization. These variables form the design space.
- State variables that represents the response of the structures. Structural responses are for example stress, displacement, force, strain, mass, volume. It can be global or related to a load case and it is generally calculated in a finite element analysis (FEA).
- Constraint functions that represent the boundaries, which have to be satisfied on the responses.
- Objective function to classify designs and return the goodness of the design. This function is connected to the responses and is function of the design variables. It must be minimized or maximized [21, 22].

There are three levels of structural optimization (Figure 5). Based on the design variable that is parameterized, the structural optimization can be classified as:

- **Size optimization**: the design variables represents the dimensions that describe the product geometry and are normally discrete variables. This approach is mostly used at the design stage and the variables are generally obtained from a designer or manufacturer's catalogues.
- **Shape optimization:** The product geometry can change during the process once it allows the changes in the boundary of the product geometry. Due to these changes in the geometry, it usually requires an automatic finite elements re-meshing. This optimization can be classified as: direct geometry manipulation and indirect geometry manipulation approaches.
- **Topology optimization:** The design variable represents the connectivity of the domain and can be classified as discrete or continuum approach. For the discrete approach, the design domain is represented by trusses, frames and panels. By varying parameters as width and thickness of individual elements, structures with different sizes and topologies can be represented [23-25].

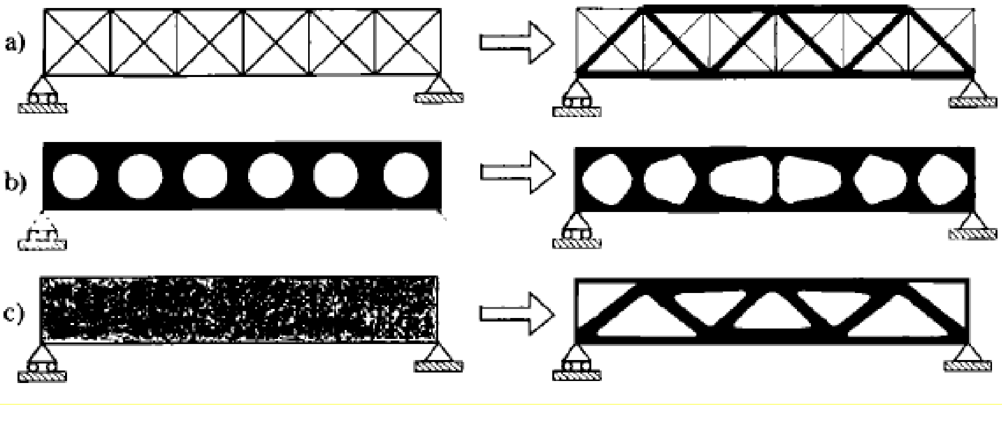

Figure 5 - Categories of structural optimization: a) size optimization; b) shape optimization; c) topology optimization[26]

2.3.1 Topology Optimization

Topology optimization has the particularity of allowing changes not only in the geometry of the structure but also in the connectivity of the components and creating some boundaries, branches and holes amidst these connections.

This main objective of a topology optimization is to yield an optimal design with shape, dimensions and connectivity of a design domain. The designable region is the part of the part where the topology optimization has effect and where the loads and boundary conditions are applied to. For the non-designable regions, the effects of the typology optimization are not materialized.

For a design domain, this technique decides which elements will be solid or void respecting an objective function and different constraints. Topology optimization not only improves structural performances but also thermal properties, fluid flow, electromagnetic applications, among other applications depending on the objective function and if it minimizes or maximizes the objective.

2.3.2 Density based approach

Ideally, the best results for an optimization would be elements consisting of only material or voids. This utopian and simple optimization concerns an 1ISE (also referred as "black-and-white" and "0-1" problem) topology with a discrete variable involving 2^N solutions, where N is the number of elements. In practice, topology optimization problems involves a very large number of finite elements making this type of problems impractical to solve for most models[27, 28]. One example involving four elements of a 1ISE Topology (Figure 6) where the limiting constraint of 0.75 volume fraction gives four solutions. The first one, *b*, is infeasible, the second, *c*, is optimal and the other two, *d* and *e*, are feasible but non optimal. For the 0.5 volume fraction constraint there is only one solution possible, *f*. This solution is the only optimal solution.

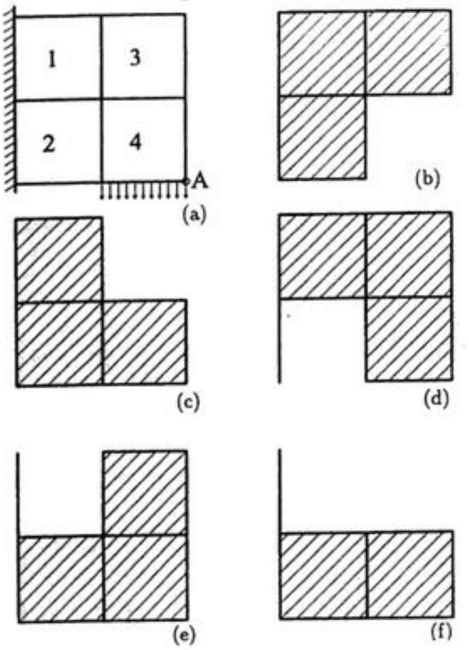

Figure 6 - 1ISE topology optimization results for 0.75 volume fraction constraint [27]

2.3.3 Finite-Element Analysis

The topology optimization methods are based on results of finite element analysis (FEA) to evaluate how a structure behave to different actions like forces, vibration, heat, fluid flow, etc.

FEA requires a mesh to divide the part into finite elements that are assigned to a material and load resulting in a prediction of the structure behaviour.

The importance of the mesh is undeniable on FEM and topology optimization. However, the mesh has a high impact on computation time. This impact gains even more relevance because topology optimization is computationally expensive by itself.

For three-dimensional topology optimization, the most common elements are the tetrahedral and hexahedral. Since the tetrahedral allows a easily mesh generation in less computation time it is more convenient, but sometimes the geometry requires the hexahedral ones for better results [29].

2.3.4 Problem formulation and design parameterization

According to the well-established theory of Bendsoe and Sigmund [26], most of the optimization methods are applied to find solve minimum strain energy design (Eq. 2.6) (also called compliance method) with a volume constraint (Eq. 2.7).

$$\min c = U^T K U = \sum_{e=1}^{n} u^e\, k^e u^e = \sum_{e=1}^{n} (\rho^e)^p u^e k_0 u^e \tag{2.6}$$

$$V^* - \sum_{e=1}^{n} V_e\ \rho^e = 0 \tag{2.7}$$

$$KU = F \tag{2.8}$$

$$0 < \rho_{min} \leq \rho^e \leq 1 \tag{2.9}$$

where the c represents the strain energy, K means the global stiffness matrix U and F the displacement and loading vectors respectively and the imposed volume constraint is characterized by the relative density, ρ^e. V^* is the target volume subjected to a constraint and V_e is the design volume, u^e is the element displacement vector, k^e is the element stiffness matrix after density interpolation and k_0 is the initial stiffness matrix [30].

2.3.5 Solid Isotropic Material with Penalization

Solid isotropic material with penalization (SIMP) is the approach that offer inherent simplicity and favourable complexity and it is abundantly used in modern topology optimization problems. SIMP is a “soft-kill” method and it is used to discretize the design domain dividing it into a grid of N elements (isotropic solid microstructures) each element having a fractional material density[31].

With the density function varying between 1 and 0, it will create a variable density gradient in the new domain. The solid isotropic microstructure with penalization approach represents the intermediate density material with a tensor $K_{ijkl}(\rho) = K^0_{ijkl} \times \rho^p$ where the original stiffness tensor of solid material K^0_{ijkl} is penalized by a density factor.

The penalization factor p forces the algorithm to converge to a solution that contains only a solid or a void by lowering the participation of fractional density elements, encouraging the development of elements with densities close to 1 or 0.

Usually it is used the proportional stiffness model where the penalized density will be essential to define the new penalized stiffness:

$$K_{ijkl}(x) = \rho(x)^p K^0_{ijkl}, p > 1 \tag{2.10}$$

The Figure 7 shows a plot of the penalty function ρ^p and his influence on density and consequently on the penalized stiffness. For p>1 the stiffness will be very low for low density values and it is not recommended.

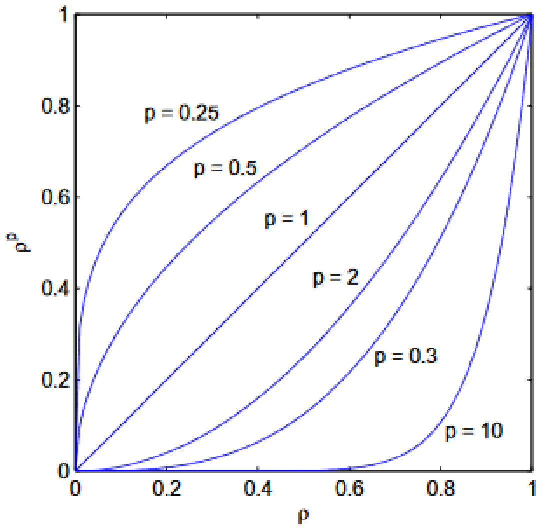

Figure 7 – Influence of the penalty factor on density [32]

The optimization algorithm workflow is represented in the Figure 8. Besides the objective function and restrictions conducted by the FE analysis, it includes the sensitivity analysis, sensitivities filtering and an algorithm for density updating. This represents a topology optimization framework for additively manufactured materials under mechanical load.

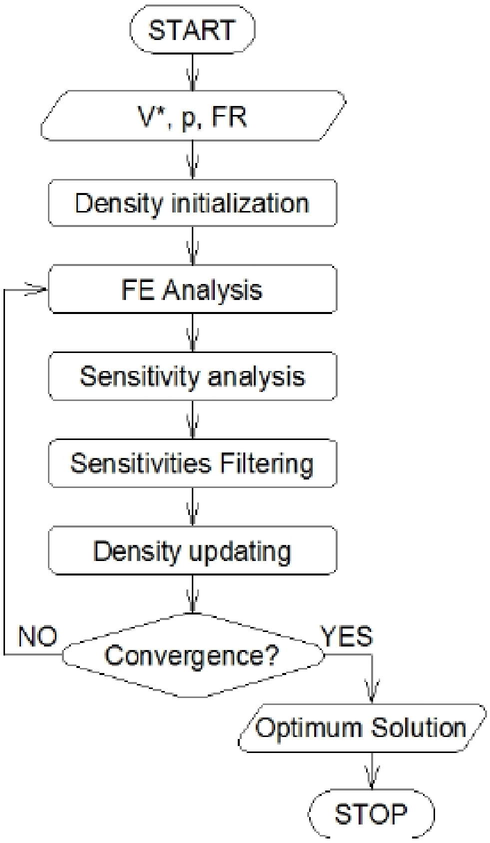

Figure 8 - Flow chart of SIMP algorithm [31]

2.3.6 Sensitivity Analysis

After the finite element analysis, it is necessary to evaluate the sensitivity of each element of the topology optimization. This analysis will determine which parameters and design are the most important ones and change the results of the optimization giving the significance of each variable. This information is very important for the changes during the iterative problem where a small perturbation on a significant variable can easily modify the solution.

According to Choi & Kim [33], the sensitivity of the structure is assumed to be differentiable with respect to the design. This sensitivity analysis can be done directly or using a method for calculating these derivatives when working with a reasonable number of constraints. The derivation of the compliance with respect to the design variable, x_e, is presented in the next equation (Eqs. 2.11; 2.12; 2.13), assuming the nodal force vector independent of the design variable.

$$\frac{\partial c}{\partial x_e} = \frac{\partial}{\partial x_e}\left(U^T F\right) \tag{2.11}$$

$$\frac{\partial F}{\partial x_e} = 0 \overset{F=KU}{\Longrightarrow} \frac{\partial K}{\partial x_e} U + K \frac{\partial U}{\partial x_e} = 0 \Rightarrow K \frac{\partial U}{\partial x_e} = -\frac{\partial K}{\partial x_e} U \tag{2.12}$$

$$\frac{\partial C}{\partial x_e} = U^T K \frac{\partial U}{\partial x_e} \Rightarrow \frac{\partial C}{\partial x_e} = -\, U^T \frac{\partial K}{\partial x_e}\, U \tag{2.13}$$

Decomposing the sum of the element sensitivity (eq. 2.14) results:

$$\frac{\partial c}{\partial x_e} = \sum_{e=1}^{n} \frac{\partial c_e}{\partial x_e} = \sum_{e=1}^{n} -u_e^T \frac{\partial K_e}{\partial x_e}\, u_e \tag{2.14}$$

Calculating each sensitivity independently and not considering any interaction between elements can lead to discontinuous structures, the so called “checkerboard effect”[34].

2.3.7 Sensitivities Filtering

In order to avoid the problems before exposed, modifying the design sensitivity of each element ensures mesh-independency. The original form of the sensitivity filter was presented by Sigmund (1997) [35] and a whole range of filtering methods is thoroughly described again by Sigmund (2007) [36].

The filter modifies the sensitivities as follows(eq. 2.15):

$$\frac{\widehat{\partial y}}{\partial x} = \frac{1}{\max(\gamma, x_e) \sum_{i \in N_e} H_{ei}} \sum_{i \in N_e} H_{ei}\, x_i \frac{\partial C}{\partial x_i} \tag{2.15}$$

where N_e is the set of elements i for which the centre-to-centre distance $\Delta(e,i)$ to element e is smaller than the filter radius, γ is a small positive number to avoid division by zero and H_{ei} is a weight factor defined as [37]:

$$H_{ei} = \max\big(0, r_{min} - \Delta(e,i)\big) \tag{2.16}$$

This modification turns the original densities into physical densities. The sensitivities of the objective function with respect to the physical densities maintains the same except the replace of x_e by $\widetilde{x_e}$.[37-39]

2.3.8 Density updating

After applying the filtering sensitivities, it is necessary to update the sensitivities to solve particular topology optimization problems. These problems are solved by a greater variety of optimization methods such as optimality criteria (OC) methods, hybrid cellular automata (HCA), approximation methods, CONLIN, the method of Moving Asymptotes (MMA), Sequential Quadratic Programming (SQP), more heuristic methods and Ant colony. [40]

The optimal criteria introduce a Lagrange multiplier that increases or decreases each sensitivity with a maximum allowed value. This modifies the objective function to response to the constraint.

This method is derived from the Karush-Kuhn-Tucker optimality condition and is interpreted as a stationary point of the Lagrangian function with respect to densities, displacements and multipliers [41]:

$$L = u^T K u + \lambda \left(\sum_{e=1}^{n} \rho_e v_e - V \right) + \mu^T (Ku - \rho) + \sum_{e=1}^{n} \alpha_e (-\rho_e + 0) + \sum_{e=1}^{n} \beta_e (\rho_e - 1) \qquad (2.17)$$

where $\lambda, \alpha, \beta, \mu$ are Lagrangian multipliers on fixed amount of material, equilibrium constraint and bound's constraints, respectively, L is the resulting stationary point and u is the displacement

For a demanding structural optimization, the method should be flexible, general and able to handle all kinds of constraints.

The method of moving asymptotes provides an approximative subproblem solved by an iterative process controlled by moving asymptotes. This is a method similar to CONLIN but faster once CONLIN converges slowly because of too conservative approximations[42].

These moving asymptotes stabilize and speed up the convergence. The variables used by MMA are:

$$y_j(x_j) = \frac{1}{x_j - L_j} \; or \; y_j(x_j) = \frac{1}{U_j - x_j}, \qquad j = 1, \ldots, n \qquad (2.18)$$

L_j and U_j are the moving asymptotes and changes during the process but satisfy for each iteration k (eq. 2.19)

$$L_j{}^k < x_j{}^k < U_j{}^k \qquad (2.19)$$

The MMA approximation of $g_i, i = 0, \ldots, l$ at the design x^k is defined by:

$$g_i^{M,k} = r_i^k + \sum_{j=1}^{n} \left(\frac{p_{ij}^k}{U_j{}^k - x_j} + \frac{q_{ij}^k}{x_j - L_j{}^k} \right) \qquad (2.20)$$

$$p_{ij}^k = \left\{ \begin{matrix} (U_j{}^k - x_j{}^k)^2 \frac{\partial g_i(x^k)}{\partial x_j} & if \; \frac{\partial g_i(x^k)}{\partial x_j} > 0 \\ 0 & otherwise, \end{matrix} \right\} \qquad (2.21)$$

$$q_{ij}^k = \left\{ \begin{matrix} 0 & if \; \frac{\partial g_i(x^k)}{\partial x_j} \geq 0 \\ -(x_j{}^k - L_j{}^k)^2 \frac{\partial g_i(x^k)}{\partial x_j} & otherwise, \end{matrix} \right\} \qquad (2.22)$$

$$r_i^k = g_i(x^k) - \sum_{j=1}^{n}\left(\frac{p_{ij}^k}{U_j{}^k - x_j{}^k} + \frac{q_{ij}^k}{x_j{}^k - L_j{}^k}\right) \tag{2.23}$$

$g_i^{M,k}$is an explicit convex function that requires that if p_{ij}^k, then q_{ij}^k and vice versa.

For more information on the MMA algorithm, there are some references that should be looked at Svanberg [43] and Christensen and Klarbring [21].

M. Fanni *et al*, [44] did a comparison (Figure 9) between MMA and different other methods according compliance values, consumed time and the resulted topological shape. The OC and HCA methods are faster in convergence, but these methods are considered as non-general optimization methods and cannot be used for complex optimizations. On the other hand, SQP and MMA methods handles any type of optimization with any type of objective functions and constraints.

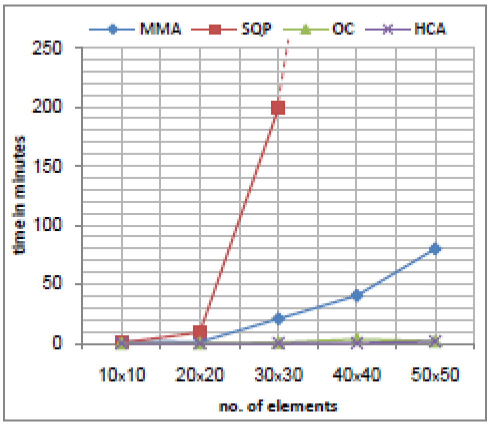

Figure 9 - Comparison between different topology optimization methods [44]

2.3.9 Topology optimization challenges

The topology optimization process is not free of potential errors [45]. The common numerical problems are divided into three categories, as follows:

i. Checkerboard effects
ii. Mesh dependency
iii. Local minima

For each of these problems, there are several preventing techniques:

i. Checkerboard effects – a) High order finite elements, b) Patches, c) Filtering, d) Restriction methods
ii. Mesh dependency – a) Relaxation, b) Perimeter control, c) Global/local gradient control
iii. Local minima – a) Continuation methods

i. Checkerboard effects

Checkerboarding problems occur when, in the results, some near elements appear alternating from solid to void. The results are similar to a checkerboard pattern and it is assigned as the most common problem for minimal compliance problems [46] and is a typical nonconvergence example. This solution leads to artificially high stiffness and hamper the manufacturing process of the part. The effect is illustrated on Figure 10 [29, 47].

Figure 10 - Checkerboard effects [29]

ii. Mesh dependency

In a common problem, mesh-refinement results in a better modelling of the same optimal structure and improves the boundaries description. In topology optimization, the structure is qualitatively different and has a tremendous impact in material locations. The resolution of a high mesh density provides finer details need for thin members while with low mesh, these members may not appear (Figure 11). This refinement is obviously connected with the manufacturing restrictions and this is a point that emphasize the importance of the additive manufacturing, [29].

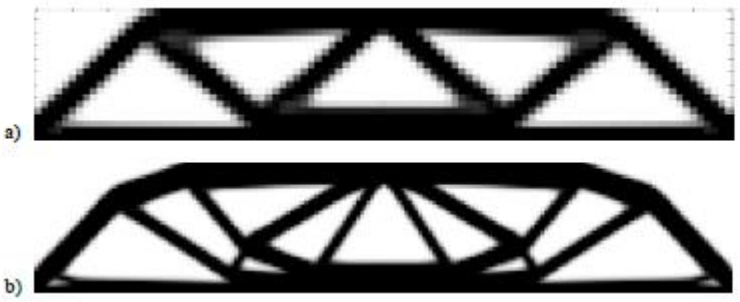

Figure 11 - Mesh dependency of Topology optimization[45]

iii. Local minima

The optimal design is very volatile, and it always changes with small variations in parameters, different geometry, number of elements and filter parameters. This occurs because, for optimizations with p>1, the results have many local minima. To solve this type of problems, it is applied continuation methods to change from convex to non-convex problems [45].

2.3.10 Other topology optimization methods

There are four different topology optimization methods, which are supported by different and advanced filters, which increase the quality of the topological results and integration in commercial softwares, such as:

1. Density-based methods
2. Discrete methods
3. Boundary variation methods
4. Biologically inspired cellular-division method

For the density-based methods, the main factor that differentiates the methods is the interpolation function and penalization. Besides the already detailed SIMP method, Stolpe and Svanberg [48] formulated the Rational Approximation of Material Properties (RAMP) which has nonzero density at zero density elements to avoid some difficulties associated with zero densities. For the SINH method, related to the use of the hyperbolic sine function, the penalization represents the material weight. Instead of penalizing material parameters, this formulation penalizes the volume directly. A comparison of this density based methods depending on the penalization and the equations of these methods are shown in Figure 12 [49].

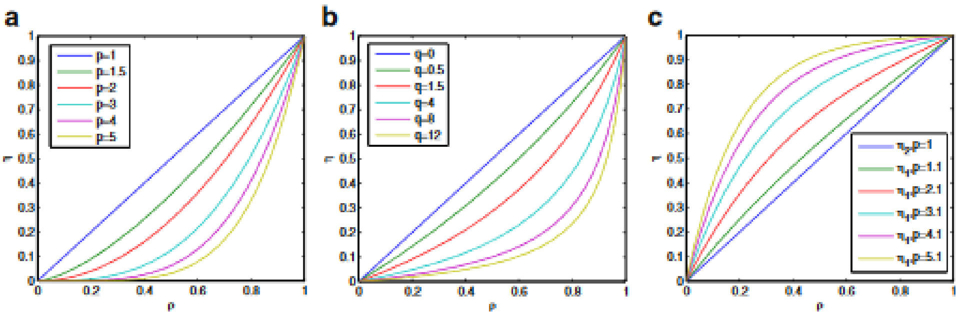

Figure 12 - Comparison of density based methods : a) SIMP, b) RAMP, c) SINH [49]

The discrete methods are very easy to use with commercial finite element analysis and their results are free of intermediate elements once his finite elements are defined to exist or not. This occurs due to the element removal/addition applied to the elements after the sensitivity calculation. The main method of this approach is the Evolutionary Structural Optimization (ESO) where is formulated a rejection ratio (RR) for iteration following this equation :

$$\frac{\sigma_e^{vm}}{\sigma_{max}^{vm}} < RR_i \tag{2.24}$$

where σ_e^{vm} is the Von Mises stresses in the element and $\sigma_{max}^{vm}$is the maximum Von Mises stress in the structure. The element removal criterion was after developed to a sensitivity number of each element directly related with the stiffness of the element (eq. 2.25).

$$\alpha_i^e = \frac{1}{2} u_i^T K_i u_i \tag{2.25}$$

where u_i is the element displacement vector and K_i is the element stiffness tensor.

2.3.11 Topology optimization software

During the last few years, modules of topology optimization have been integrated into the industrial calculation codes. There are several softwares providing topology optimization modules such as Optistruct, which comes with Hyperworks (Altair), Tosca(FE-Design), which comes with the Abaqus code (DS Simulia), MSC-Nastran (MSC Software), Genesis (VRCreo (PTC)), PLM Software, which comes with NX/CAE (Siemens), and Inspire (SolidThinking) and Ansys [50]. Here after three of them will be described in brief.

Hyperworks Optistruct

This software was released in 1994 and was one of the first to provide structural optimization to a commercial software. Is one of the most used nowadays and provides the possibility of optimizing regarding the buckling strength. The student license is very limited, lacking several features present on main version.

FE Design Tosca

One of the most used nowadays. It is compatible with most FEA-softwares. Provides powerful optimization solutions for design of lightweight, stiff, and durable parts, ready to manufacture designs and reduces the number of tests required and prototype builds.

Ansys/Siemens NX/MSC Nastran

Based on algorithms of Tosca structure software, suitable for structural and fluid flow problems.

2.4 Fatigue Analysis

Fatigue is the failure induced on a material upon cyclic load action. It is difficult to predict, once it is not visible in the early damaging stages and generally leads to abrupt failure. Normally, fatigue damage is characterized by three stages: crack initiation, crack propagation and fracture as seen in Figure 13 [51].

.

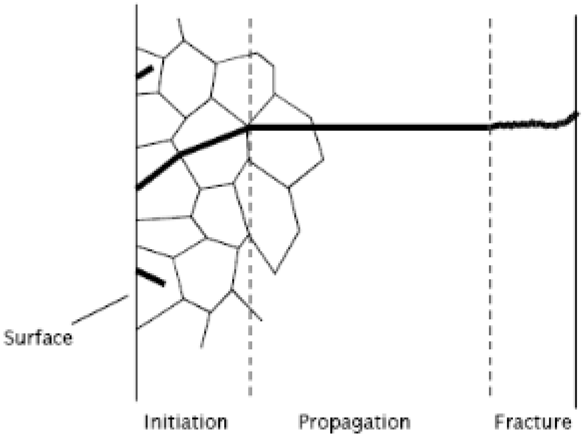

Figure 13 - Stages of fatigue failure [51]

Fatigue damage can evolve according to three different regimes: Low-Cycle Fatigue (LCF)(between 1 to 10^4 cycles), High-Cycle Fatigue (HCF)(more than 10^4 cycles) and infinite life (no fatigue failure). Fatigue strength depends on the nature of loading. If the amplitude loading is variable, it can be defined by deterministic or stochastic analysis methodologies can be used to assess fatigue damage. Figure 14 gives an overview of the fatigue damage regimes and common assessment methodologies.

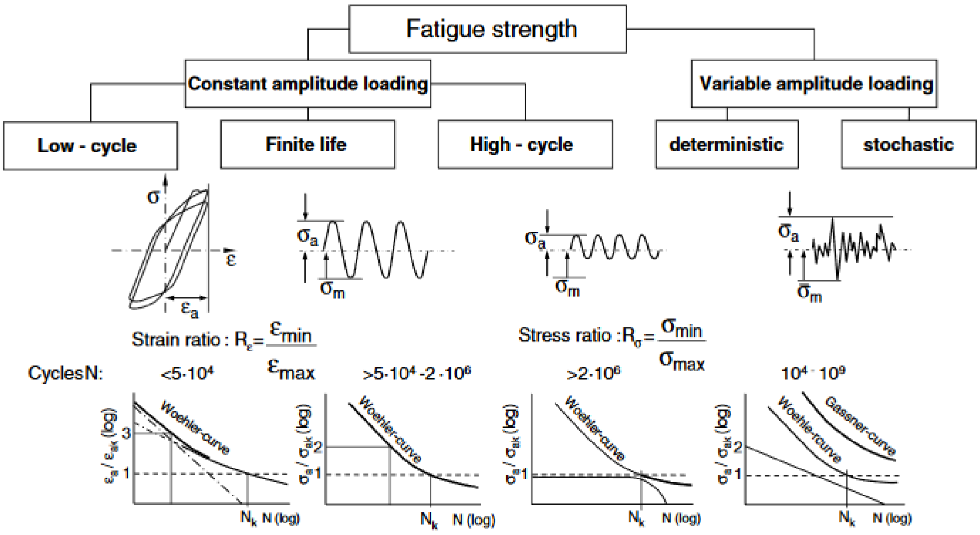

Figure 14 - Partition of fatigue strength[52]

The main difference between high-cycle and low-cycle fatigue is that in HCF only elastic deformation occurs while in LCF elastic and plastic deformations are coexistent.

The stress-life methodology is often applied with constant and proportional loading for fatigue analysis in HCF regimes. For constant amplitude fatigue loading where the load cycles are identical, usually sinusoidal, one need to introduce the following loading definitions: alternating stress amplitude (S_a), the mean stress S_m or the maximum stress S_{max} and the minimum stress S_{min}. These stresses are related as follows:

$$S_{max} = S_m + S_a, \tag{2.26}$$

$$S_{min} = S_m - S_a, \tag{2.27}$$

$$S_m = \frac{S_{max} + S_{min}}{2} \tag{2.28}$$

The stress range is $SR = 2\,S_a = S_{max} - S_{min}$ and the stress ratio, $R = \frac{S_{min}}{S_{max}}$. In Figure 15, it represents one cycle of a sinusoidal load and a representation of each stress mentioned above.

This high-cycle fatigue approach is applied when the materials behaviour is elastic and there is no assumptions on separation of crack initiation and crack propagation in the fatigue analysis. Total fatigue failure or crack initiation are able to be assessed using the stress-life approaches.

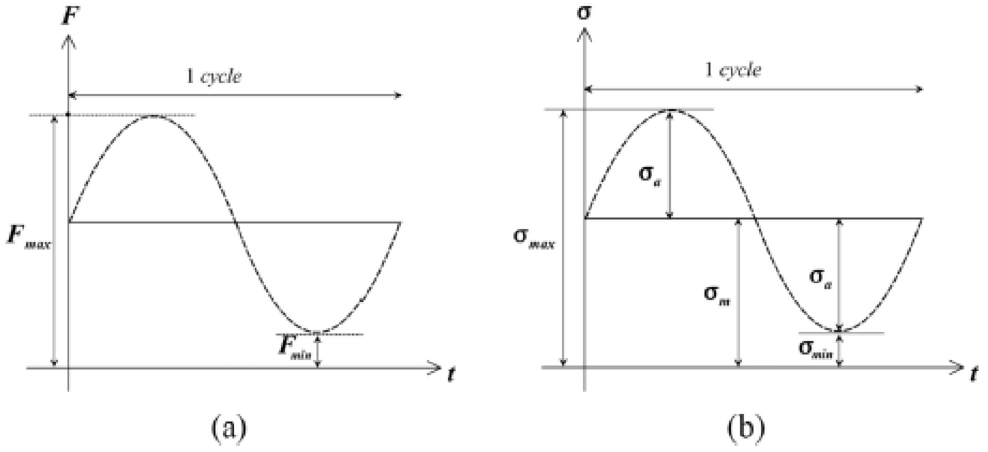

(a) (b)

Figure 15 – Stress cycle definition: a) sinusoidal load cycle; b) Sinusoidal stress cycle [53]

2.4. 1 Stress-life (S-N) curves

There are different approaches for fatigue failure analysis such as stress-life method, strain-life methods and Linear Elastic Fracture Mechanics based method. For HCF it is common to use a stress-life curve since it can be translated into strain-life curve following the equation $\sigma = E * \varepsilon$, because the stresses are always within the elastic range. S/N curves, also called Wöhler curves, depends on the number of cycles usually plotted on a logarithmic scale and the alternating stress plotted on linear or logarithmic scale. This curve is obtained from fatigue tests at different stress levels and represents the quantitative relationship between applied stress cycles and the specimen lifetime. In certain ranges, the following the S-N curve, is used to represent the fatigue strength of the material/component (Figure 16) :

$$\frac{N}{N_D} = \left(\frac{S}{S_d}\right)^m \tag{2.29}$$

where N_D is the fatigue limit cycles (infinit life cycles definition), N represents the fatigue life and S_d the endurance fatigue limit. For variable amplitude loading there is a need to define the fatigue damage variable, D_i. The damage for a number of constant amplitude cycles, n_i, at the stress amplitude S_{ai} is defined by the ratio between that number of cycles n_i and the number of cycles required to failure for a constant amplitude loading at σ_{ai}, N_i [54]

$$D_i = \frac{n_i}{N_i} \tag{2.30}$$

For a loading case with different stress amplitudes over the time, a linear damage accumulation is often assumed according to Miner's proposal [54].

$$D_i = \sum_{i=1}^{n} \frac{n_i}{N_i} \tag{2.31}$$

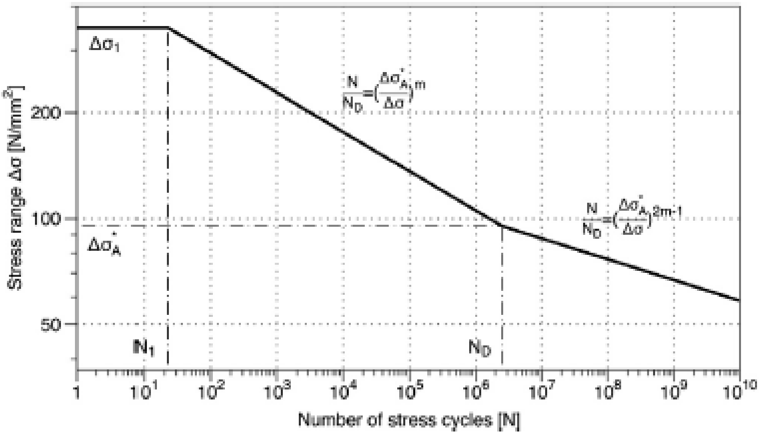

Figure 16 - S-N curve used for fatigue calculations[55]

The mean stress of the stress cycle can have a substantial influence on fatigue behaviour. In general, tensile mean stresses are detrimental and compressive are beneficial (see Figure 17) [56].

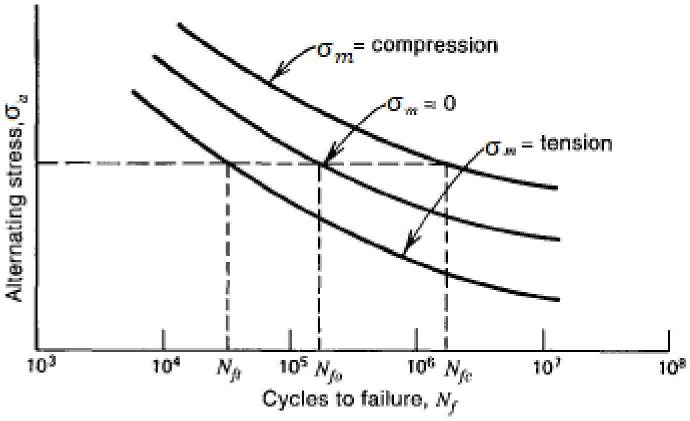

Figure 17 - Effect of mean stress on fatigue[56]

The fatigue endurance limit is an important fatigue property to be used in design against fatigue. Therefore, the knowledge about this property is mandatory, which would require very expensive tests. There are however approximation procedures to get the design information. For example, the fatigue endurance limit for $S_m = 0$ or stress R-Ratio, R=-1, a classical approach is given by using the linear relation between tensile fatigue strength, S_f , corresponding to infinite life, the and ultimate tensile strength, S_U of the material:

$$S_f = \alpha S_U \tag{2.32}$$

where α=0.5 for steel and titanium alloys, and α=0.35 for aluminium alloys[57].

Some relations discriminate the steels according to their specific tensile strength. The fatigue strength S_f estimated for steels with a tensile strength S_U lower than 1400 MPa is $S_f \approx 0.5S_U$ (Figure 18) and for higher values of S_U, $S_f = 700$ MPa is assumed.

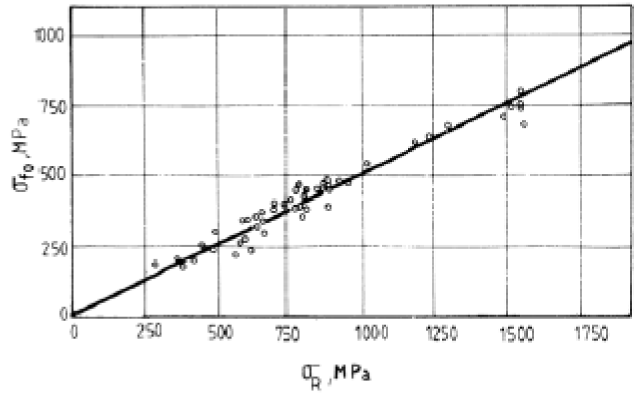

Figure 18 - Correlation tensile strength vs fatigue strength for steel [58].

The influence of the mean stress on fatigue endurance limit or any other specific fatigue lives is a common problem in design. In cases with nonzero mean stress, the following equations allows the correction of the tensile mean stress effects on fatigue endurance limits:

Modified Goodman:

$$\frac{S_a}{S_f} + \frac{S_m}{S_u} = 1 \tag{2.33}$$

Gerber:

$$\frac{S_a}{S_f} + \left(\frac{S_m}{S_u}\right)^2 = 1 \tag{2.34}$$

Morrow:

$$\frac{S_a}{S_f} + \left(\frac{S_m}{S_f}\right)^2 = 1 \tag{2.35}$$

Soderberg:

$$S_a = S_f \left(1 - \frac{S_m}{S_0}\right) \tag{2.36}$$

where S_a is the fatigue endurance for non-null meal stress, S_m is the mean stress, S_f is the fully reversed fatigue limit or endurance limit, S_u is the ultimate tensile strength and S_0 is the yield strength.

The Soderberg equation is more conservative compared to the others, as is shown in Figure 19 [57].

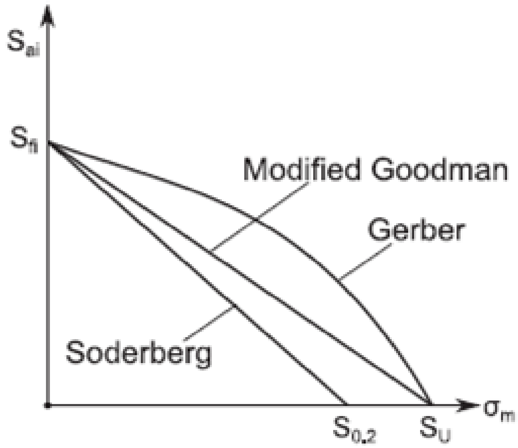

Figure 19 – Mean stress corrections of fatigue endurance limit [57]

2.4. 2 Low-Cycle Fatigue

When LCF occurs the stress cannot be directly translated to a strain-life curve. Therefore, a strain-life approach will be necessary. For this purpose it is useful to separate the two components of deformation: elastic and plastic. For the elastic component of deformation ε_e, Basquin suggested a relation in following the form (eq. 2.37),

$$\varepsilon_a E = \frac{\Delta\varepsilon_a E}{2} = \sigma_a = \sigma_f^{'}(N)^b \tag{2.37}$$

where $\varepsilon_a = \frac{\Delta\varepsilon_a}{2}$ is the elastic strain amplitude, E the Young modulus, σ_a the elastic stress amplitude, N is the life at σ_a. $\acute{\sigma_f}$ a fatigue strenght coefficient and b a fatigue strenght exponent or Basquin’s exponent.

Coffin and Manson proposed a relation between the plastic component of the cyclic strain and fatigue life leading to what is known today as the Manson-Coffin relationship (eq. 2.38) [59]:

$$\varepsilon_p = \frac{\Delta\varepsilon_p}{2} = \varepsilon_f\acute{}(N)^c \tag{2.38}$$

where $\Delta\varepsilon_p$ is the plastic strain range, $\acute{\varepsilon_f}$ is the fatigue ductility coefficient, c the fatigue ductility exponent, which are assumed material properties. The fatigue ductility exponent c, can be approximated by:

$$c = \frac{-1}{1 + 5n'} \tag{2.39}$$

where n' is the cyclic strain hardening exponent of the material,

Combining the two fatigue relations it is possible to develop a $\varepsilon_a - N$ curve accounting for both the elastic and plastic components (eq. 2.40):

$$\varepsilon_a = \frac{\Delta\varepsilon_t}{2} = \frac{S_f(\acute{N})^b}{E} + \varepsilon_f\acute{}(N)^c \tag{2.40}$$

As the plastic strain component has more influence, a stress relaxation reduces the mean stress and can bring it to zero. The reduction of mean stress is illustrated in Figure 20.

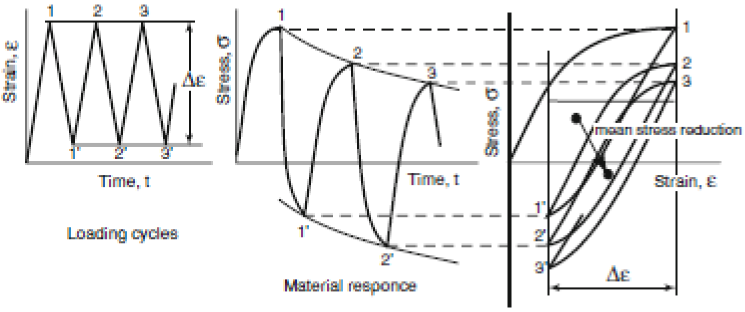

Figure 20 - Reduction of mean stress due to stress relaxation[59]

This reduction of mean stress affects the elastic component of the $\varepsilon_a - N$ curve and Morrow developed a correction to improve the results of fatigue life (eq. 2.41)

$$\varepsilon_a = \frac{S_f - S_m}{E}(N)^b + \varepsilon_f\acute{}(N)^c \tag{2.41}$$

2.4. 3 Fatigue constrained topology optimization

There are several publications concerning fatigue optimization. For shape optimization there is much interesting work. Fatigue topology optimization was also studied by applying equivalent static loads regarding the dynamical nature of loading conditions. (Grunwald and Schnack (1998)[60]; Mrzyglod and Zielinski (2006)[61]; Kaya et al. (2010)[62]).

Svärd, H (2015)[63] tried to incorporate fatigue failure probability of a small volume element as function of the applied stress based on the weakest link model developed by Weibull in 1930.

Collet *et al*. (2017)[64] utilized the modified Goodman failure criterion based on the Sines method for infinite-life fatigue.

Svärd, H (2015) [65] considered the “critical plane” criteria for fatigue. It is very difficult to find the critical plane, once every node has to be subjected to a function of the normal direction of the plane that is not concave, so, gradient based methods do not guarantee convergence. This paper uses the worst case error to guarantee a solution for the fatigue criterion evaluation.

Changing the entire algorithm of the optimization, applying fatigue constrains Holmberg *et al* (2014)[66]. Before the optimization it was determined a critical fatigue stress, using this stress as constraint and the minimum mass as objective function.

Jeong *et al* (2015) [67] uses a static and harmonic FE procedures and demonstrated that the local mode was a problem to fatigue-constrained TO method and is resolved by using a higher mass penalization factor.

Nabaki *et al* (2019) [53] used the fatigue-based BESO method minimizing compliance subject to fatigue and volume constraints. The failure criterion used was the modified Goodman, which was already applied in the sensitivity analysis. The compliance of the fatigue-constrained topology optimization was higher than the traditional one.

3 Project Specifications and Part Modelling

This section contains the specifications of the case study (component) considered for this research as well as the description of the numerical approach conducted for the topology optimization.

The component selected for this study is a holding support element, commonly called “bracket”, used in aerospace industry. In particular a bracket developed by Topological Optimization and Additive Manufacturing for the Airbus A350 XWB, see Figure 21, is selected for this study. This element makes part of the suspension of a flight Crew Rest Compartments (FCRC) on the primary structure of an aircraft (frames, structure and outer skin). This component will be used as a reference in this work for a topological optimization exercise as well as for the additive manufacturing process simulation and final fatigue analysis of the component. The selection of an existing component was important to allow benchmarking work between the proposed optimization exercise and the existing solution for the bracket.

The part dimensions, information of the material used, as well as the forces and boundary conditions applied, were obtained from Kranz[68] and are summarized in Table 1.

Figure 21 - Airbus ALM/3D Printing FCRC Cabin Bracket Installation[69]

Table 1 - Bracket Data [68]

Data of the component	
Designation	FCRC-bracket
Function	Transmit loads
Material	Al 7075; ρ=2.8g/cm^3;
Dimensions (mm)	160.5 x 65 x 65.5 (y,z,x)
Weight (g)	226
Charges	Static loads (see Figure)

3.1 Material properties

Due to the interaction with other projects on the field of additive manufacture, it was decided to establish the 316-L Stainless Steel as the working material. This material shows a good weldability and is a very popular material in AM applications, mainly because of its corrosion resistance resulting from the nickel and molybdenum contents in the alloy. In order to characterize the elastic and plastic hardening behaviours of the material, the parameters presented in the Table 2 were considered [70]. This data was introduced in numerical software ABAQUS® allowing to reproduce the elastoplastic behaviour of the material combining the isotropic and cyclic hardening of the material. The relation of stress range applied and the number of cycles is described by means of the SN curve estimated for R=-1 shown in Figure 22. This curve was used later to estimate the fatigue life of the optimized part taking into account the effect of residual stresses promoted by Additive Manufacture process and service load.

Table 2 – Properties of SS-316L[70]

Young Modulus	***Yield Stress***	***Kinematic Hardening parameters***		***Isotropic hardening parameters***	
E(GPa)	***S_0 (MPa)***	***c(MPa)***	***γ***	***Q(MPa)***	***b***
200	211	57.805	619.04	42.3	21.6

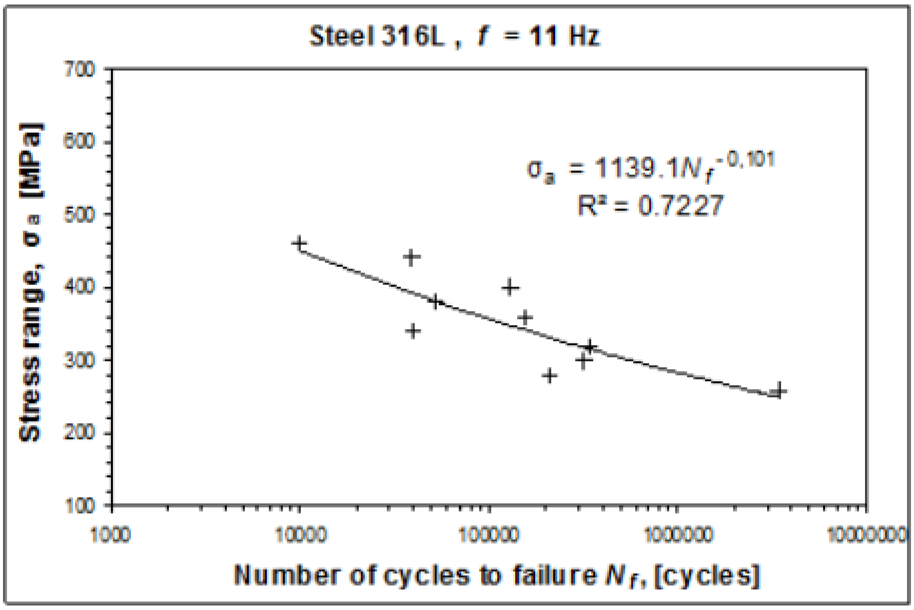

Figure 22 – S-N curve of the SS-316L[71]

3.2 Part specifications

The geometric and loading specifications of the bracket considered for this study are covered in this section. The geometry of the bracket is illustrated in the Figure 23 and the load and tightening points are exhibited in Figure 24. The boundary conditions was the encastre of the bottom of the bushing connector to simulate the bolts tightening and symmetry around the x axis to reduce the computational cost was considered. The initial mass of this part was 2.10 kg.

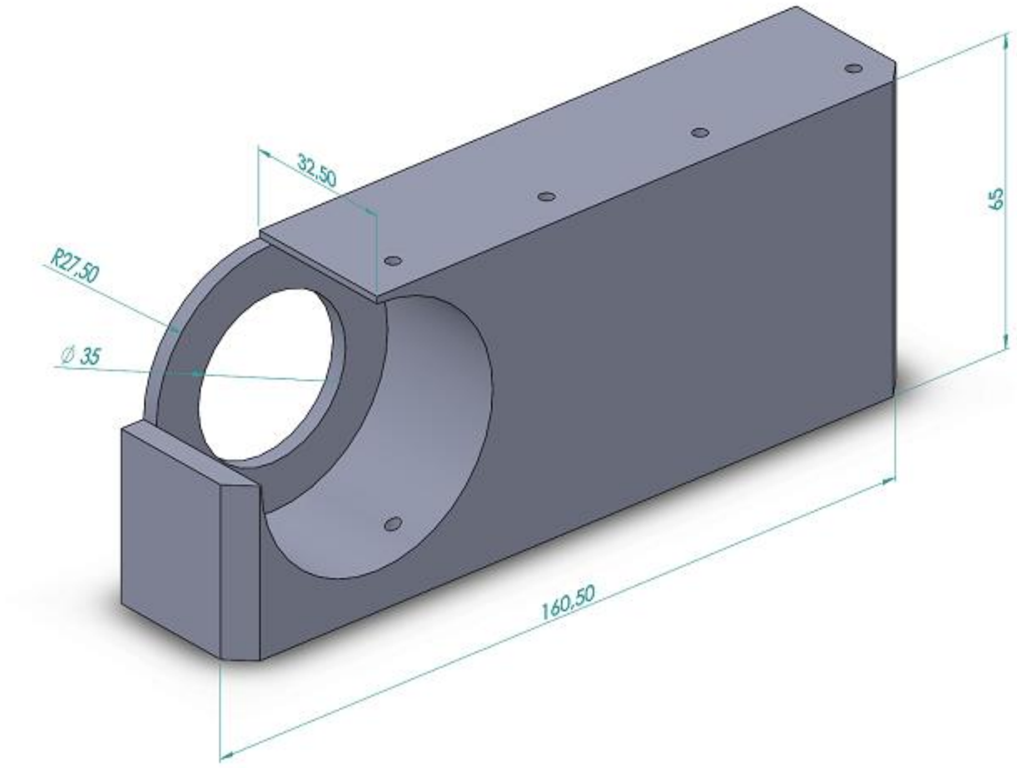

Figure 23 -3D part for topology optimization (dimensions in mm)

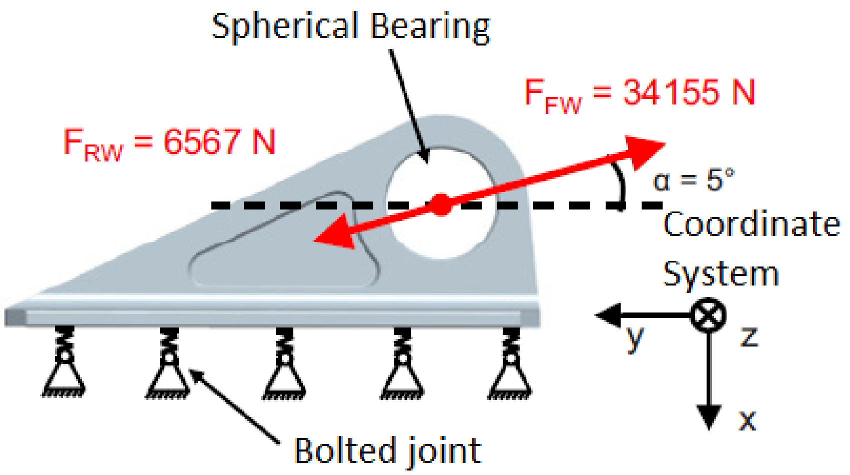

Figure 24 - Load and part specifications[68]

3.2.1 Finite Element Mesh

The mesh approximate global size chosen was 1.5 mm. It was assigned local seeds to the regions of the fasteners and to the hole where the load is applied. 4-noded linear tetrahedrons was used due to the simplicity of mesh generation. Figure 25 shows the model and the mesh parameters chosen.

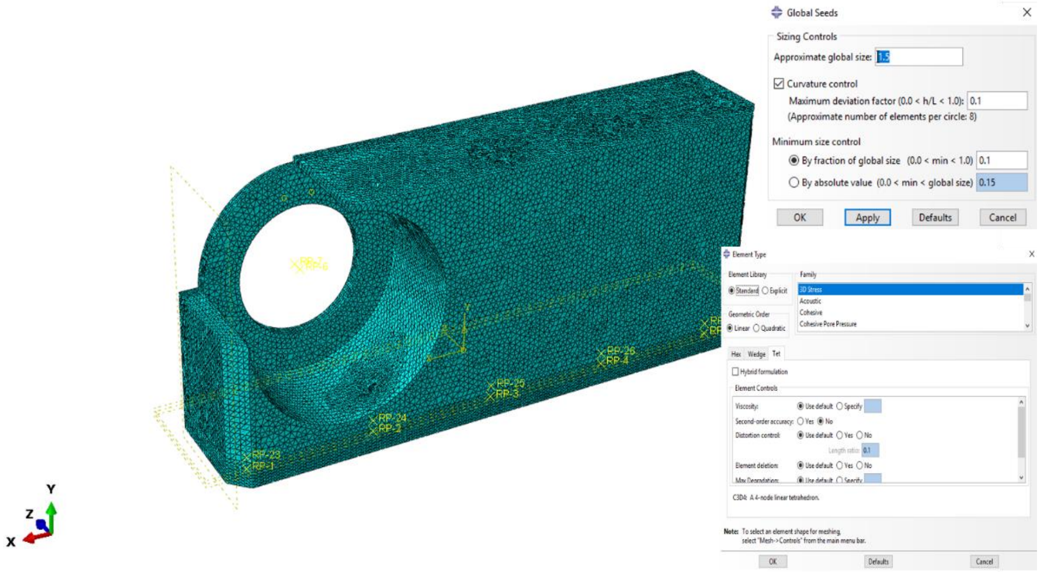

Sizing Controls
Approximate global size: 1.5
☑ Curvature control
Maximum deviation factor (0.0 < h/L < 1.0): 0.1
(Approximate number of elements per circle: 8)
Minimum size control
● By fraction of global size (0.0 < min < 1.0) 0.1
○ By absolute value (0.0 < min < global size) 0.15

Element Library: ● Standard ○ Explicit
Geometric Order: ● Linear ○ Quadratic
Family: 3D Stress, Acoustic, Cohesive, Cohesive Pore Pressure
☐ Hybrid formulation
Element Controls
Viscosity: ● Use default ○ Specify
Second-order accuracy: ○ Yes ● No
Distortion control: ● Use default ○ Yes ○ No
Length ratio: 0.1
Element deletion: ● Use default ○ Yes ○ No
Max Degradation: ● Use default ○ Specify
C3D4: A 4-node linear tetrahedron.
Note: To select an element shape for meshing, select "Mesh->Controls" from the main menu bar.

Figure 25 – FE Model with mesh parameters

To replicate the five existing fasteners on each side, the kinematic coupling constraint available in the ABAQUS was used. Typically, a kinematic coupling constraint is used to simulate the load transmission between two parts linked by a bolt connection. In detail, a control point is defined at the centre of the bolt hole and all degrees of freedom at the nodes on the holes surface (coupling nodes) are constrained [72]. A connector element between the reference point and grounded point was used: a 1D element type, designated by Bushing Connector, that requires the definition the of stiffness on the six degrees of freedom. A scheme of this coupling constraint is shown in Figure 26.

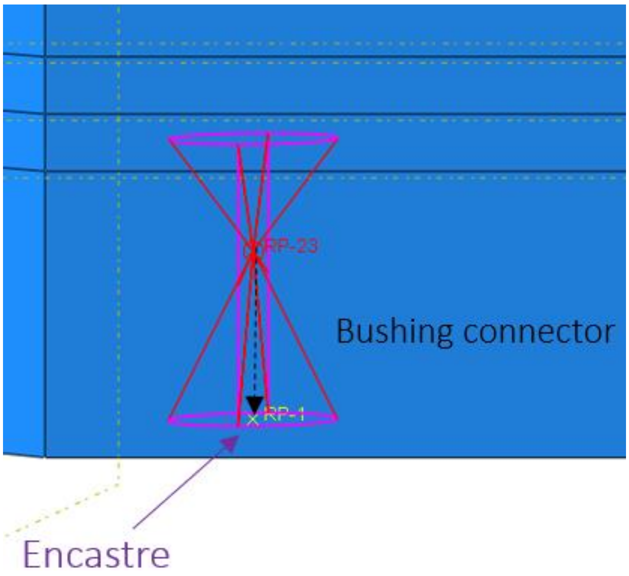

Figure 26- Reference node attached to the hole surface nodes and use of bushing connector

Using the bushing connector, results the advantages and limitations expressed in Table 3.

Table 3 - Advantages and limitiations of using bushing connectors[72]

Advantages	***Limitations***
Easy to establish "point-to-point" links when modelling bolted joints in structures	Calculations by hand need to be performed to obtain the bolt stiffness, which adds time and operations in the procedure.
Handle both elastic, plastic and damage behaviour in a simple way.	
Work with solid and shell models	
Can handle bending moment as secondary bending.	
Work with single and double shear lap joints.	

.

3.2.2 Bolt stiffness

In order to apply the Bushing Connector it is necessary to estimate several stiffness parameters, to be introduced in the numerical mode. Table 4 summarizes the stiffness coefficients required to be introduced as a function of the elastic properties and some geometric features of the bolted joints.

Table 4 – Stiffness coefficients and results for bushing connectors

Stiffness Coefficients	***Equations***		***Results (N/m)***
Axial Stiffness	$K_1 = \frac{E * S}{L}$	(3.1)	$1.48 * 10^5$
Shear Stiffness	$K_2 = K_3 = \frac{1}{C}$	(3.2)	$3.16 * 10^4$
Rotational Stiffness	$K_{5-6} = \frac{1}{\varepsilon} * \left(Max(K_2 * K_3)\right) * \frac{L_{BUSH}^2}{4}$	(3.3)	$7.9 * 10^7$

Regarding Table 4, the following nomenclature has to be introduced:

E = Material Young Modulus;

S= Fastener cross section area;

L= Fastener's length;

D= flexibility of the fastener, defined using Huth Formulation:

$$D = \left(\frac{t_1 + t_2}{2 * d}\right)^a * \left(\frac{b_1}{t_1 * E_1} + \frac{b_2}{t_2 * E_2} + \frac{b_1}{2 * t_1 * E_3} + \frac{b_2}{2 * t_2 * E_3}\right) \tag{3.3}$$

t_1: Thickness of plate 1

t_2: Thickness of plate 2

E_1: Young modulus of plate 1

E_2: Young modulus of plate 2

E_3: Young modulus of fastener

a: Coefficient depending on fastener type (2/3 for metallic and graphite/epoxy bolted joints; 2/5 for riveted metallic joints)

b_1,b_2: Coefficients depending on the joint plates material, b_1=b/n and b_2=b/n^2, with n=1 for single shear and n=2 for double shear, b=3 for bolted metallic, b=2.2 for riveted metallic and b=4.2 for bolted epoxy/graphite composites [73] and, for rotational stiffness

$$with\ \frac{1}{\varepsilon} = 100, \tag{3.5}$$

$$and\ K_4 = 100 \tag{3.6}$$

This modelling is only a good approximation, but the axial loads are accurately calculated if it is used contact modelling.

3.2.3 Spherical bearing and load point

The load point is characterized by having a spherical bearing to prevent deformations in the load area. This load point was modelled using a reference point coupled to the hole surface nodes as illustrated in Figure 27. The inner coupling point where the load operates is connected to the nodes of the circular surface by a kinematic coupling: all degrees of freedom of the reference point were restrained except rotation around y-axis [74].

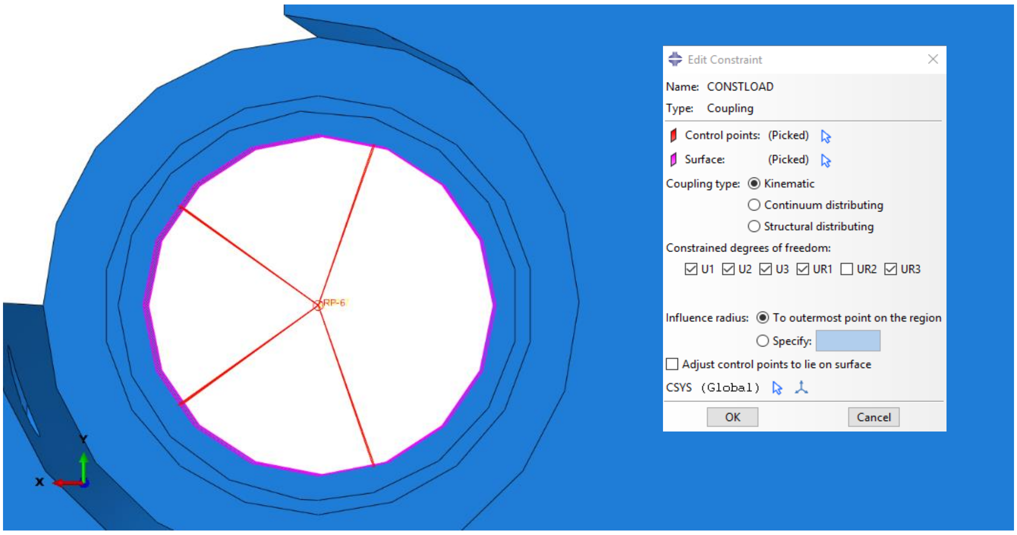

Name: CONSTLOAD
Type: Coupling
Control points: (Picked)
Surface: (Picked)
Coupling type: ● Kinematic
○ Continuum distributing
○ Structural distributing
Constrained degrees of freedom:
☑ U1 ☑ U2 ☑ U3 ☑ UR1 ☐ UR2 ☑ UR3
Influence radius: ● To outermost point on the region
○ Specify:
☐ Adjust control points to lie on surface
CSYS (Global)

Figure 27 - Coupling Constraint for load point

3.3 Topology optimization workflow

A topology optimization goes through several common stages. The flow chart is described in Figure 28 and sorts the stages and the challenges of each stage. All of these stages are iterative and several testes and simulations have been made to define the input parameters of each stage.

In order to define the design space, it was needed to isolate some specific areas of the initial material block. Once the optimization follows the SIMP method described before as a density-based approach, where some elements are forced to have a density near either 1 or 0, the bolt areas and the load/bearing assigned surface had to be partitioned in order to avoid material removal in those areas. In addition, all the other regions were involved in the design space and subject to optimization. These partitions are shown in Figure 29.

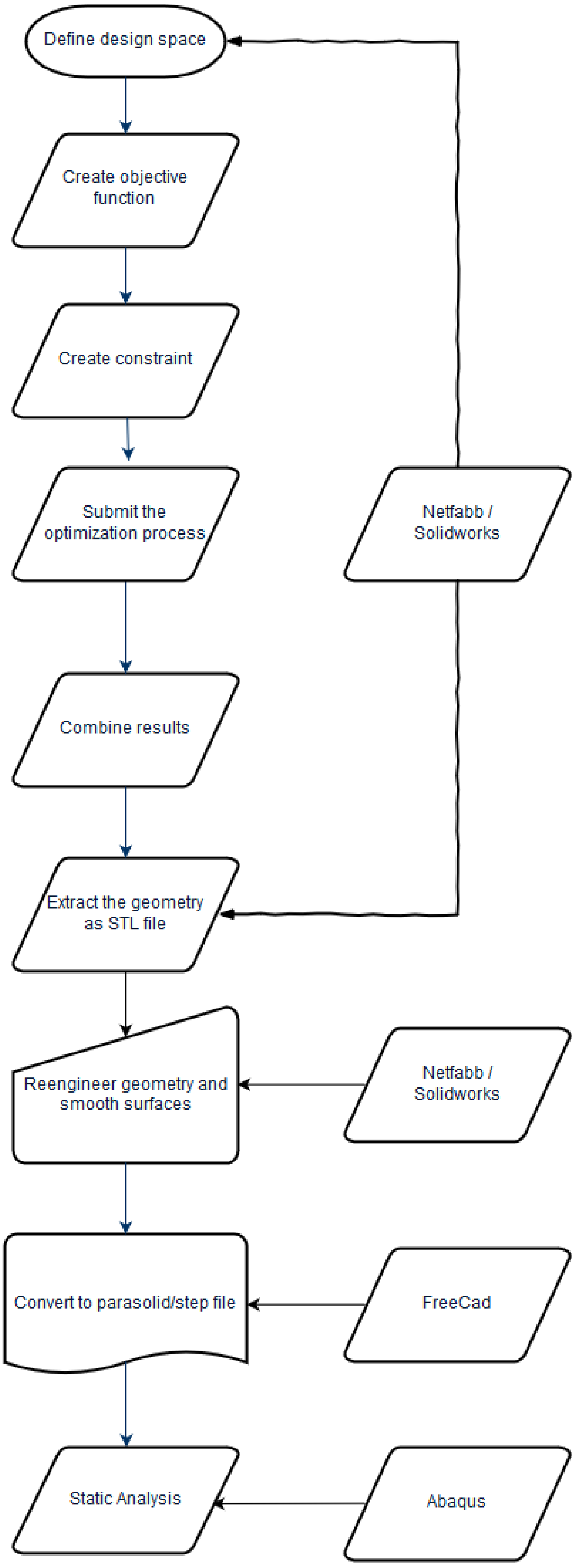

Figure 28 - Topology optimization workflow

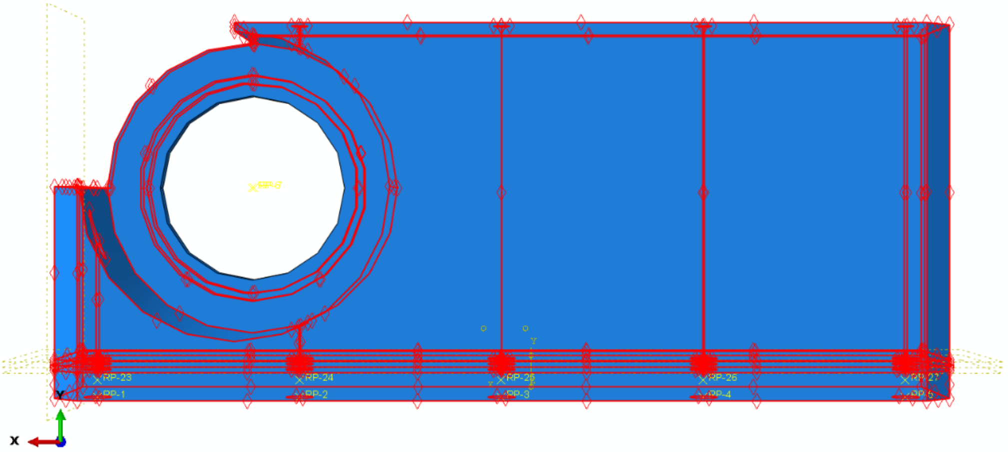

Figure 29 - Design region assigned for the topology optimization

The objective function was defined as the minimization of the strain energy of the component (the compliance method) and the constraints chosen intended to minimize the volume to a fraction of 0.12 of the initial value.

During the submission of the optimization process it was possible to monitor the process with access to a plot that shows the convergence of the constraint and objective function (see Figure 30).

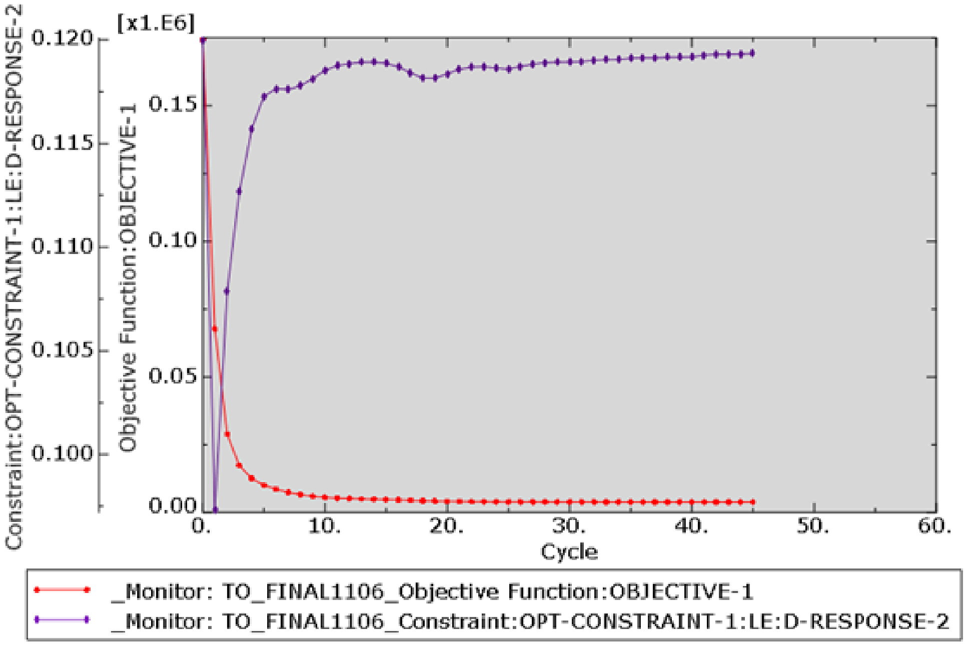

Figure 30 – Example of convergence of objective function and volume constraint

The optimization results in separate output database files for each design cycle. These separate files must be combined into a single output database file selecting the data needed to be shown in the Visualization module. It is possible to combine all the base results with analysis results from all the output database files, only the last result with analysis results from the last design cycle, the initial and last, every n cycles and it is possible to specify the desired design cycle with the analysis results. In this work, it was combined all the design cycles.

The post processing of the optimization results has some particularities too. Some parameters that can be changed during this stage, makes it possible to extract different geometries of the optimization. A threshold called ISO can usually be set to regulate which densities are displayed. The ISO value must be between zero and one. If the ISO value is very high, the isosurface will shift toward the inside of the model decreasing its volume. For example, for an ISO value of 0.5, the results only show the elements with densities above 50 %. The most recommended values for this parameter is ISO=0.3-0.5[75, 76]. Other parameters, like R% (Reduction percentage) that is used to give a coarser surface as well as the Number of Smoothing Cycles to obtain a smoother surface are required for the extraction.

After extracting the corresponding STL file, that only describes the surface geometry of a three-dimensional object, it is important to remove potential areas with stress concentration. In line with this objective, it was used the Netfabb software (educational version) that allows repairing and modifying STL files. The principal function used in this software was Smooth Triangles. This function smooths rough surfaces and rounds sharp edges, which can be stress concentration regions. For this process triangles with similar size are recommended. For each smoothing iteration, each corner point of the triangle mesh switch to a new position calculated by the average position of the adjacent corner points. Therefore, the position of the first corner point translates into the average value. As example of this process, the Figure 31 shows a smoothed cube subjected to five iterations [77].

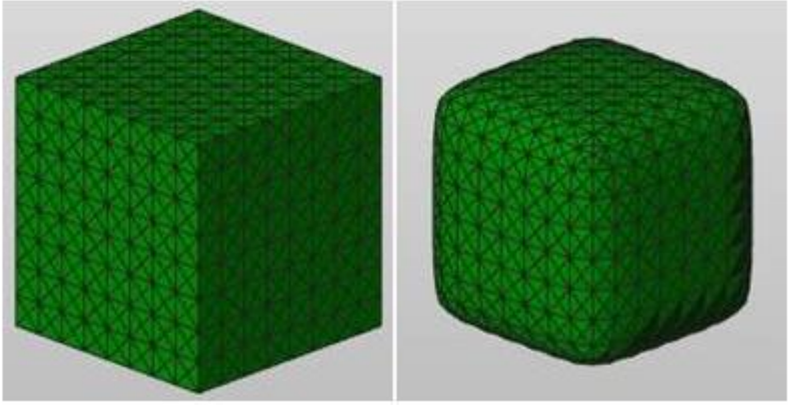

Figure 31 - Smooth triangle feature performed with Netfabb [77]

Other feature widely used was Refine Triangle Mesh (Figure 32). It minimizes the maximum edge length to a new value and finds appropriate triangles refinement. This feature does not change the shape of the part, just increases the number of triangles and devides the existing ones into smaller ones. It is possible to apply this feature to specific regions or to the whole part[78].

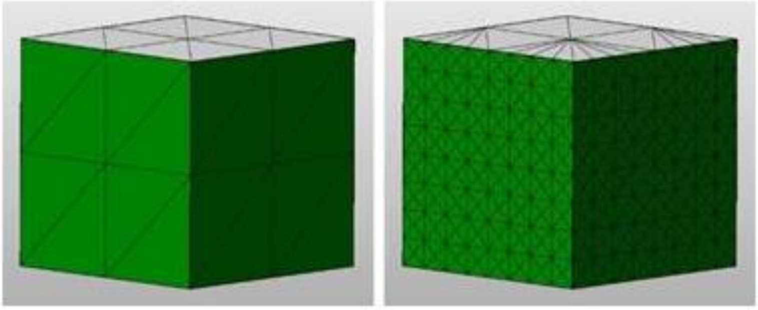

Figure 32 – Refine Triangle Mesh feature by Netfabb [78]

After smoothing and refine the potential critical regions it is necessary to obtain a Step or Parasolid files that provides precise geometrical information of the optimized part. It should be noted that a 3D model of the optimized part is necessary to execute a final analysis that will allow validating all optimization process. In fact, the stress field must be evaluated since under the predefined loading conditions.

FreeCad can import and export standard file formats allowing files conversion. For this purpose, it creates a shape from a mesh with a sewing tolerance that must be set. Then, it is important to simplify the part and refine shape to convert into a solid and later export to either Step or Parasolid formats in order to import again the model in the Abaqus.

Reengineer the part is also important, once it is necessary to interpret what kind of geometry was obtained and what will be the consequences of not modify it. It should be noted, that the optimization process leads to an initial approach of the final part. In fact, if there is a significant hole in a critical area of the part or if it is found a lack of material in certain areas it is important to correct it in order to avoid regions with high stress concentrations. To implement these adjustments, the 3D CAD software Solidworks was used again.

After this intermediate stage a static analysis of the part reproducing the same constraints, boundary conditions, material properties and loading conditions is performed. The results obtained from this simulation will be considered for the fatigue life assessment exposed in the Chapter 5. In addition, these results will be coupled with the results derived by the AM simulation that simulates the information about distortions and residual stresses from the manufacturing process.

4 Additive Manufacturing Simulation Details

4.1 Methodology

For simulating the additive manufacturing process of this case study part, the ESI Additive Manufacturing software was used.

There are several temperature-dependent material properties such as the density, thermal conductivity, specific heat, Young modulus and yield strength. These properties should be used during the simulation since their temperature dependency affects the residual stresses and distortion results [15]. For the simulation, the software is based on Equation 4.1.

$$\Delta L = \alpha L_0 \Delta T \tag{4.1}$$

where ΔL is the length variation, α the linear expansion coefficient, L_0 the initial length and ΔT the variation between the initial and final temperatures (T_i and T_f). In other words, the temperature variation causes distortion in the study part which would distort without create any residual stress. The inherent boundaries conditions do not allow the distortions and the residual stresses appear.

As it is used in most cases, mostly because of computational time, the method used in this case study is the uncoupled thermo-mechanical analysis. In this method, the analysis is performed sequentially and the interactions between temperature and stress fields are not considered.

The study can only give a macroscopic insight of the problem. For deeper understanding, it is possible to model the material at the powder level and consider the effects of fluid flow at the melt pool [79].

The application of the ESI Additive Manufacturing software requires some material parameters to simulate the building process of the part. These parameters will be explained below.

First, it is necessary to access the material database and assign the material properties to each part inside the model. It is necessary to assign material to the workpiece and baseplate. Since ESI software material database includes 316L stainless steel, it was not necessary to find the required properties in the literature and enter them manually in the software. The material information required for the AM simulation of the SS-316-L are shown in Table 5 and Figure 33.

Table 5- Properties of SS 316L required for the AM simulation

Solidification Temperature (K)	*Young's Modulus (Pa)*	*Poisson's Ratio*	*Expansion Coefficient (1/K)*
1673.15	1.95×10^{11}	0.29	1.99×10^{-5}

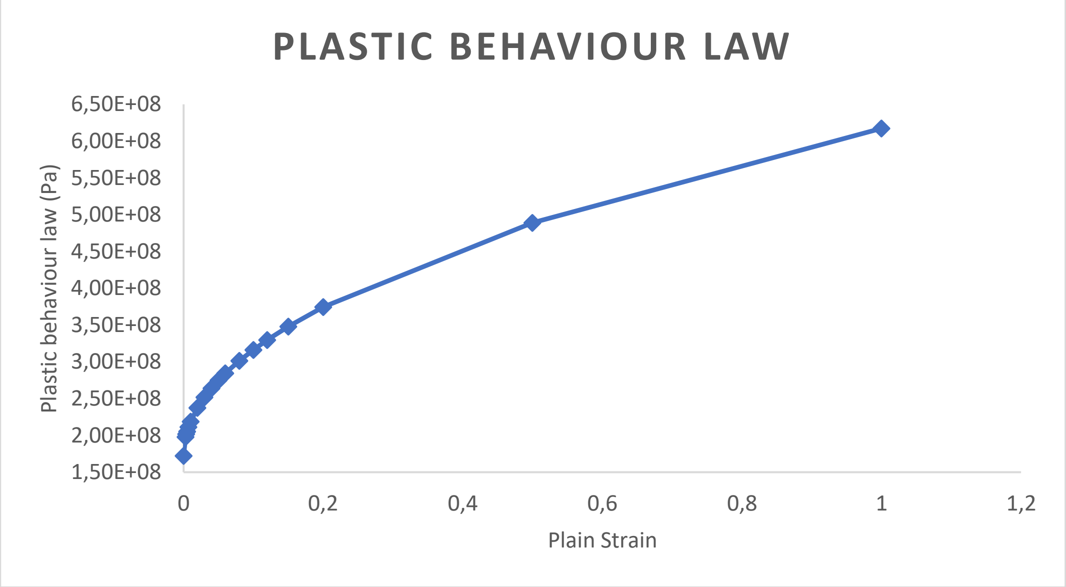

Figure 33 - Plastic behaviour law of SS 316L

The pre-processing starts with the definition of the project settings, indicating the directory which will be used. After that, it is necessary to define the workpiece, which is imported as the resulting STL file from the smooth stage of TO process, which was explained in Section 3.3. The baseplate needs to be delineated too, since the program will demand its dimensions. For this project, it was used a 250x250x25 mm steel plate. The 250x250 transversal section has been chosen because it is the most common value for the majority of the L-PBF machines and appropriated for the case study component. The thickness of 25 mm was selected in order to be large enough to avoid the baseplate warping during the manufacturing process.

The process parameters required by the software are three temperature of different zones and building stages, being them:

Chamber temperature: Temperature during the building process;

Release temperature: Temperature of the spare part;

Ambient temperature: Temperature after cooling and removing process.

The chamber temperature is the most important parameter, since it has a fundamental role in the simulation during the building process. For the solver default thermal analysis, the chamber temperature is set for the previous build layer (the layer immediately under the construction layer), for each iteration. The material solidification temperature is established for the "under process" layer (the layer which is being melted at the present stage). The software will solve a finite element problem, where the last built layer will be at the solidus temperature (initial temperature), and it will cool down until the ambient temperature (Chamber temperature). All these three temperatures (chamber, release and ambient) were set to 30ºC.

Figure 34 it is explains the influence of each temperature on thermo-mechanical loads.

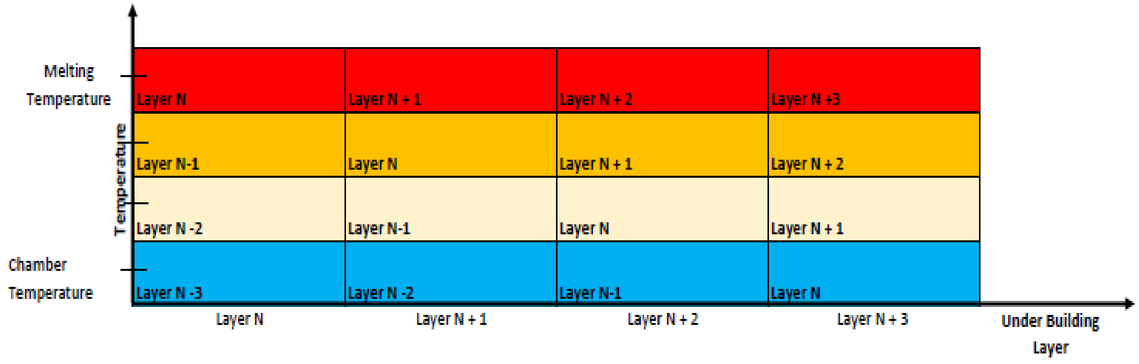

Figure 34 - Principal stages and temperatures of the additive simulation

The cooling process can be used as default (described previously) or it can be used the Custom Cooling Law. Choosing this custom cooling law, the software will ask how many layers it will take to the material to cool from the melting temperature (building layer) to the chamber temperature. All layers in between will be their temperature calculated using a linear interpolation from these two temperatures. These temperatures can be seem in Figure 35, where for this example it was used four layers for the Custom Cooling Law.

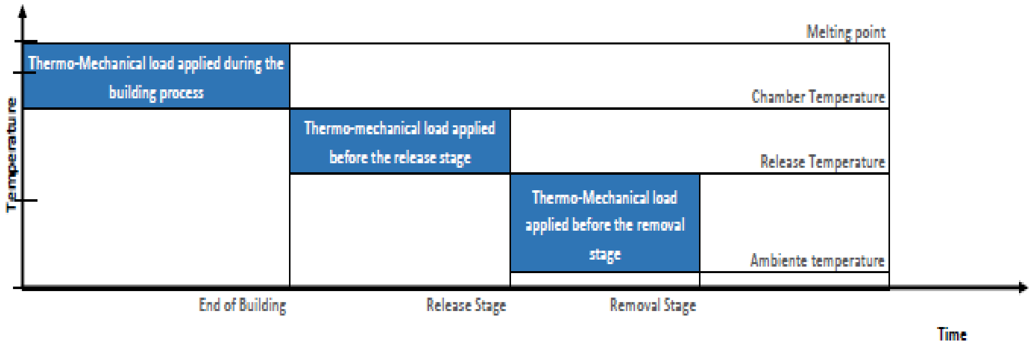

Figure 35- Temperatures and stages characterizing custom cooling law

The scanning strategy allows two strategies/deposition options: the full layer deposition or the multiple patch deposition. If the multiple patch strategy is followed, the workpiece geometry will be subdivided into stripes and the model will do numerical resolutions for each stripe of the layer. The full layer strategy is a simplification of the model but deliver faster results. These two strategies are shown in Figure 36.

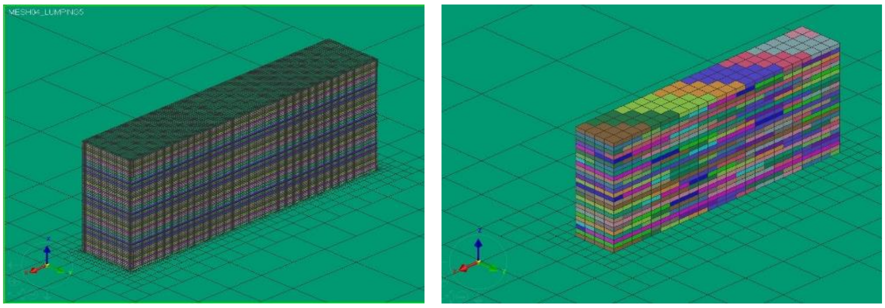

Figure 36 - Scanning strategy options of the part: Full layer deposition/activation (left) and multiple patch strategy (right)

In this study full layer deposition simulation was considered since it allows the following advantages:

- The workpiece geometry is subdivided into layers;
- The model activates each complete layer one after the other;
- As a result of the previous features, the simulation will be faster.

For the support strategy, the software gives the opportunity to import a specific support geometry, provided as STL, or to choose an automatic support strategy. For this last option, to define the support it is important to input the stiffness for each direction. These stiffness values are the spring parameters that will be applied as boundary conditions at the global stiffness matrix. For the present case, the support stiffness values were set as a default value.

Using the automated supports strategy, it is essential to define the inclination angle criterion, which was set as 45º. This criterion corresponds to the maximum inclination that would need to be supported above that, surfaces are considered as self-supported. In addition, the software requires information about the minimum area where a support can be placed (if a very small piece is suspense, with an area below the minimum specified, the software will not place a support there). For the presented simulations, it was set a minimum value of 1 mm^2 for the supports to be placed.

There are three stages of this simulation, as displayed in Figure 37:

- Building process where layers are deposited;
- Release the baseplate and workpiece from machine;
- Remove workpiece from baseplate.

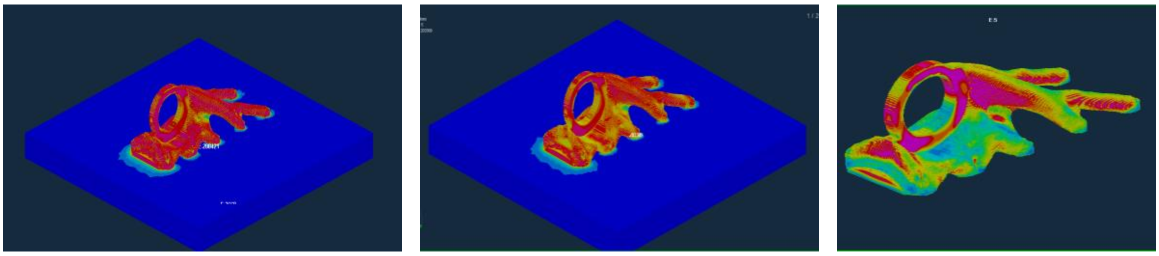

Figure 37 - Stages of the simulation (left) building process, (middle) Release build plate from the machine, (right) Removal of the workpiece from the base plate

The meshing strategy used was the locally refined. This mesh is characterized by fine mesh at the workpiece surface where, usually, stress and stress gradients are larger. This mesh strategy returns coarse cells inside the volume. It is well adapted to the baseplate, because the mesh refines towards the location of the part what optimizes the use of elements.

The mesh strategy can also be uniform (same cells size) or baseplate dependent (strategy used when there is a focus on knowing the building process effect on the baseplate) either uniform or locally refined.

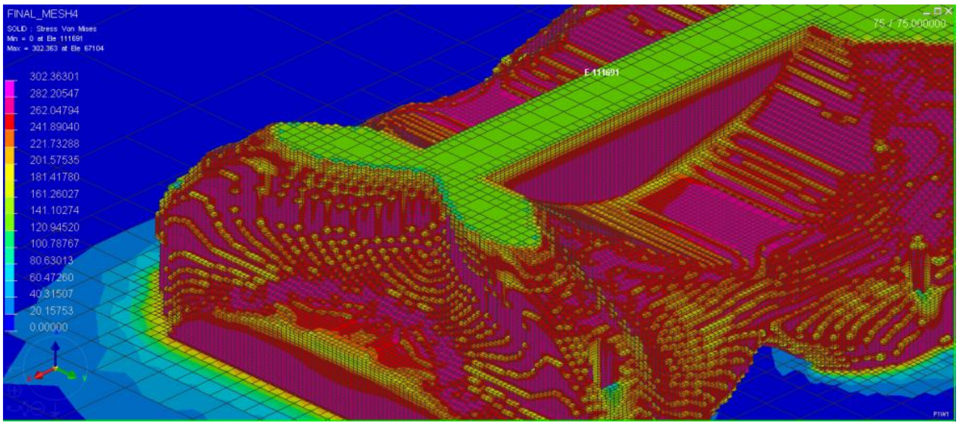

Figure 38 - Meshing strategy (locally refined)

As it is possible to infer, from the analysis of Figure 38, the mesh is not uniform for all the generated elements. This strategy is not the strictly desired on most of the cases. However, for fatigue, the exterior elements have a major relevance compared to the interior ones, the only way to provide a good mesh is to locally refine the part, due to the software restriction of a maximum of 2.000.000 elements.

For defining the mesh size, the software requires the cell size of elements at the normal direction of the workpiece surface, the tangential direction. In addition, there is an additional parameter called “background mesh”, which allows more accuracy to the mesh for thin geometries (geometries thinner than the element size).

5 Results and Discussion

5.1 Optimization Results

The results obtained from the topological optimization coupled with additive manufacturing process simulation of the mechanical component selected as case-study and described in the Section 3 are presented in this section. In detail, the topology optimization procedure was conducted in ABAQUS with the SIMP algorithm and following the workflow presented in the previous chapter which allowed to obtain a modified bracket with a mass reduction of 12,5%. The additive manufacture process was also simulated by means of commercial software ESI, which allow to derive the residual stress field and distortions. A fatigue assessment was performed combining the effect of the alternating stress resulted from the cyclic loading and considering the effect of mean stress, which in turn are dependent of the residuals stresses imposed by the manufacture process.

The bracket previously illustrated in the Figure 23 was the starting point for the topology optimization. It was followed the workflow already presented and the applied objective function was minimizing the strain energy and the constraint was limited, after several tries, to 12 % of the initial volume. Since the case-study part presented a symmetry, only half of the bracket was optimized using the z-symmetry as boundary condition.

The results of the optimization must be interpreted regarding the value of the density of the elements that contributes for the global stiffness of the problem. The density threshold must be chosen between a compromise of mass/volume reduction and the geometrical appearance of the part. With the density method, the material density of each element is directly used as the design variable and the topology optimization results exist between $0 \leq \rho \leq 1$; these represent the state of void and solid, respectively. It should be noted that the mapping is chosen in a way which reduces the stiffness to weight ratio of elements with intermediate design variable values, thus making them structurally inefficient. For a density of 0.7 the geometry presented in the Figure 39 was obtained.

In Appendix A, the deformation and stress field (Von Mises) resulting from the optimization are presented.

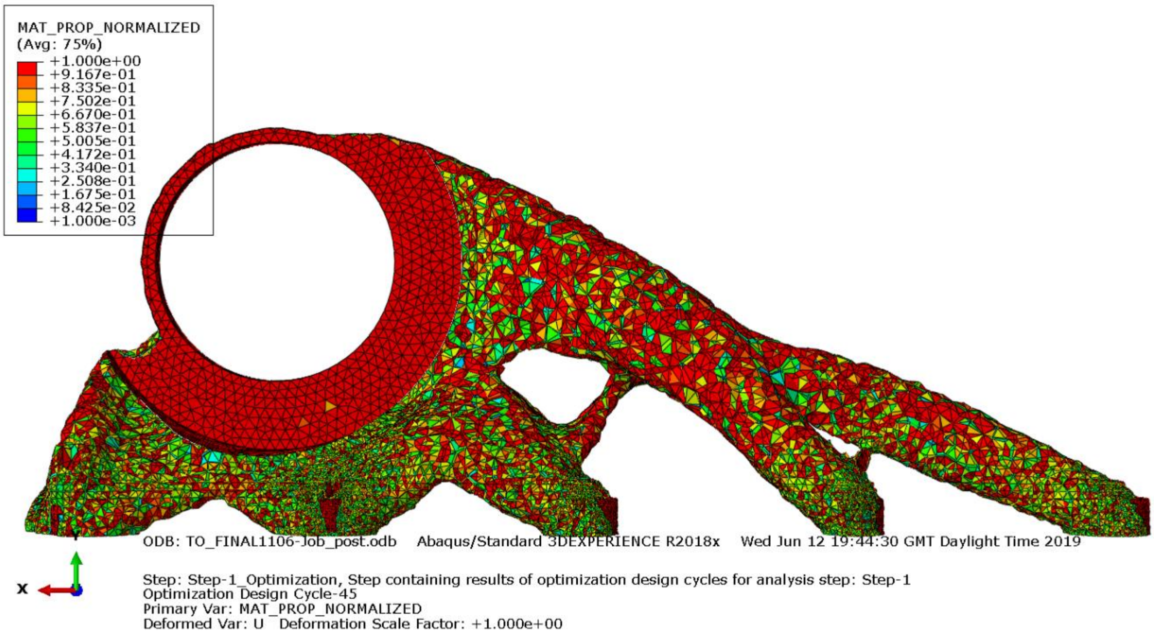

Figure 39 - Topology optimization results (ISO-value=0.7)

The ISO-value or density threshold of 0.5 [76, 80] was chosen to extract the geometry from the ABAQUS (see Figure 40).

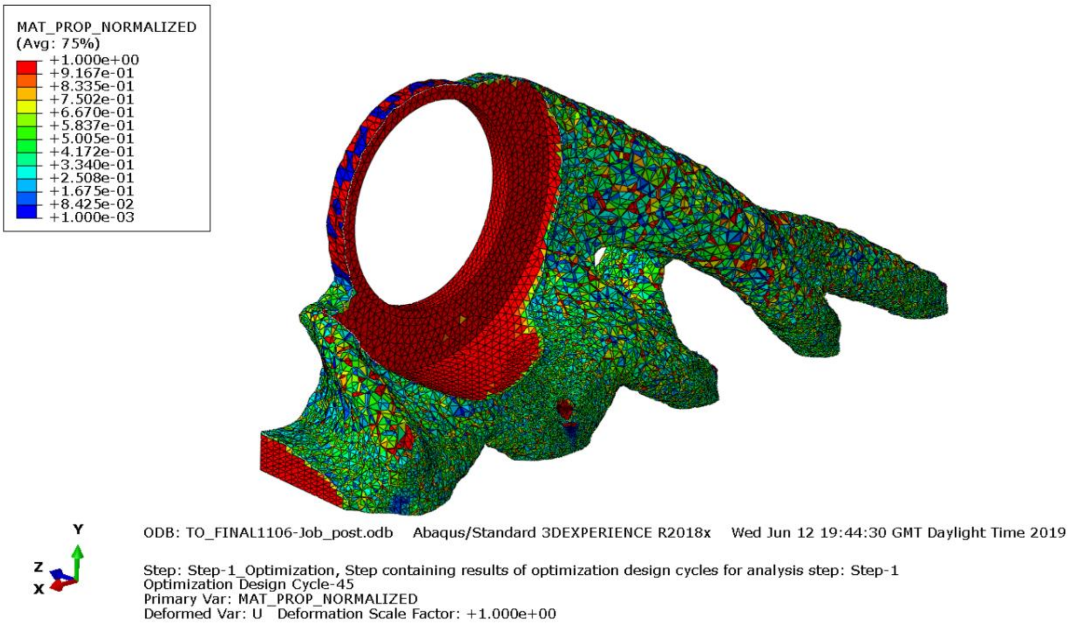

Figure 40 - Extracted geometry from Abaqus (ISO-value=0.5)

After the extraction of the resulting STL (file only contains the surface contour of the part), file it is essential to interpret the geometry shape and avoid sharp edges, which will act as stress concentration areas. These areas may affect the fatigue strength of the component. For that reason, it is necessary to smooth and refine some areas of the part; this was performed using the Netfabb software. This is an iterative process, because after smoothing the part, a static analysis is perfomed in order to verify the stress concentration areas, which have to be smoothed again. Figures 41 and 42 show the most important areas that were smoothed by magnifying them before and after the process.

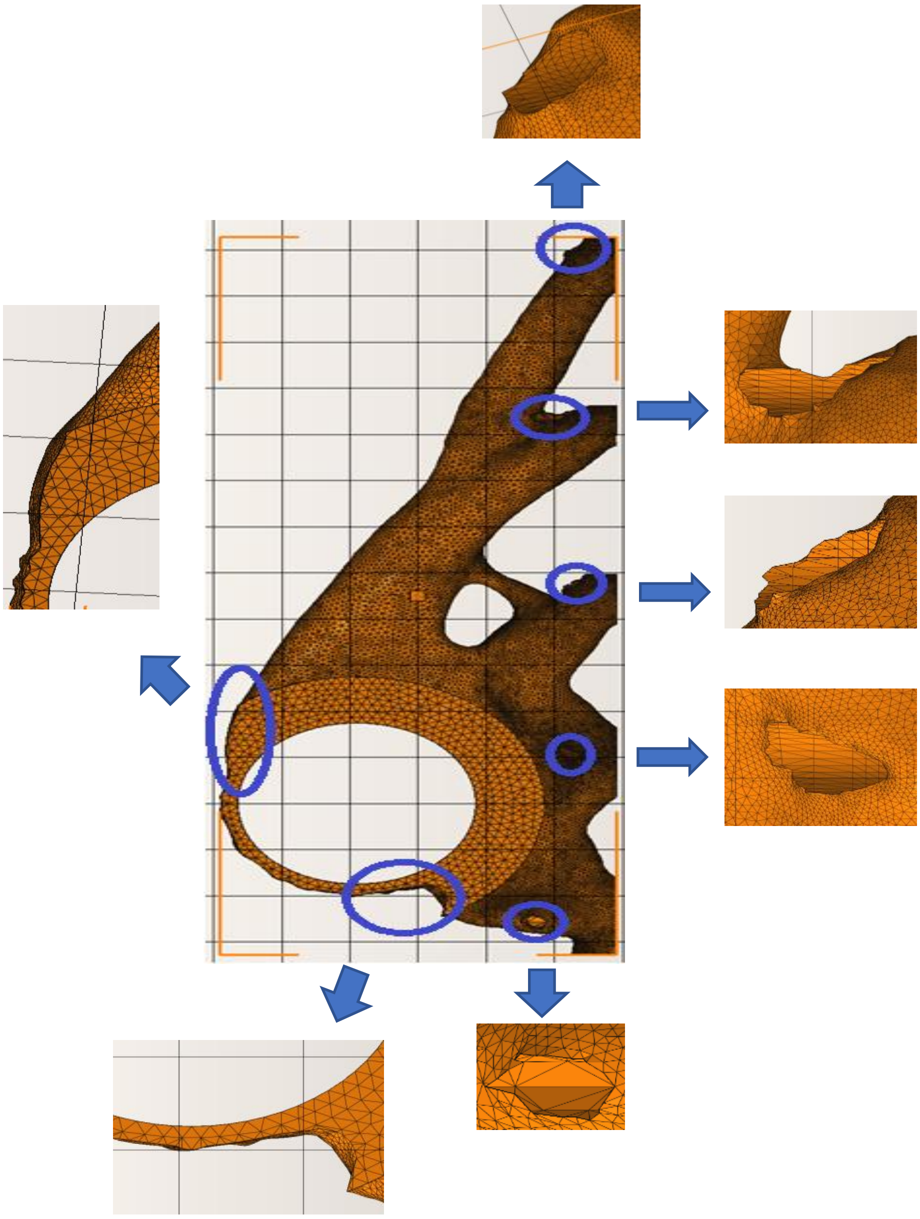

Figure 41 - Topology optimization result before smoothing

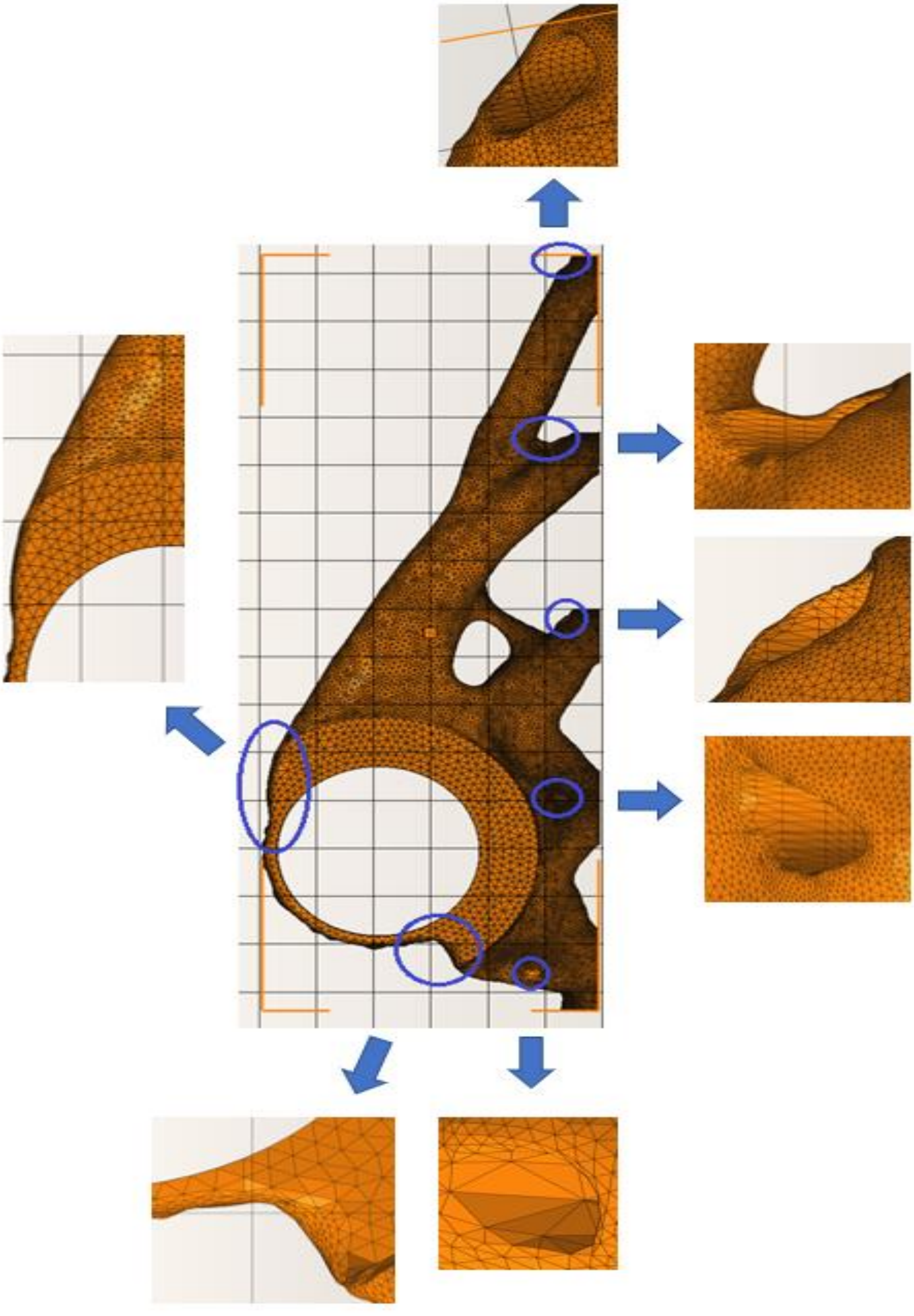

Figure 42 - Post-Smoothing results of TO

After the STL repair using Netfabb, which was useful for rounding sharp edges, the geometry of the part was evaluated and since the external cyclic load is transmitted on the central hole, it was indispensable to reinforce the material around the hole, in order to avoid an high stress concentration in that area and distribute the stress to other part areas. The algorithm optimization does not reinforced this area since the constraint does not take into account fatigue resistance and only respond to the applied load. For this purpose, it was performed an extrusion adding material around the hole as the arrows point out in Figure 43.

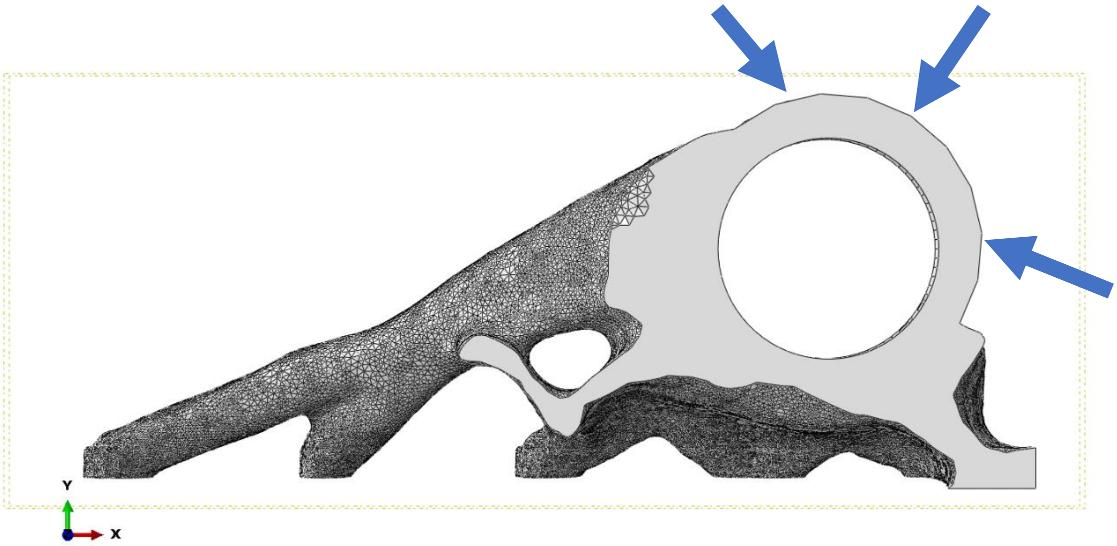

Figure 43 - Reverse engineering of the topology optimization result

The mass properties, stiffness and stiffness-to-mass ratio is presented in Table 6.

Table 6 - Final geometry properties

	Initial Geometry	***Final Geometry***
Mass (g)	2100	263
Stiffness (N/mm)	$1.93\text{x}10^5$	$1.44\text{x}10^5$
Stiffness to weight ratio (N/mm*g)	92	549

The mass was reduced to 12.53 %. This value is different from the constraint in topology optimization. This discrepancy can be explained because the workpiece was submitted to reverse engineering that added material to the part as well as the design domain considered, was not the totality of the part (some regions were "frozen" and material could not be removed there).

For calculating the stiffness of the bracket, a static analysis for both geometries (before and after the optimization) was performed, where it was extracted values from displacement in a selected point, positioned in the external part of the ring, in the symmetry plan, characterized by a vector (connecting the point to the centre of the circle). This point was selected in the farthest point of the load.

The stiffness achieved for both geometries had a differential of 25.39% and since for stiffness-to-weight ratio, only the mass changes significantly, this ratio is significantly higher for the final geometry, compared to the initial one.

After achieving a final geometry, cyclic simulation was performed in order to evaluate the most critical areas with higher stress concentrations. The plot of equivalent stress is presented in the Figure 44.

Figure 44 - Static analysis of the final optimized support

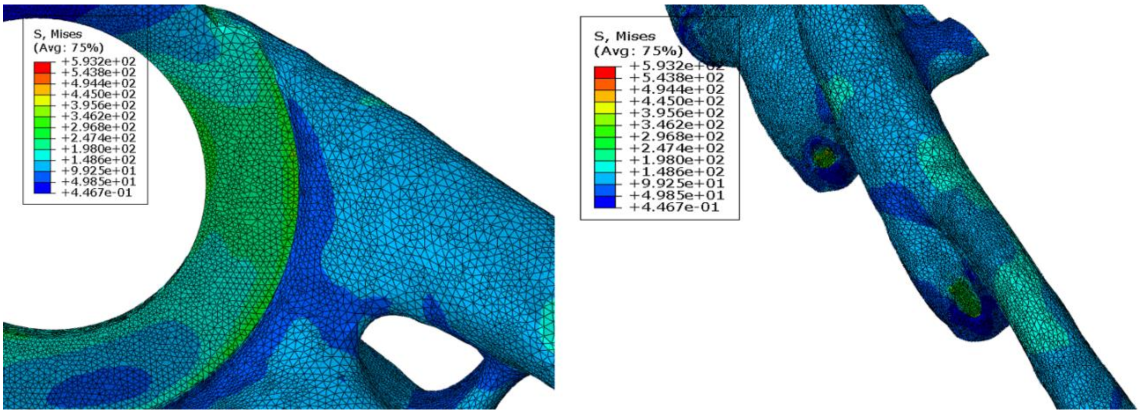

Figure 45 - Stress concentration areas

Figure 45 shows high stress concentration areas around the hole where the load is applied. These stresses are about 200-400 MPa. In one of the arms of the bracket, there are other stress concentrations, with lower values.

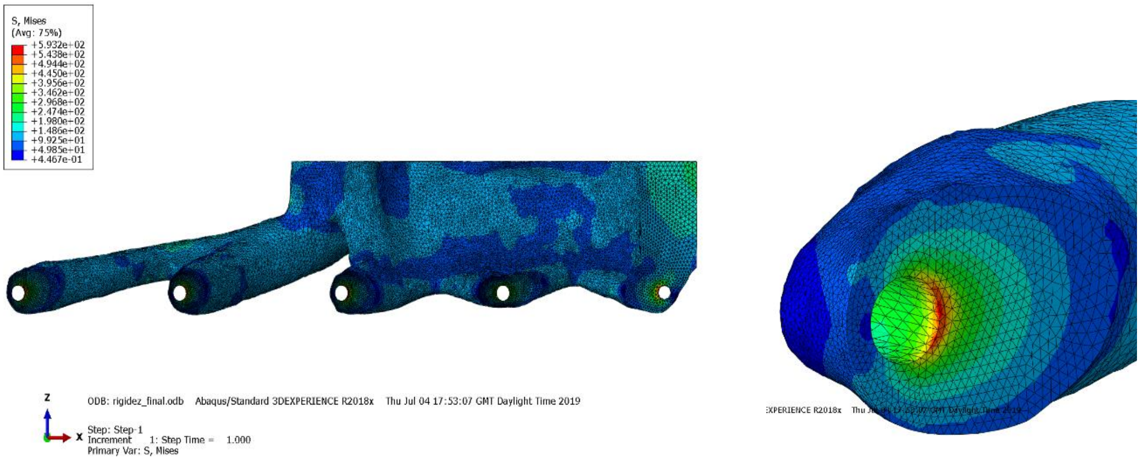

Figure 46 - Stress distribution in holes

In Figure 46 is possible to detect a peak on the stress results in the bolt holes. These results can be caused by the simplistic model used for the bolted joints. This approximation was used due to the lower computational cost, which is very high in topology optimization, despite increasing the local stiffness. This method does not take into account the fasteners pre-load and, above all, the contact between the different elements of the connection, which would improve the distribution of loads.

Figure 47 shows the displacement field which is higher in the upper section of the part and Figure 48 exhibits the final geometry of the case-study.

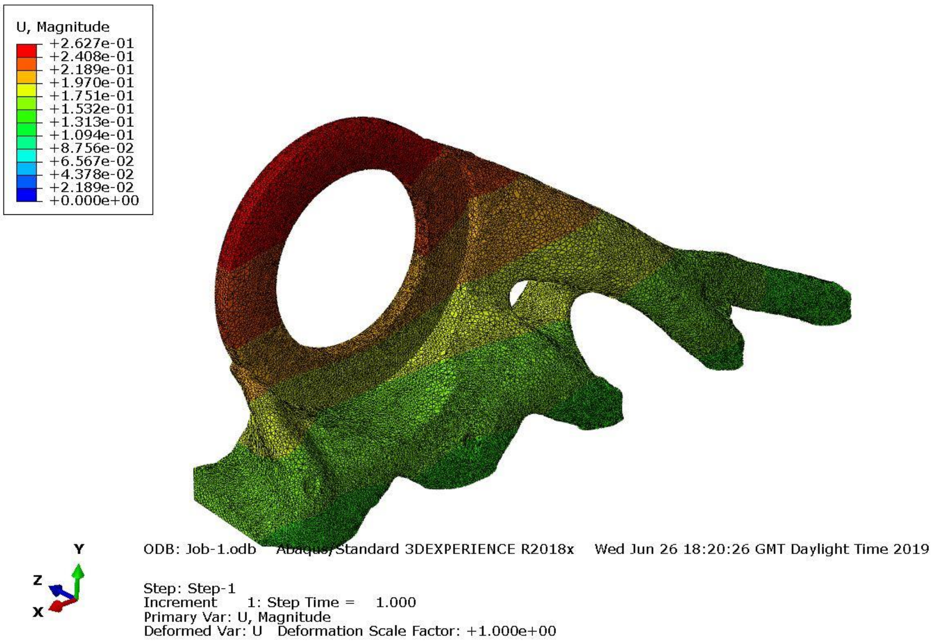

Figure 47 - Displacement field of the part

Figure 48 - Final Geometry of the case-study part

5.2 Additive manufacturing results

Before simulating the final optimized geometry of the bracket, convergence studies for different mesh sizes were performed using a preliminary topology optimized workpiece (it is important to emphasize that the workpieces used in these convergency studies here was not the final one, but had a very similar geometry). For each mesh size, it was obtained results for the displacements in z direction were computed since it takes an important role by control the powder layer thickness and the accumulation of the cross-sectional area [81, 82], besides putting in risk the manufacturability of the part with a possible collision with the recoater as it is explained below. In addition, the maximum Von Mises stresses, as well as the maximum and minimum normal stresses on coordinate axis directions, S_{xx}, S_{yy}, S_{zz}, were computed. These supplementary results will be presented in Appendix B.

For each mesh size, it was simulated three building orientations of the part. The results will be analysed for each orientation varying the mesh size; this is performed in order to analyse the convergence of the mesh. The orientation 1 is in the normal building direction (base surface parallel to the baseplate). The orientation 2 is a 90º rotated part in x-axis. The last orientation is the normal building direction 90º rotated in y axis. These three orientations are illustrated in the Figure 49.

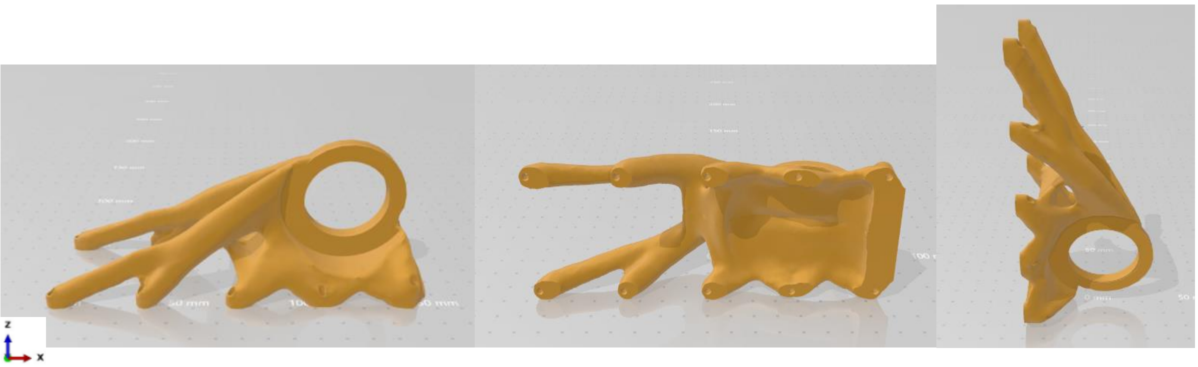

Figure 49- Orientations of the part used in AM simulation: 1(left),2(middle),3(right)

The mesh sizes simulated showed 3 different element sizes: 1.5 mm ; 1mm ; 0.75mm. These meshes will be respectively assigned the names: Mesh 1.5, Mesh 1 and Mesh 0.75.

After finishing melting the selected regions of a layer, a new powder film is spread above the previous manufactured layer. This process is done by a recoater. The depth of this powder layer is known as “layer thickness”, and for the present case is 50 μm. As explained before, due to the thermal gradients involved in the AM process, distortions will occur during the process. After building a layer, if the deformations on z-direction (build direction) are larger than the powder layer thickness, when the recoater moves to deposit another powder layer, it can collide with the workpiece and might break, damage or even rip out the part.

For orientation 1 the results of maximum z-displacement, during the building process for each z coordinate depending on the mesh size are presented in Figure 50.

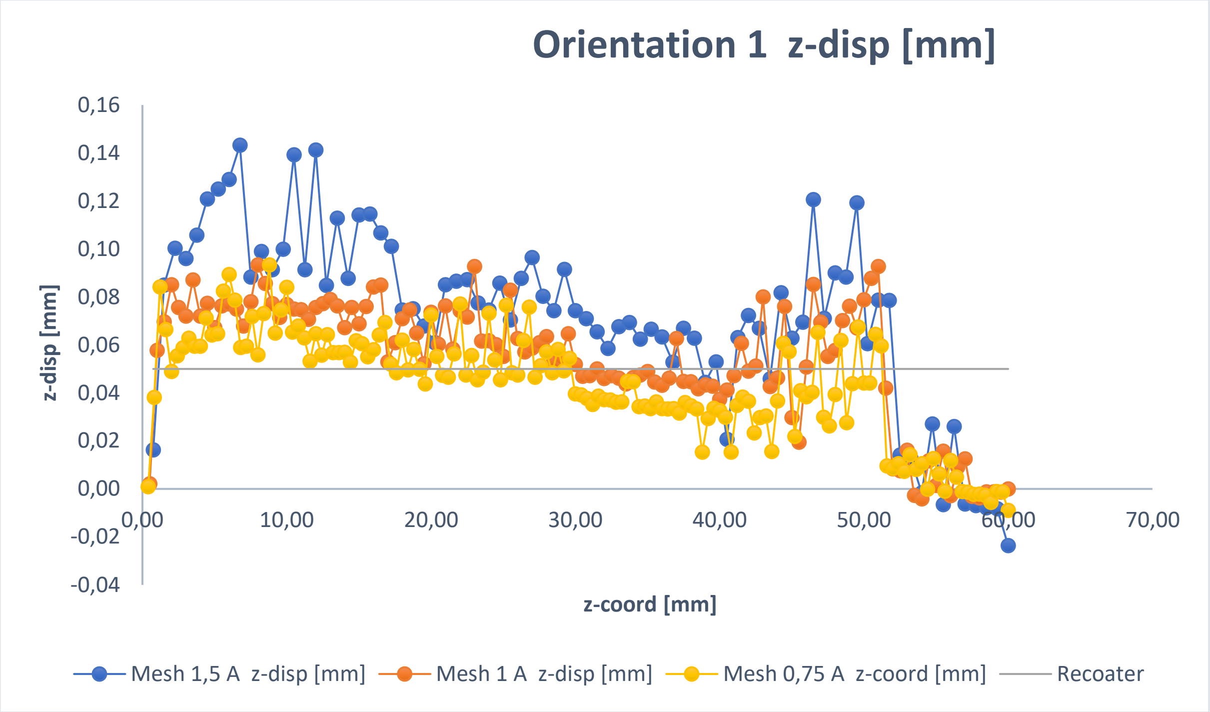

Figure 50 – Maximum z-displacement in function of z-coordinate for Orientation 1

From the analysis of the Figure above, the Mesh 1.5 show higher values of z-displacement while the Mesh 0.75 present the better results since its deformations are at almost z-coordinates below the set recoater.

For orientation 2 the maximum results of z-displacement, during the building process for each z coordinate depending on the mesh size, are presented in Figure 51.

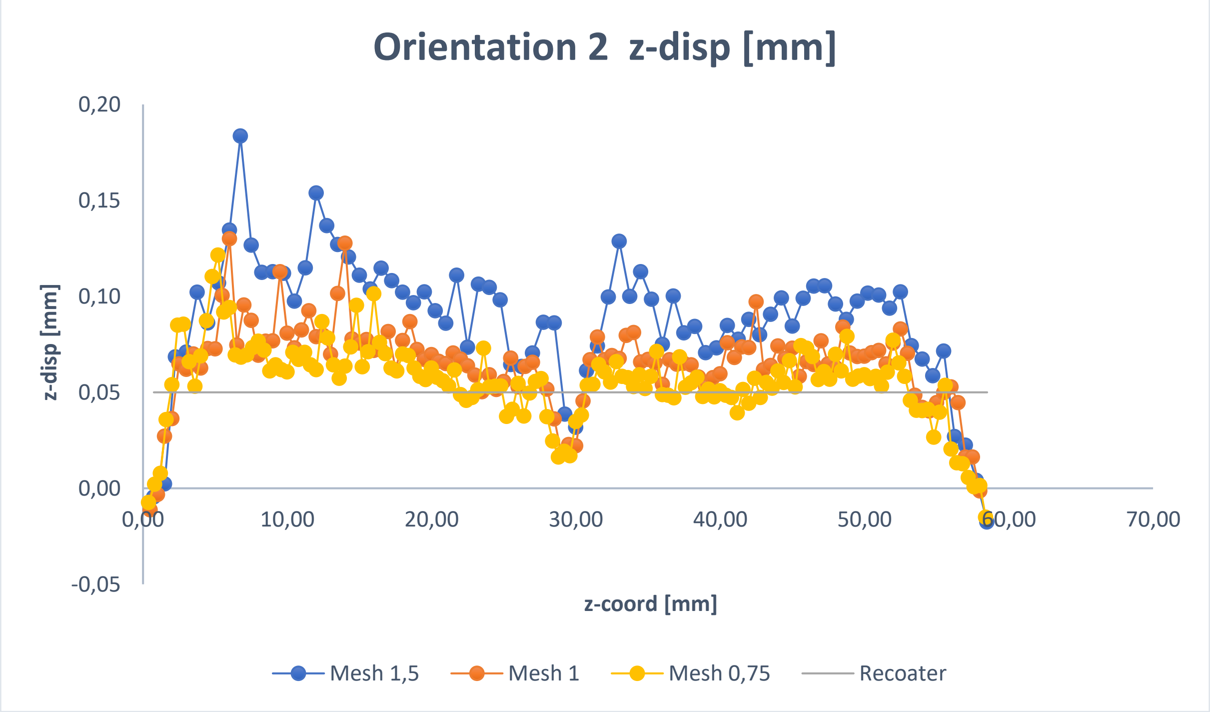

Figure 51 - Maximum z-displacement in function of z-coordinate for Orientation 2

From the Figure 51 it is verified that, for orientation 2, almost the same results are achieved compared to the orientation 1. As long as the mesh is refined, the results of maximum z-displacement tends to decrease. Even for the more refined mesh (Mesh 0.75) the values are almost above the set recoater what can induce problems already discussed.

For orientation 3 the results of maximum z-displacement, during the building process for each z coordinate depending on the mesh size, are presented in Figure 52.

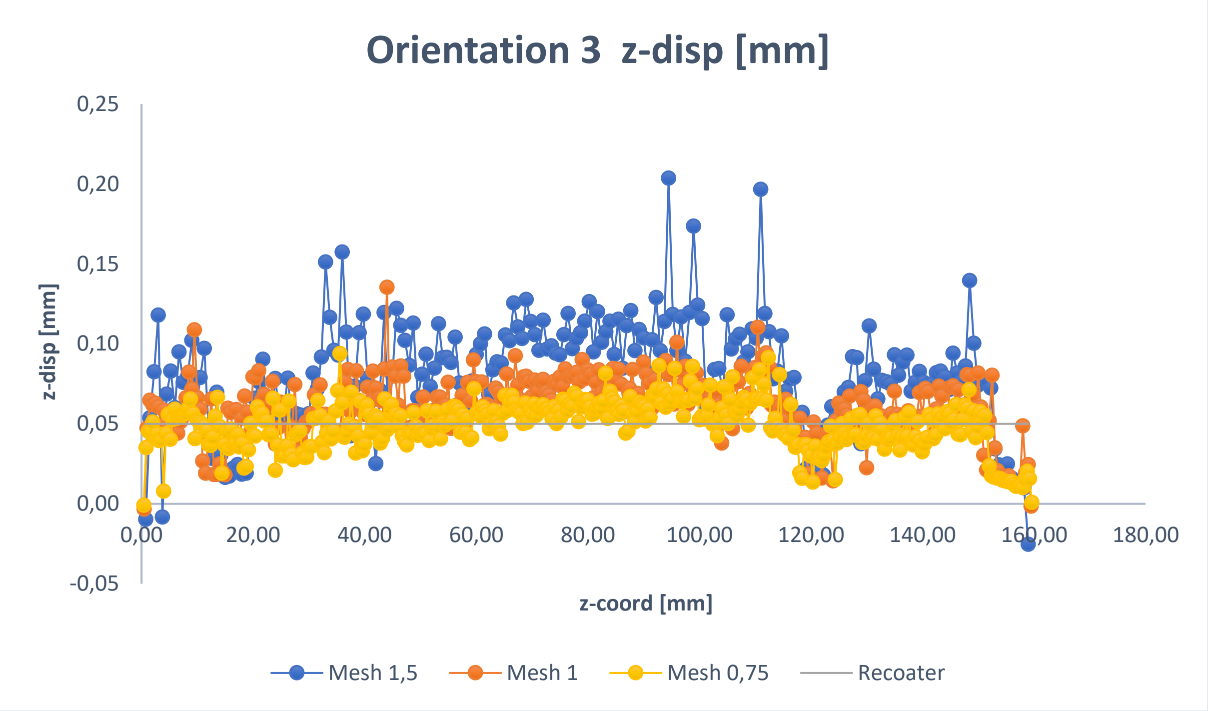

Figure 52 - Maximum z-displacement in function of z-coordinate for Orientation 3

For orientation 3, it is possible to infer that Mesh 1.5 presents the higher values similar to the previous results while the other two have closer results. In this orientation, the number of layers are higher due to the higher length of the part in z-direction, thus, there are more points analysed.

For a better understand of the results, three graphs (Figure 53; Figure 54; Figure 55) for the three different meshes were plotted with the maximum (MAX), average (AVG) and minimum (MIN) results.

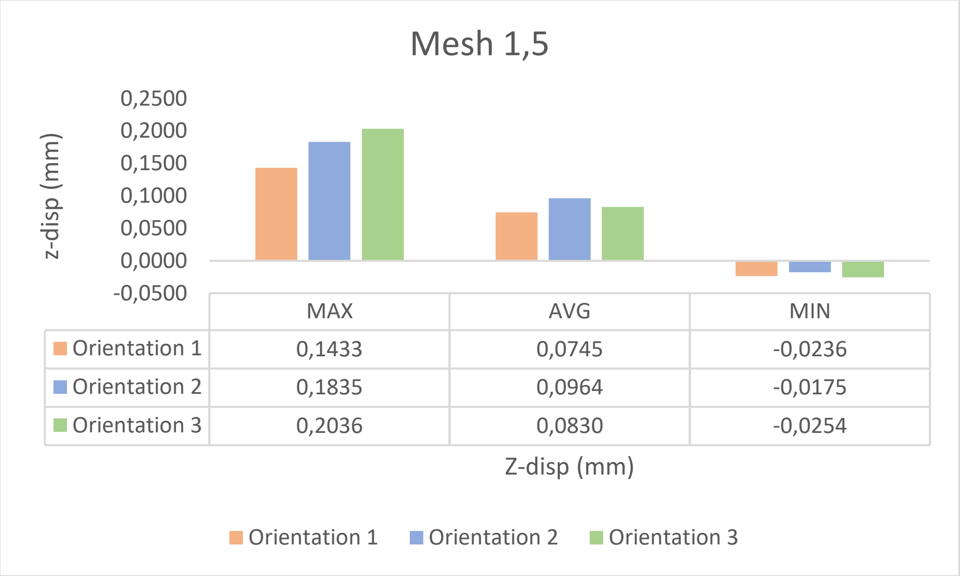

	MAX	AVG	MIN
Orientation 1	0,1433	0,0745	-0,0236
Orientation 2	0,1835	0,0964	-0,0175
Orientation 3	0,2036	0,0830	-0,0254

Figure 53 - Maximum, Average and Minimum values for z-displacement for Mesh 1.5

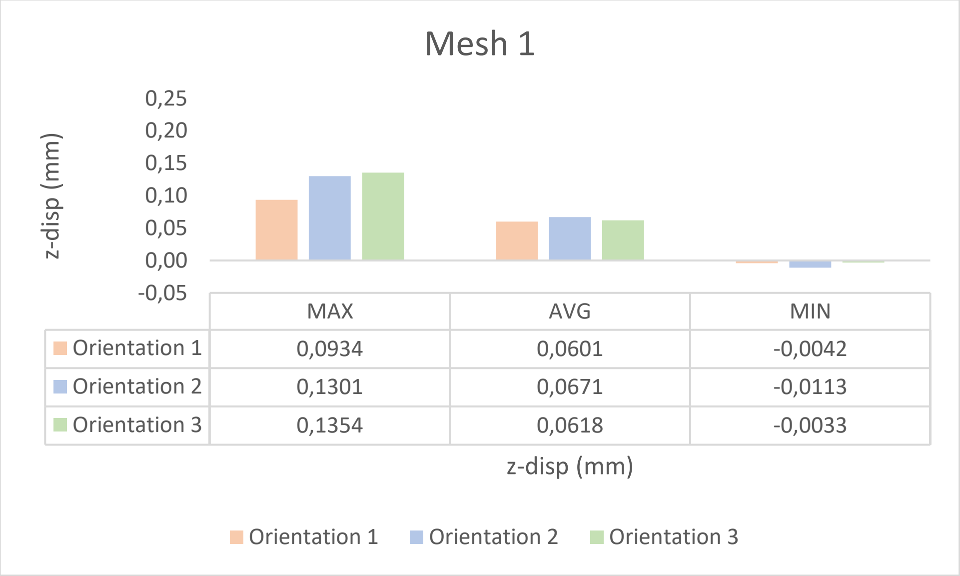

	MAX	AVG	MIN
Orientation 1	0,0934	0,0601	-0,0042
Orientation 2	0,1301	0,0671	-0,0113
Orientation 3	0,1354	0,0618	-0,0033

Figure 54 - Maximum, Average and Minimum values for z-displacement for Mesh 1

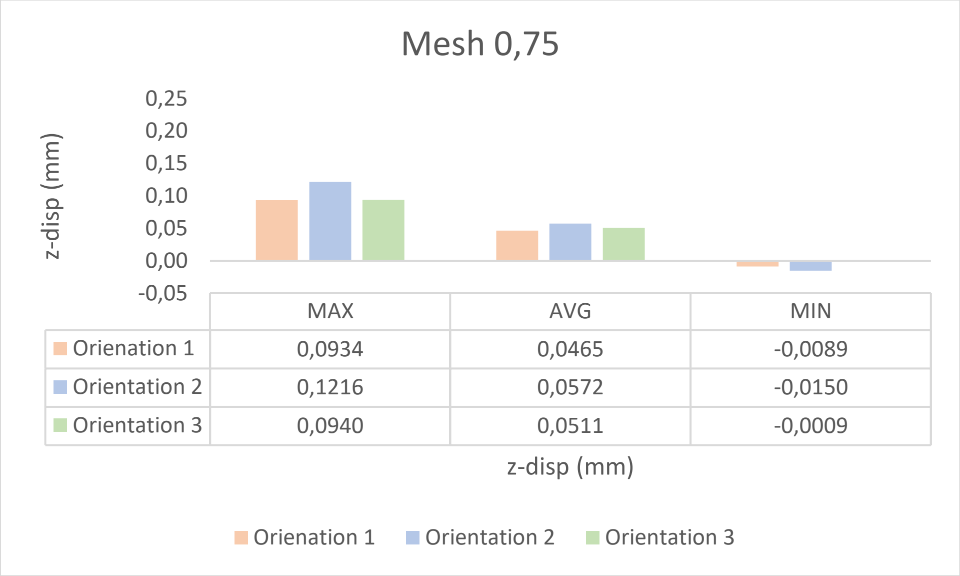

	MAX	AVG	MIN
Orienation 1	0,0934	0,0465	-0,0089
Orientation 2	0,1216	0,0572	-0,0150
Orientation 3	0,0940	0,0511	-0,0009

Figure 55 - Maximum, Average and Minimum values for z-displacement for Mesh 0.75

From the analysis of these three plots, it is deduced that the z-displacement converge since the difference between the values of the Mesh 0.75 to the Mesh 1 are smaller than the differences between the results of Mesh 1 to Mesh 1.5. The results for Mesh 1.5 have maximums for the three orientations incomparably higher than for the others. For example, for orientation 1, the result of the maximum z-displacement for mesh 1.5 is around 0.14 while for the other meshes the result converge for 0.0934.

To avoid the problems with recoater collisions it can be used soft recoaters that allows the recoater itself to deform and it does not need to stop the build. Other techniques can be used, such as rotating the part to avoid being parallel to the recoater, which would become more difficult for the recoater passage. If it is rotated 45 degrees around z-axis, the recoater doesn’t need to pass through a wall with two corners at a time which reduces the crash probability. Other technique is to avoid putting parts behind each other because if the recoater touches some part it has no influence in the other parts[83]. Caelers, M. [84] did a study where it was monitored the building process, based on sensors, to avoid collisions between the part and the recoater.

For the final geometry achieved, the simulation of the manufacturing process included results for the three stages of the production. The distortions during the building of the part (stage 1), after releasing the baseplate from the machine (Stage 2) and after removing the workpiece from the baseplate (Stage 3) were analysed. Since the baseplate is stiff, the Stage 2 (releasing the baseplate and workpiece set from the machine) has not much influence on the residual stresses of the part (the baseplate has very small deformations during the Stage 1) and are very similar to Stage 1. Therefore, it will only be presented results regarding Stage 1 and 3.

The following results are relative to finer mesh, the smallest element length simulated, a mesh size of 0.5 with a lumping factor of 5 and will be presented for each direction for the selected stages. The lumping factor results from an attempt to improve the computational time, joining a number of processed layers into one simulation layer.

For orientation 1, Figure 56 provides the Von Mises stresses distribution on Stage 1 and 3. For the building process, the external stresses are very high in nearly every areas. When the baseplate is removed the maximum stresses decrease from 300 to 280 MPa what is linked to the increase of deformations due to the removal of a boundary condition. For the workpiece removed from the base plate, it is possible to see higher stress concentrations around the big hole and in the two long narrow areas.

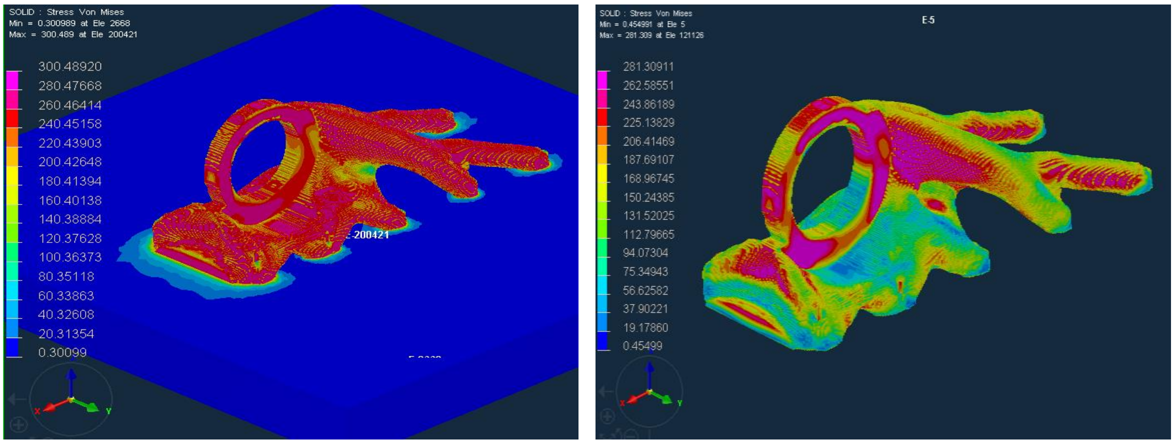

Figure 56 - Von Mises distribution for Orientation 1, Stages 1 and 3 (final optimized geometry and refined mesh)

For orientation 2, the Von Mises stresses distribution on Stage 1 and 3 is shown in Figure 57. For stage 1, the surface stresses are very high everywhere, except for some areas beneath the body part. When the baseplate is removed the maximum stresses decrease from 316 to 285 MPa. For the workpiece removed from the base plate, high stresses are shown in the bottom and in the ring.

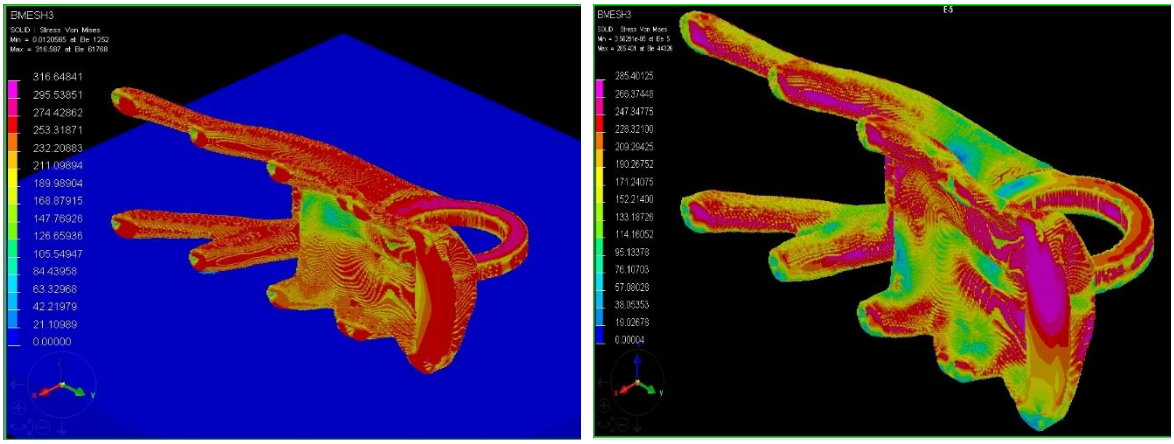

Figure 57 - Von Mises distribution for Orientation 2, Stages 1 and 3 (final optimized geometry and refined mesh)

For orientation 3, the Figure 58 provides the Von Mises stress distribution on same stages. For the building process, the surface stresses are very high almost everywhere except in the areas in the bottom of the ring. When the baseplate is removed the maximum stresses decrease from 316 to 283 MPa. For the workpiece removed from the base plate, high stresses are shown in the hole and in the supports direction.

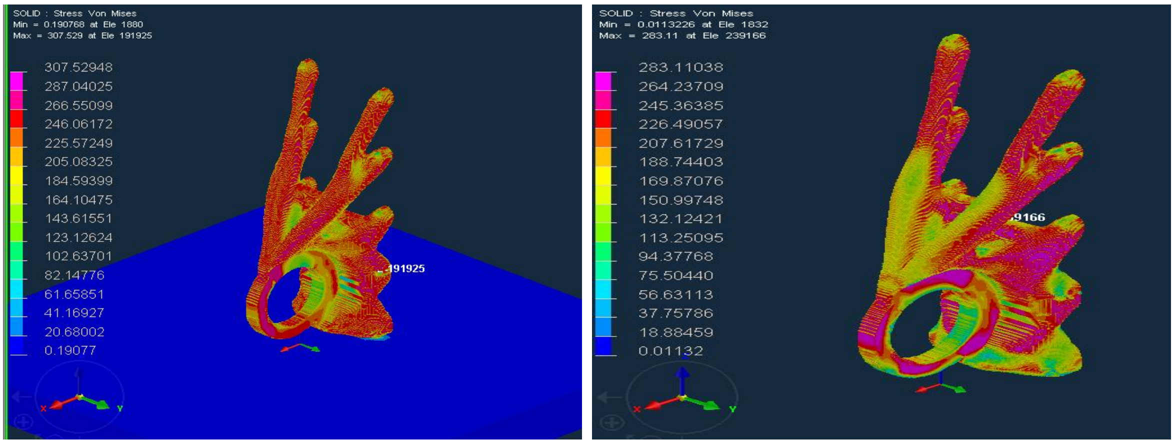

Figure 58 - Von Mises distribution for Orientation 3, Stages 1 and 3 (final optimized geometry and refined mesh)

A plot with the maximum Von Mises stresses was done to better represent the results (Figure 59).

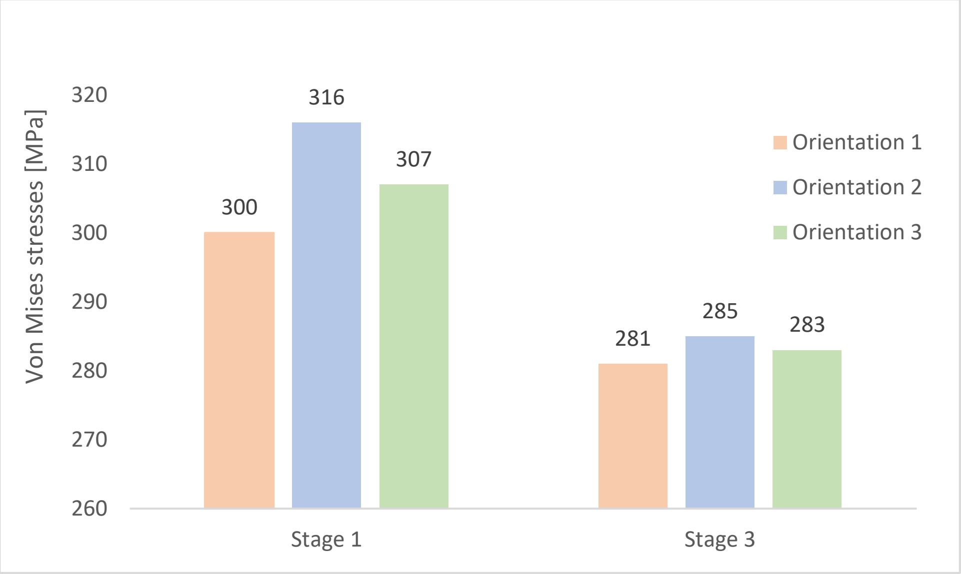

Figure 59 - Maximum Von Mises stresses for each orientation and stage

It is possible to infer from the results that, as the baseplate is extracted from the part it will result in a stress relief for every orientation. The orientation 1 has the lowest Von Mises maximum stress and the orientation 2 the highest. The variation for Orientation 1 is 6.76%, for Orientation 2 is 10.88 % and for Orientation 3 is 8.48% comparing the results for the considered stages (1 and 3).

In Figure 60, it is performed a cut view in the X-Z plan showing the first principal stress of the building part (during stage 1), where the compressive stresses inside the building part is visible (displayed in blue) comparing with the exterior tensile stresses shown in green.

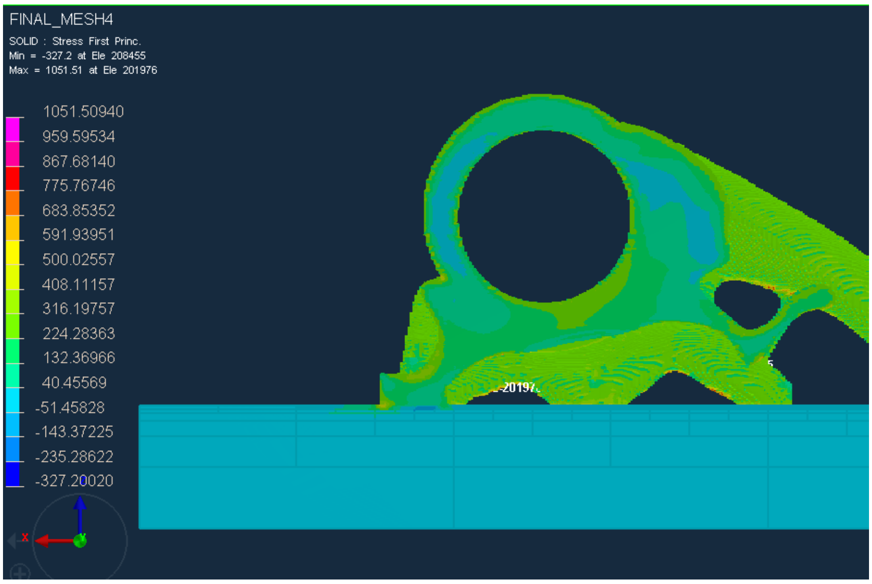

Figure 60 - Detail of interior compressive stresses

5.3 Fatigue assessment

For the fatigue assessment it was firstly defined a cyclic analysis with a load ratio, R=-1 conducted on ABAQUS in order to compute the alternate stress. The mean stresses were considered the ones resulting from the simulation of the additive manufacture process simulation conducted on ESI. For each simulation, 3 critical points, based on the stress distribution obtained by ABAQUS, discarding the five holes stress values. For the cyclic analysis, it was chosen the first three points since there were high stress concentrations at the origin of the symmetry (Point 1), around the hole taking the transition to the parts body (Point 2), and in the leg corresponding to the farthest fastener from the load point (Point 3). These 3 first points will be analyzed for each orientation (Figure 61).

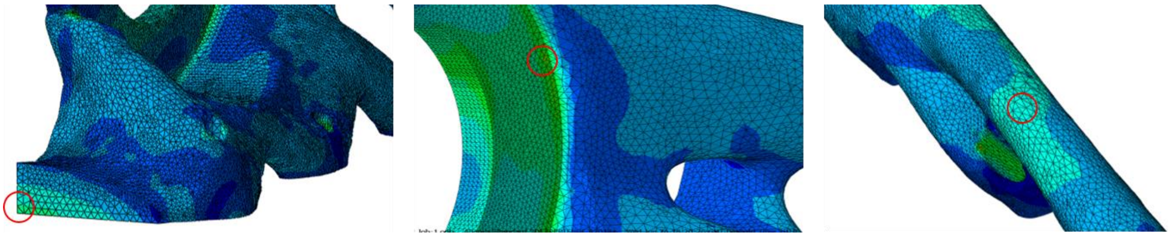

Figure 61 – Von Mises stress distribution to choose the points 1,2,3

For the mean stresses, it was set as critical points for Orientation 1, the points 4,5 and 6 based on high residual stresses (Figure 62). These points were chosen only attending the AM simulation and are not linked with the points taken from ABAQUS.

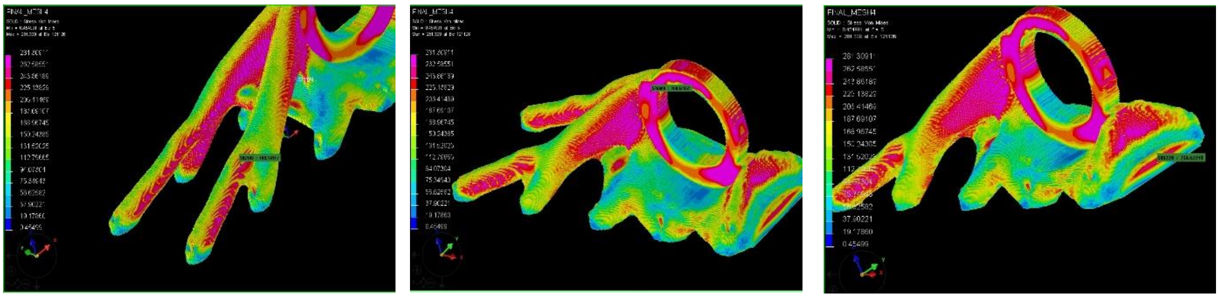

Figure 62 - Von Mises stress distribution to choose the points 4,5,6

For the same reasons, for Orientation 2, the points 7,8 and 9 were chosen as well as for the Orientation 3, the points 10,11,12. This is not the ideal method, but, since the ESI and ABAQUS models have different meshes, the overlap of the points would be extremely difficult. These points, corresponding to the closest nodes of each software, are shown in the Figure 63.

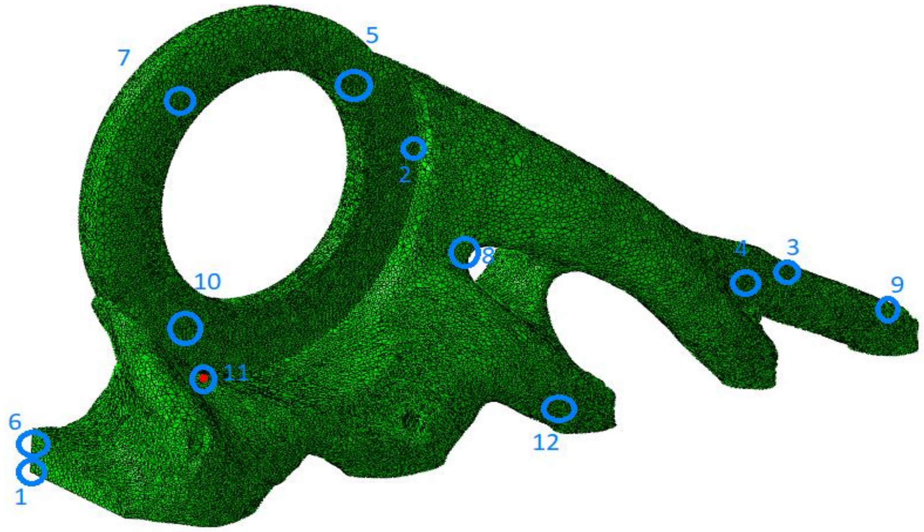

Figure 63 - Critical points provided by high stress areas resulting from Abaqus and ESI simulations

Stress-based criteria are based on equivalent stresses approaches. The most commonly used for fatigue are the maximum principal stress theory, the maximum shear stress theory (Tresca) and the octahedral shear stress theory (Von Mises) (equations. 5.1; 5.2 and 5.3).

Maximum principal stress:

$$S_{qa} = S_{a1} \tag{5.1}$$

Maximum shear stress:

$$S_{qa} = S_{a1} - S_{a3} \tag{5.2}$$

Octahedral shear stress:

$$S_{qa} = \frac{1}{\sqrt{2}} * \sqrt{((S_{a1} - S_{a2})^2 + (S_{a2} - S_{a3})^2 + (S_{a3} - S_{a1})^2)} \tag{5.3}$$

where $S_{a1} > S_{a2} > S_{a3}$,

Despite being the most used method, it does not take into consideration the beneficial effects or detrimental effects of possible compressive or tensile principal stresses. To solve these type of problems, one may consider the sum of the principal mean normal stresses [56]:

$$S_{qm} = S_{m1} + S_{m2} + S_{m3} \tag{5.4}$$

This formulation suggest that is possible to cancel out the effect of a tensile mean stress acting in one direction by other compressive mean stress acting in another direction, which is not experimentally true.

One method that combines these two formulations is the Sines method[85] that is represented by:

$$\sqrt{((S_{a1} - S_{a2})^2 + (S_{a2} - S_{a3})^2 + (S_{a3} - S_{a1})^2)} + m * (S_{m1} + S_{m2} + S_{m3}) = \sqrt{2} S_{Nf}$$

where m is the coefficient of mean stress, normally 0.5 [56]

For each point it was extracted the results of the cyclic loading simulation and the stresses resulting from the SLM process in the corresponding orientation but for the first three critical points resulting from the cyclic loading.

The alternating stresses obtained are result from a stress range value for each cycle; the principal stresses for the higher and lower tension peaks and only the range of these values was considered. These results were extracted for all the points (the first 3 chosen on ABAQUS and the last 9 chosen on ESI)

For example, Figure 64 shows the peaks of the First, Second and Third principal stresses, for point 2.

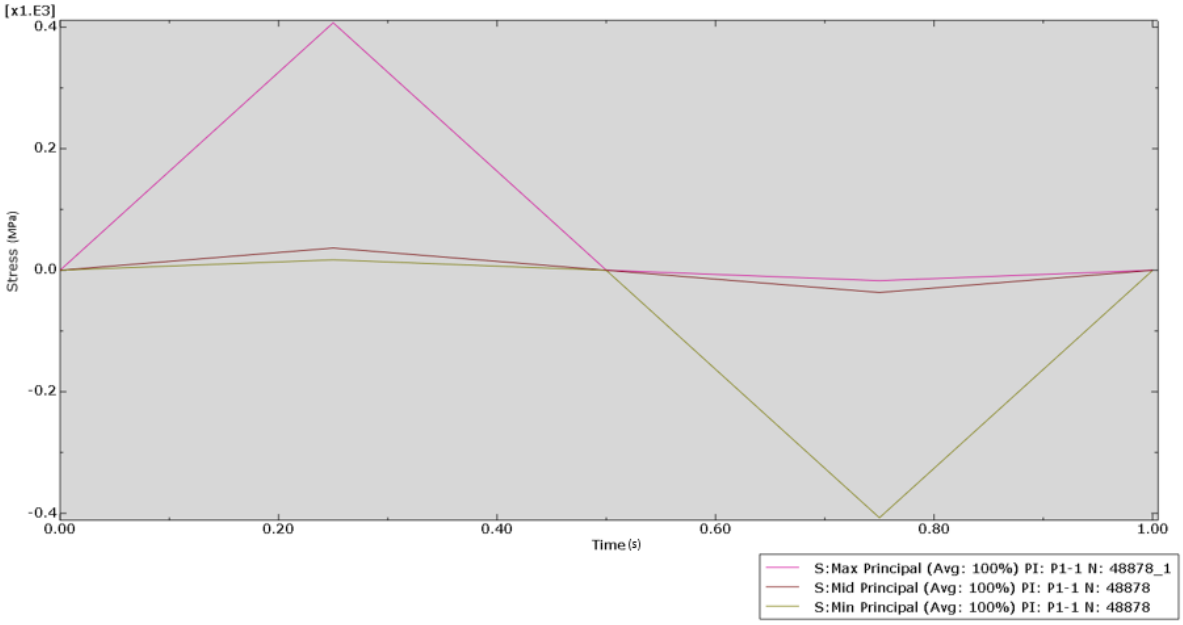

Figure 64 - First, Second and third principal stresses of one cycle

The results of principal stresses corresponding to alternating stress obtained from ABAQUS are shown in table 7.

Table 7 - Principal Stresses and the equivalent stresses for the selected critical points

	First Principal (MPa)	***Second Principal (MPa)***	***Third Principal (MPa)***	***Equivalent Alternating Stress (MPa)***
Point 1	214.8	2.8	216.1	300.8
Point 2	424.6	73.2	424.6	497.0
Point 3	172.3	2.5	173.1	240.8
Point 4	109.3	0.2	109.0	154.0
Point 5	134.6	0.4	134.1	190.0
Point 6	140.5	1.2	139.5	196.2
Point 7	3.8	0.2	3.7	4.9
Point 8	-74.7	-11.5	-77.3	91.2
Point 9	101.8	0.4	99.0	141.5
Point 10	-91.5	0	-90.1	128.4
Point 11	60.3	4.8	-57.0	143.8
Point 12	107.2	-1.9	107.7	154.6

For the same critical points, the mean stresses resulting from the additive manufacturing building simulation, are shown in table 8. These points corresponds to the same before analyzed in ABAQUS.

Table 8 - Principal Stresses, Equivalent mean nominal stresses as well as the Sines values at selected critical points

Orientation 1	***First Principal (MPa)***	***Second Principal (MPa)***	***Third Principal (MPa)***	***Equivalent mean nominal stress (MPa)***	***Sines method (MPa)***
Point 1	218.7	141.1	82.6	442.4	369.1
Point 2	222.6	8.7	-41.5	189.8	418.5
Point 3	119.8	-21.4	-41.1	57.3	190.5
Point 4	189.5	-69.9	-85.1	34.4	121.1
Point 5	292.9	56.5	-0.7	348.7	257.3
Point 6	249.6	-2.9	-11.0	235.6	222.1
Orientation 2					
Point 1	245.3	9.9	-0.1	255.0	302.9
Point 2	-10.9	-37.4	-109.0	-157.7	295.7
Point 3	233.4	24.8	5.8	264.1	263.6
Point 7	270.1	168.3	-0.3	438.1	158.4
Point 8	0.4	-27.1	-279.2	-305.9	-43.7
Point 9	267.7	9.8	-7.5	269.9	195.5
Orientation 3					
Point 1	115.3	99.5	7.2	222.1	291.2
Point 2	227.1	7.5	-40.7	193.8	419.9
Point 3	343.6	129.3	44.3	517.1	353.1
Point 10	283.5	31.8	-0.5	314.8	202.1
Point 11	285.6	41.0	0.2	326.9	217.2
Point 12	288.4	108.7	-18.4	378.7	243.2

The Sines methods results combines the values resulting from the equivalent stress resulting from the alternating stress and the sum of the values of the principal stresses expressed on Table 8 multiplied by the *m* parameter set at 0.5[56] expressed as equivalent mean nominal stress.

The final goal corresponding to the achievement of the number of cycles in each point according to each orientation is obtained by the application of the SN curve of the material, shown in Figure 21 with the following parameters (eq 5.4)

$$S = C * N^{m} \tag{5.4}$$

with C=1139.1 and m=-0.101 from reference [71]

For each orientation, it was obtained the following number of cycles, expressed in Table 9. Since the points 4, 6, 7, 9, 10 and 11 present a number of cycles over 10^7, they are considered as infinite life points.

Table 9 - Number of cycles for the critical points of each orientation considering the effect of mean stresses

Orientation 1	***Number of cycles (N_f)***
Point 1	7.0×10^4
Point 2	2.0×10^4
Point 3	4.9×10^7
Point 4	4.3×10^9
Point 5	2.5×10^6
Point 6	1.1×10^7
Orientation 2	
Point 1	5.0×10^5
Point 2	6.3×10^5
Point 3	2.0×10^6
Point 7	3.0×10^8
Point 8	Infinite life
Point 9	3.8×10^7
Orientation 3	
Point 1	7.3×10^5
Point 2	2.0×10^4
Point 3	1.1×10^5
Point 10	2.7×10^7
Point 11	1.3×10^7
Point 12	4.4×10^6

The number of cycles not considering the influence of the mean stresses during construction, in other words, equivalent to produce parts by manufacturing processes where the residual stresses are very low and can be negligible, are also presented in Table 10.

Table 10 - Number of cycles for the critical points of each orientation considering only the effects of the alternating stresses

Orientation 1	***Number of cycles (N_f)***
Point 1	$1.6x10^{7}$
Point 2	$1.1x10^{5}$
Point 3	$1.5x10^{8}$
Point 4	$1.2x10^{10}$
Point 5	$1.6x10^{9}$
Point 6	$1.1x10^{9}$
Orientation 2	
Point 1	$1.6x10^{7}$
Point 2	$1.1x10^{5}$
Point 3	$1.5x10^{8}$
Point 7	$7.7x10^{24}$
Point 8	$2.2x10^{12}$
Point 9	$2.9x10^{10}$
Orientation 3	
Point 1	$1.6x10^{7}$
Point 2	$1.1x10^{5}$
Point 3	$1.5x10^{8}$
Point 10	$7.5x10^{10}$
Point 11	$2.5x10^{10}$
Point 12	$1.2x10^{10}$

For a better understanding of the mean stresses influence it is presented the S-N curve and the corresponding points considering or not the residual stresses of the AM, for each orientation (Figures 65; 66; 67).

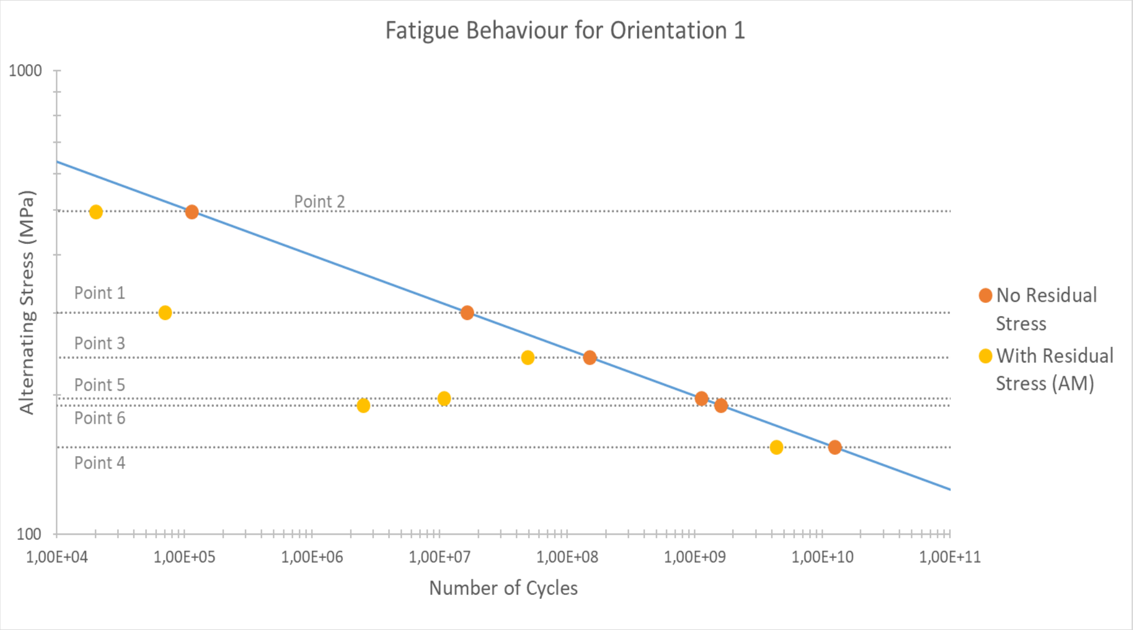

Figure 65 - SN curve considering the alternating stress points and the mean stresses for orientation 1

For orientation 1, all the points considering residual stresses have less fatigue life compared to the ones not considering their effects. The effect of the residual stresses varies from point to point but have a higher impact on points 1 and 6. Despite this analysis, the most critical point is the point 2 because it has the lowest fatigue life ($N_f = 2.0x10^4$) and determines the fatigue resistance of the whole part built in orientation 1.

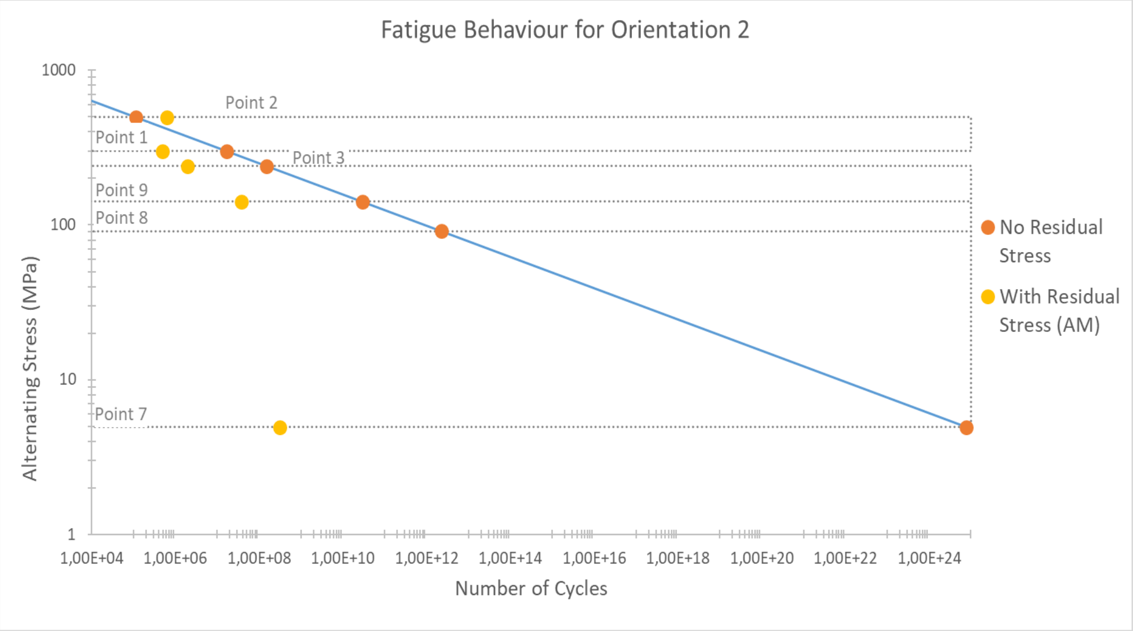

Figure 66 - SN curve considering the alternating stress points and the mean stresses for orientation 2

For orientation 2, the critical point changes to the point 1 (N_f = 5,0E+05) since the equivalent mean nominal stress for the point 2 acts as a compressive stress (-157,67). This means that, despite having a higher alternating stress than Point 1, the residual stress effect is beneficial and increases the fatigue resistance in this point. For the whole part built in this orientation, the maximum number of cycles calculated for the critical point is 5,0E+05. For the point 8 the residual stresses are not considered since the Sines Method result was negative due to the compressive stresses that were higher (in absolute value) than the alternating stress and it is not possible to represent in the graph.

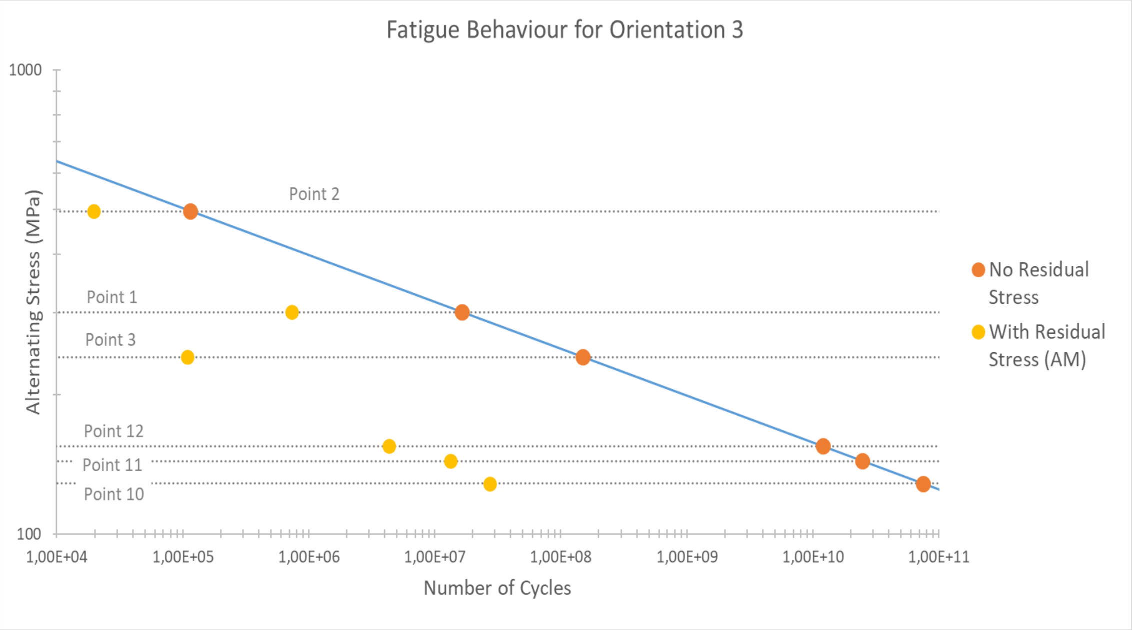

Figure 67 - SN curve considering the alternating stress points and the mean stresses for orientation 3

For orientation 3, the residual stresses of the considered points decrease the fatigue life of the part. The critical point is the point 2 ($2.0x10^4$ cycles). The points 10 and 11 are considered as infinite life because the number of cycles was above 10^7 cycles.

A overview of the problem shows that for orientations 1 and 3 the minimum number of cycles is $2.0x10^4$ cycles while for orientation 2 the minimum number of cycles is 5,0E+05 cycles. It is possible to deduce that the best orientation for building the part is the orientation 2 since it provides a higher number of cycles.

For orientations 1 and 3 the critical point is the Point 2 while for orientation 2, due to the effect of compressive residual stresses, the Point 1 is the critical one.

The benefits of a compressive equivalent mean nominal stress are also shown in the point 2 for orientation 2 where the results for the Sines method provides a higher number of cycles than for the equivalent alternating stress while for the tensile stresses of orientations 1 and 3, the number of cycles decrease when compared with the alternating stress

For the point 8 the compressive stresses of the equivalent mean nominal stress have a higher impact on the Sines method than the equivalent alternating stress. Because of this, the method provides a less than zero equivalent stress what cannot be expressed by the SN curve and it is set as infinite life, that’s why the lower alternating stress doesn’t have a corresponding point because the curve only represents positive stresses.

There is another point that must be mentioned since it was a critical point for the additive manufacturing simulation but had a very low alternating stress. This cause a very high number of cycles (7.7×10^{24} cycles) and it is shown in Figure 66.

For the represented values, since the major part of the equivalent mean nominal stress are positive values, these stresses often reduce the life of the part.

Many of the points considered as critical, assuming the values of mean stresses, presented a high number of cycles because the corresponding equivalent alternating stress was not so high and it has a decisive importance in these calculations.

6 Conclusions and Future works

6.1 Conclusions

The main goals of this work were:

1. Topology optimization of a selected part
2. Additive manufacturing simulation of the optimized part
3. Evaluation of the fatigue behaviour taking into account the service loads and the residual stresses effects from the manufacturing process

The topology optimization process suggests a new geometry for a selected part, in order to fulfil the strain energy criterion and reduction of volume/mass following the selected constraint.

The topological optimization process is not a fully automated process requiring additional post-processing operations to complement the topology optimization, such as smoothness/material addition in critical areas to maintain the part integrity. The results of this process resulted in a new geometry with 12.53% of the initial mass increasing the stiffness/mass ratio in 596.74 %.

From the simulation of the building of the part by additive manufacturing, or more specifically, by SLM, the distortion in z direction of the three orientation parts converged for the different meshes since the differences between the results of the z-displacement tended to decrease as the mesh was refined.

The static analysis revealed a high peak of stresses (Von Mises) in the modelled fasteners and in the hole around the load point. The results associated with the fasteners are neglected since the chosen method doesn't take into account the pre-load of the fasteners and the contact between the different connection elements. This model was used in all of the stages of the project.

After this stage, the final geometry of the part was again submitted to the original load to evaluate the potential areas of fatigue failure. For these areas, the alternating stress ranges are calculated.If this component was manufactured by a traditional process, only these stresses were considered for the number of cycles to failure prediction.

The residual stresses related to the SLM process cause mean stresses effects that had to be taken into account. The alternating stresses and the mean stresses were correlated for different critical points. For most of the cases, and as it was expected the consideration of the mean stresses led to reduction of the fatigue life. However, for the critical point, with lower fatigue resistance (point 2), and taking into account the building orientation of the manufacturing process, the residual stresses appear as compressive stresses for the orientation 2, what increased the fatigue resistance in this point.

6.2 Future works

For future works it is interesting to consider the SN curve of the material obtained by AM.

Other interesting particularity is to consider different manufacturing strategies, besides the orientations already considered. Simulating the AM construction with different chamber, release and ambient temperatures is also important.

Model the contact between the fasteners and the part, using, if possible, the values of the pre-load is other possibility.

It is also important to simulate the same initial part, applying other load in other directions to view the differences in the topology optimization response as well as use a different algorithm for achieve a more sophisticated final geometry is very important to test. Different objective functions and restrictions, namely, stress and fatigue constraints are other considerable projects.

Full-scale cyclic tests to analyse the AM part produced are an idea to be implemented regarding this work.

Comparing the AM simulations results with other software which will provide a way to validate or benchmark the residual stresses computations.

7 References

[1] U. M. Dilberoglu, B. Gharehpapagh, U. Yaman, and M. Dolen, "The Role of Additive Manufacturing in the Era of Industry 4.0," *Procedia Manufacturing,* vol. 11, pp. 545-554, 2017.

[2] E. Holmberg, "Stress and fatigue constrained topology optimization,", Licentiate Thesis, Linköping Univeristy, 2013.

[3] S. Tripathy, C. Chin, T. London, U. Ankalkhope, and V. Oancea, *Process Modeling and Validation of Powder Bed Metal Additive Manufacturing*, NAFEMS World Congress 2017, pp. 11-14, 2017.

[4] C. Y. Yap *et al.*, *Review of selective laser melting: Materials and applications*, *Applied Physics Reveiws*, vol.2 (4), pp. 41-101 2015.

[5] L. Yang *et al.*, *Additive Manufacturing of Metals: The Technology, Materials, Design and Production*. Springer, pp. 168, ISBN 9783319551289, 2017.

[6] V. Bhavar, P. Kattire, V. Patil, S. Khot, K. Gujar, and R. Singh, "A review on powder bed fusion technology of metal additive manufacturing," in *Proceedings of the 4th International Conference and Exhibition on Additive Manufacturing Technologies-AM-2014, Bangalore, India*, 2014, pp. 1-2.

[7] T. Kurzynowski, E. Chlebus, B. Kuźnicka, and J. Reiner, "*Parameters in Selective Laser Melting for processing metallic powders*," in *High Power Laser Materials Processing: Lasers, Beam Delivery, Diagnostics and Applications,* vol. 8239, 2012.

[8] L. Zumofen, C. Beck, A. Kirchheim, and H.-J. Dennig, "*Quality Related Effects of the Preheating Temperature on Laser Melted High Carbon Content Steels*." in International Conference on Additive Manufacturing in Products and Applications, Springer, Cham, pp. 210-219, 2017.

[9] R. Mertens, B. Vrancken, N. Holmstock, Y. Kinds, J.-P. Kruth, and J. Humbeeck, "Influence of Powder Bed Preheating on Microstructure and Mechanical Properties of H13 Tool Steel SLM Parts.", *Physics Procedia* vol. 83, pp. 882-890, 2016.

[10] I. Yadroitsev, P. Krakhmalev, and I. Yadroitsava, "Selective laser melting of Ti6Al4V alloy for biomedical applications: Temperature monitoring and microstructural evolution," *Journal of Alloys and Compounds,* vol. 583, pp. 404-409, 2014.

[11] R. Li, J. Liu, Y. Shi, L. Wang, and W. Jiang, "Balling behavior of stainless steel and nickel powder during selective laser melting process," *The International Journal of Advanced Manufacturing Technology,* vol. 59 (9), pp. 1025-1035, 2012.

[12] C. Li, J. F. Liu, and Y. B. Guo, "Prediction of Residual Stress and Part Distortion in Selective Laser Melting," *Procedia CIRP,* vol. 45, pp. 171-174, 2016.

[13] A. M. Mirzendehdel and K. Suresh, "Support structure constrained topology optimization for additive manufacturing," *Computer-Aided Design,* vol. 81, pp. 1-13, 2016.

[14] C. J. Smith, I. Todd, and M. Gilbert, "Utilizing additive manufacturing techniques to fabricate weight optimized components designed using structural optimization methods.", in *Solid Free. Fabr. Symp.* pp. 879-894, 2013.

[15] B. Schoinochoritis, D. Chantzis, and K. Salonitis, "Simulation of metallic powder bed additive manufacturing processes with the finite element method: A critical review." *Proceedings of the Instituiton of Mechanical Engineers, Part B: Journal of Engineering Manufacture,* vol.23(1), pp 96-117, 2017.

[16] C. R. Fisher and C. E. Vail, "Computational Simulation of an Additively Manufactured Marine Component," *Journal of Materials Engineering and Performance,* vol. 28(2), pp. 627-632, 2019.

[17] M. Gouge, P. Michaleris, E. Denlinger, and J. Irwin, "Chapter 2 - The Finite Element Method for the Thermo-Mechanical Modeling of Additive Manufacturing Processes," in *Thermo-Mechanical Modeling of Additive Manufacturing*, M. Gouge and P. Michaleris, Eds.: Butterworth-Heinemann, pp. 19-38. , 2018.

[18] C. R. Fisher and C. E. Vail, "Computational Simulation of an Additively Manufactured Marine Component," *Journal of Materials Engineering and Performance,* journal article vol. 28(2), pp. 627-632, 2019.

[19] J. Cao, M. A. Gharghouri, and P. Nash, "Finite-element analysis and experimental validation of thermal residual stress and distortion in electron beam additive manufactured Ti-6Al-4V build plates," *Journal of Materials Processing Technology,* vol. 237, pp. 409-419, 2016.

[20] T. M. Rodgers, J. D. Madison, and V. Tikare, "Simulation of metal additive manufacturing microstructures using kinetic Monte Carlo," *Computational Materials Science,* vol. 135, pp. 78-89, 2017.

[21] P. W. Christensen and A. Klarbring, "An introduction to structural optimization." Springer Science & Business Media, vol.153, ISBN 140286652, 2008.

[22] L. Rosenblad and F. Hallbäck, "Low Cycle Fatigue Weld Optimization using Chaboche Material Model,", Master Thesis, KTH School of Engineering Sciences, Stockohlm, 2018.

[23] M. Grujicic *et al.*, "Application of Topology, Size and Shape Optimization Methods in Polymer Metal Hybrid Structural Lightweight Engineering." *Multidiscipline modeling in Materials and Structures,* vol.4 (4), pp 305-330, 2008.

[24] R. T. Haftka and R. V. Grandhi, "Structural shape optimization—A survey," *Computer Methods in Applied Mechanics and Engineering,* vol. 57(1), pp. 91-106, 1986.

[25] R. Larsson, "Methodology for Topology and Shape Optimization: Application to a Rear Lower Control Arm,", Master Thesis, *CHALMERS UNIVERSITY OF TECHNOLOGY, Goteborg,* 2016.

[26] M. P. Bendsøe and O. Sigmund, "Topology Optimization - Theory, Methods, and Applications." Berlin Heidelberg: Springer Verlag, ISBN 3-540-42992-1, 2003.

[27] G. I. N. Rozvany and N. Olhoff, *Topology Optimization of Structures and Composite Continua*. , vol. 7, Springer Netherlands, ISBN 9780792368076, 2001.

[28] I. Ferguson, "Using Topology Optimization to Improve Design for Additive Manufacture," , Master thesis, Pennsilvanya State University, Pennsilvanya, 2015.

[29] N. Taillieu, S. c. Jacques, and W. p. Van Paepegem, "A topology optimization framework for additively manufactured materials under mechanical load," Master Thesis, Universiteit Gent, Gent, 2016.

[30] J. Liu and Y. Ma, "A survey of manufacturing oriented topology optimization methods," *Advances in Engineering Software,* vol. 100, pp. 161-175, 2016.

[31] R. Cazacu and L. Grama, "Overview of structural topology optimization methods for plane and solid structures," *Annals of the University of Oradea, Fascicle of Management and Technological Engineering,* pp. 1583-0691, 2014.

[32] K. A. James, G. J. Kennedy, and J. R. R. A. Martins, "Concurrent aerostructural topology optimization of a wing box," *Computers & Structures,* vol. 134, pp. 1-17, 2014.

[33] K. K. Choi and N.-H. Kim, *Structural sensitivity analysis and optimization 1: linear systems*. Springer Science & Business Media, ISBN 0387271694 2006.

[34] E. F. Moreira, "Application of Topology Optimization to Satellite Tertiary Structures,", Master Thesis, Instituto Superior Técnico, Lisboa, 2016.

[35] O. Sigmund, "On the Design of Compliant Mechanisms Using Topology Optimization," *Mechanics of Structures and Machines,* vol. 25(4), pp. 493-524, 1997.

[36] O. Sigmund, "Morphology-based black and white filters for topology optimization," *Structural and Multidisciplinary Optimization,* journal article vol. 33(4), pp. 401-424, 2007.

[37] E. Andreassen, A. Clausen, M. Schevenels, B. S. Lazarov, and O. Sigmund, "Efficient topology optimization in MATLAB using 88 lines of code," *Structural and Multidisciplinary Optimization,* journal article vol. 43(1), pp. 1-16, 2011.

[38] S.-B. Hu, L.-P. Chen, Y.-Q. Zhang, J. Yang, and S.-T. Wang, "A crossing sensitivity filter for structural topology optimization with chamfering, rounding, and checkerboard-free patterns," *Structural and Multidisciplinary Optimization,* journal article vol. 37(5), pp. 529-540, 2009.

[39] S. Wang, K. Lim, B. Khoo, and M. Wang, "A hybrid sensitivity filtering method for topology optimization," *COMPUTER MODELING IN ENGINEERING AND SCIENCES,* vol. 24, no. 1, p. 21, 2008.

[40] A. Tovar and K. Khandelwal, "Uniqueness in linear and nonlinear topology optimization and approximate solutions," in *Proceedings of the 2nd International Conference on Engineering Optimization (EngOpt 2010), Lisbon, Portugal*, 2010.

[41] S. Ananiev, "On Equivalence Between Optimality Criteria and Projected Gradient Methods with Application to Topology Optimization Problem," *Multibody System Dynamics,* journal article vol. 13(1), pp. 25-38, 2005.

[42] D. Fujii, K. Suzuki, and H. Ohtsubo, "TOPOLOGY OPTIMIZATION OF FRAME STRUCTURES USING CONLIN OPTIMIZER." *Journal of Structural and Construction Engineering, vol. 66*, pp. 59-66, 2001.

[43] K. Svanberg, "A class of globally convergent optimization methods based on conservative convex separable approximations," *SIAM journal on optimization,* vol. 12(2), pp. 555-573, 2002.

[44] M. Fanni, N. Shabara, and M. Alkalla, "A Comparison Between Different Topology Optimization Methods." *Mansoura Engineering Journal*, vol.38(1), 2013.

[45] O. Sigmund and J. Petersson, "Numerical instabilities in topology optimization: A survey on procedures dealing with checkerboards, mesh-dependencies and local minima," *Structural optimization,* journal article vol. 16 (1), pp. 68-75, 1998.

[46] A. Díaz and O. Sigmund, "Checkerboard patterns in layout optimization," *Structural optimization,* journal article vol. 10(1), pp. 40-45, 1995.

[47] M. Wang and X. Qian, "Efficient filtering in topology optimization via B-splines," *Journal of Mechanical Design,* vol. 137(3), pp. 031402, 2015.

[48] M. Stolpe and K. Svanberg, "On the trajectories of penalization methods for topology optimization," *Structural and Multidisciplinary Optimization,* journal article vol. 21(2), pp. 128-139, 2001.

[49] J. D. Deaton and R. V. Grandhi, "A survey of structural and multidisciplinary continuum topology optimization: post 2000," *Structural and Multidisciplinary Optimization,* journal article vol. 49(1), pp. 1-38, 2014.

[50] Y. Saadlaoui, J.-L. Milan, J.-M. Rossi, and P. Chabrand, "*Topology optimization and additive manufacturing: Comparison of conception methods using industrial codes*." Journal of Manufacturing Systems, vol.43, pp.178-186, 2017.

[51] N. Mavrodontis, "Fatigue analysis with fe-safe," https://info.simuleon.com/blog/fatigue-analysis-with-fe-safe , 2019. Accessed in: 27/04/2019

[52] C. M. Sonsino and K. Dieterich, "Fatigue design with cast magnesium alloys under constant and variable amplitude loading," *International Journal of Fatigue,* vol. 28(3), pp. 183-193, 2006.

[53] K. Nabaki, J. Shen, and X. Huang, "Evolutionary topology optimization of continuum structures considering fatigue failure," *Materials & Design,* vol. 166, pp. 107586, 2019.

[54] V. Neelakandan, A. Jha, S. Rao P V, J. Hardikar, "Importance of Fatigue Life in Design Optimisation of Off-highway Powershift Transmission system.", *Journal of Materials Science and Surface Engineering,* vol.3(1), pp. 195-201, 2015.

[55] Y.-S. Lee, J. A. González, J. H. Lee, Y. I. Kim, K. C. Park, and S. Han, "Structural topology optimization of the transition piece for an offshore wind turbine with jacket foundation," *Renewable Energy,* vol. 85, pp. 1214-1225, 2016.

[56] R. I. Stephens, A. Fatemi, R. R. Stephens, and H. O. Fuchs, *Metal fatigue in engineering*. John Wiley & Sons, 2nd edition, ISBN 0471510599, 2000.

[57] F. Dirksen, M. Anselmann, T. I. Zohdi, and R. Lammering, "Incorporation of flexural hinge fatigue-life cycle criteria into the topological design of compliant small-scale devices," *Precision Engineering,* vol. 37(3), pp. 531-541, 2013.

[58] O. J. Horger and A. S. o. M. Engineers, *Metals Engineering Design: ASME Handbook*. McGraw-Hill, ISBN 007001518, 1953.

[59] P. P. Milella, *Fatigue and corrosion in metals*. Springer Science & Business Media, 1st edition, ISBN 978-88-470-2336-9, 2012.

[60] J. Grunwald and E. Schnack, "Modeling fatigue for shape optimization of dynamically loaded parts," *Advances in Engineering Software,* vol. 29(1), pp. 63-67, 1998.

[61] M. Mrzyglod and A. P. Zielinski, "Parametric structural optimization with respect to the multiaxial high-cycle fatigue criterion," *Structural and Multidisciplinary Optimization,* journal article vol. 33(2), pp. 161-171, 2007.

[62] N. Kaya, İ. Karen, and F. Öztürk, "Re-design of a failed clutch fork using topology and shape optimisation by the response surface method," *Materials & Design,* vol. 31(6), pp. 3008-3014, 2010.

[63] H. Svärd, "Using the weakest link model of fatigue in topology optimization", Doctoral Thesis, KTH School of Engineering Sciences, 2015.

[64] M. Collet, M. Bruggi, and P. Duysinx, "Topology optimization for minimum weight with compliance and simplified nominal stress constraints for fatigue resistance," *Structural and Multidisciplinary Optimization,* journal article vol. 55(3), pp. 839-855, 2017.

[65] H. Svärd, "A branch and bound algorithm for evaluation of the Findley fatigue criterion," *International Journal of Fatigue,* vol. 73, pp. 27-38, 2015.

[66] E. Holmberg, B. Torstenfelt, and A. Klarbring, "Fatigue constrained topology optimization," *Structural and Multidisciplinary Optimization,* journal article vol. 50(2), pp. 207-219, 2014.

[67] S. H. Jeong, D.-H. Choi, and G. H. Yoon, "Fatigue and static failure considerations using a topology optimization method," *Applied Mathematical Modelling,* vol. 39(3), pp. 1137-1162, 2015.

[68] J. Kranz, "Methodik und Richtlinien für die Konstruktion von laseradditiv gefertigten Leichtbaustrukturen.", Springer Vieweg, ISBN 978-3-662-55339-8, 2017.

[69] P. Sander, "On the way to Additive Manufacturing " in *World PM2016 congress and exhibition*, Airbus, 2018.

[70] S. Roy, S. Goyal, R. Sandhya, and S. K. Ray, "Low cycle fatigue life prediction of 316 L(N) stainless steel based on cyclic elasto-plastic response.", Nuclear Engineering and Design, vol.253 pp. 219–225, 2012.

[71] D. Angelova, Y. Rozina, and T. Lazarova, "On factors influencing fatigue process in steel 316L used in hydrogen energy technologies.", *Journal of Chemical Technology and Metalurgy,* vol.49(1), pp. 29-34, 2014.

[72] A. Korolija, "FE modeling of bolted joints in structures", Master Thesis, Linsköpings Universitet, Linsköpings, 2012.

[73] "Fastener modelling in Nastran" , https://www.aerospacengineering.net/fastener-modelling-in-nastran/, 2013. Accessed in: 07/03/2019

[74] E. Adolfsson, "Simplified finite element bearing modeling: with NX Nastran," ed, 2015.

[75] S. Johnsen, "Structural topology optimization: basic theory, methods and applications," Institutt for produktutvikling og materialer, 2013.

[76] Ansys. (2017). *Topology Optimization R18.0 Feature and Usage Highlights: Additive Manufacturing Application*. Available: https://www.fluidcodes.com/archives/products/1489307672Topology%20Optimization%20180%20Features.pdf . Accessed in: 26/04/2019

[77] Autodesk, "Smooth Triangles,", https://knowledge.autodesk.com/support/netfabb/learn-explore/caas/CloudHelp/cloudhelp/2017/ENU/NETF/files/GUID-522C37A2-BACA-4268-99F2-5C55C99AB1FF-htm.html?fbclid=IwAR1k_EgsKjJqGGOYLnWBfWQ2sc_srbF_-Oi5POCWU2AO30j3-7DmZu2_YEY . Accessed in: 18/04/2019

[78] Autodesk. Refine Triangle Mesh [Online]. Available: https://knowledge.autodesk.com/support/netfabb/learnexplore/caas/CloudHelp/cloudhelp/2017/ENU/NETF/files/GUID-9C810B5A-6711-4F02-B4BD-19EC2EC48962-htm.html .Accessed in: 18/04/2019

[79] C. Körner, E. Attar, and P. Heinl, "Mesoscopic simulation of selective beam melting processes," *Journal of Materials Processing Technology,* vol. 211(6), pp. 978-987, 2011.

[80] S. H. Jeong, S. H. Park, D.-H. Choi, and G. H. Yoon, "Toward a stress-based topology optimization procedure with indirect calculation of internal finite element information," *Computers & Mathematics with Applications,* vol. 66(6), pp. 1065-1081, 2013.

[81] D. Xie *et al.*, "Assumption of Constraining Force to Explain Distortion in Laser Additive Manufacturing," (in eng), *Materials (Basel),* vol. 11(11), 2018.

[82] M. Fischer, D. Joguet, G. Robin, L. Peltier, and P. Laheurte, "In situ elaboration of a binary Ti-26Nb alloy by selective laser melting of elemental titanium and niobium mixed powders," (in eng), *Mater Sci Eng C Mater Biol Appl,* vol. 62, pp. 852-9, 2016.

[83] K. V. Praet, "Tips and Tricks for Metal 3D Printing: Recoaters," 2017, https://www.materialise.com/en/blog/metal-3D-printing-recoaters . Accessed in: 15/06/2019

[84] M. Caelers, "Study of in-situ monitoring methods to create a robust SLM process: Preventing collisions between recoater mechanism and part in a SLM machine," Master Thesis, KTH Royal Institute of Technology, Stockholm, ed, 2017.

[85] G. Sines, "Behavior of Metals Under Complex Static and Alternating Stresses", *Metal Fatigue*, Eds. McGraw Hill, New York,1959.

APPENDICES

Appendix A: Stress and deformation Results of Topology optimization

The results of the topology optimization is presented in this section. In figure 68 it is shown the deformation distribution of the part. The upper part of the ring have the highest displacements.

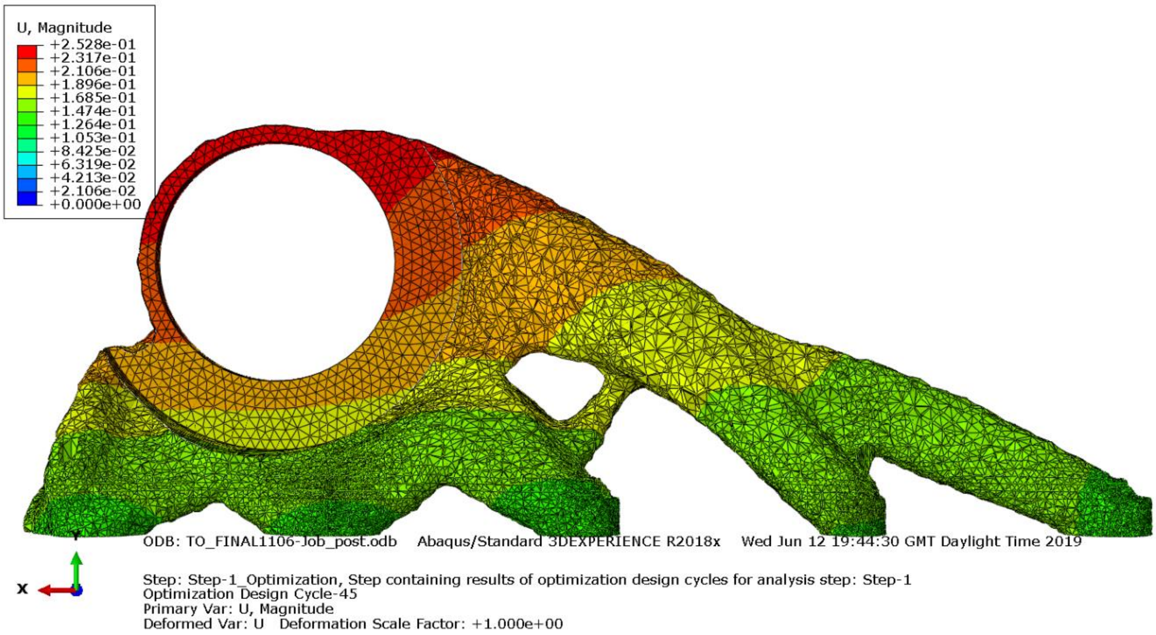

```
ODB: TO_FINAL1106-Job_post.odb    Abaqus/Standard 3DEXPERIENCE R2018x    Wed Jun 12 19:44:30 GMT Daylight Time 2019

Step: Step-1_Optimization, Step containing results of optimization design cycles for analysis step: Step-1
Optimization Design Cycle-45
Primary Var: U, Magnitude
Deformed Var: U   Deformation Scale Factor: +1.000e+00
```

Figure 68 - Deformation results of topology optimization

In figure 69 it is presented the Von Mises stress distribution where it is possible to verify higher stress around the hole.

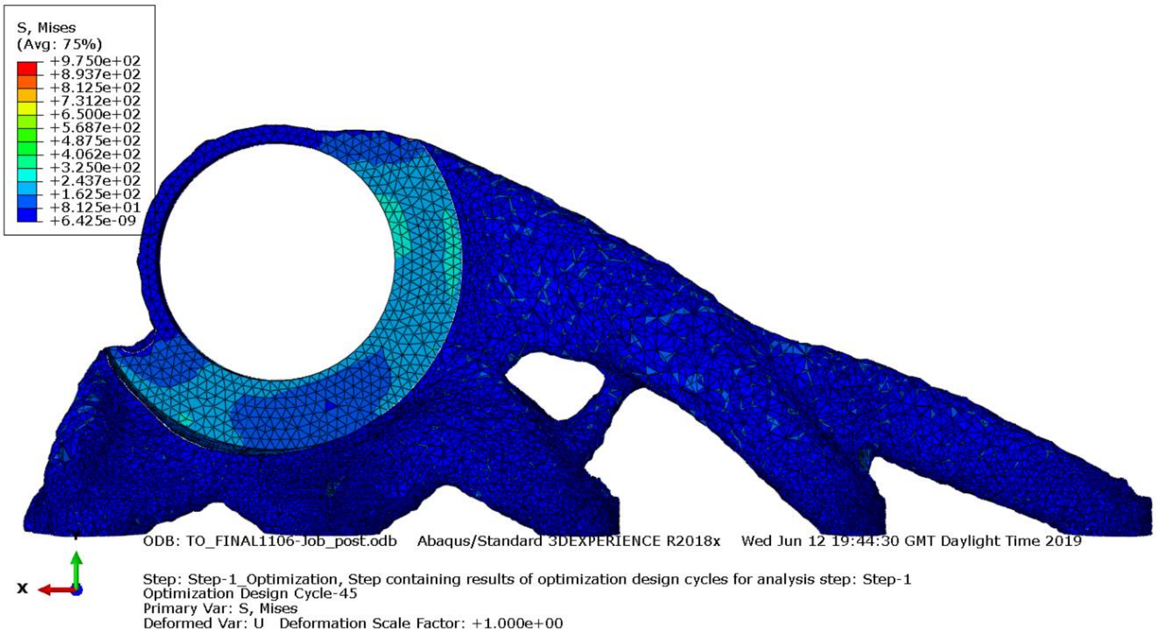

```
ODB: TO_FINAL1106-Job_post.odb    Abaqus/Standard 3DEXPERIENCE R2018x    Wed Jun 12 19:44:30 GMT Daylight Time 2019

Step: Step-1_Optimization, Step containing results of optimization design cycles for analysis step: Step-1
Optimization Design Cycle-45
Primary Var: S, Mises
Deformed Var: U   Deformation Scale Factor: +1.000e+00
```

Figure 69 - Von Mises stress distribution results of topology optimization

APPENDIX B: Intermedial Results of Mises, S_{xx}, S_{yy} and S_{zz}

The results shown in this section were obtained for an intermedial geometry very similar to the final geometry. Only the values of stage 1 and 3 are presented since the effects of the part emotion from the machine are not significant. The results are shown in Figures 70, 71 and 72.

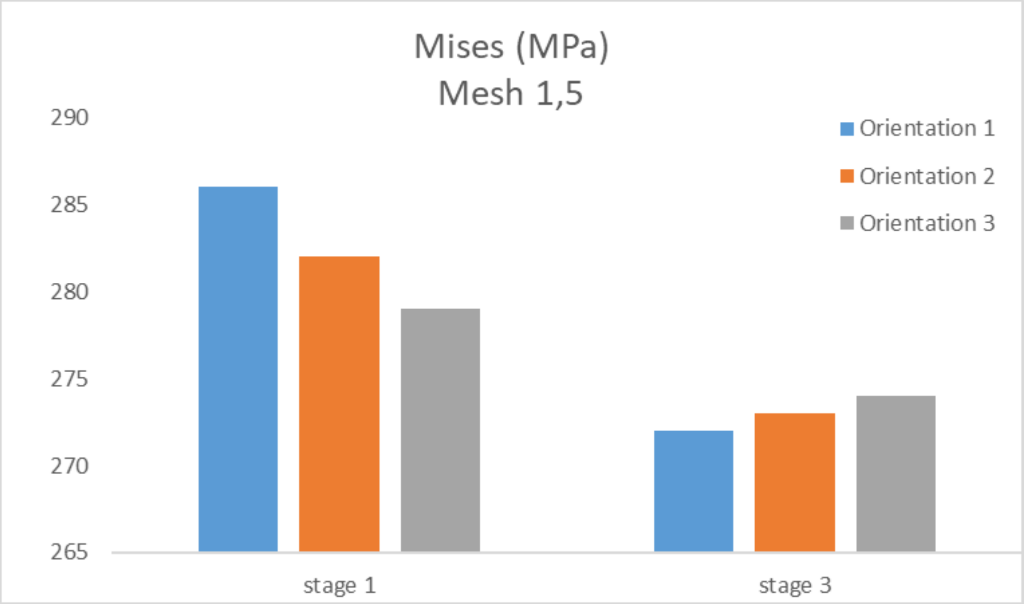

Figure 70 -Von Mises maximum stress value for mesh 1.5, for each orientation and for stage 1 and 3

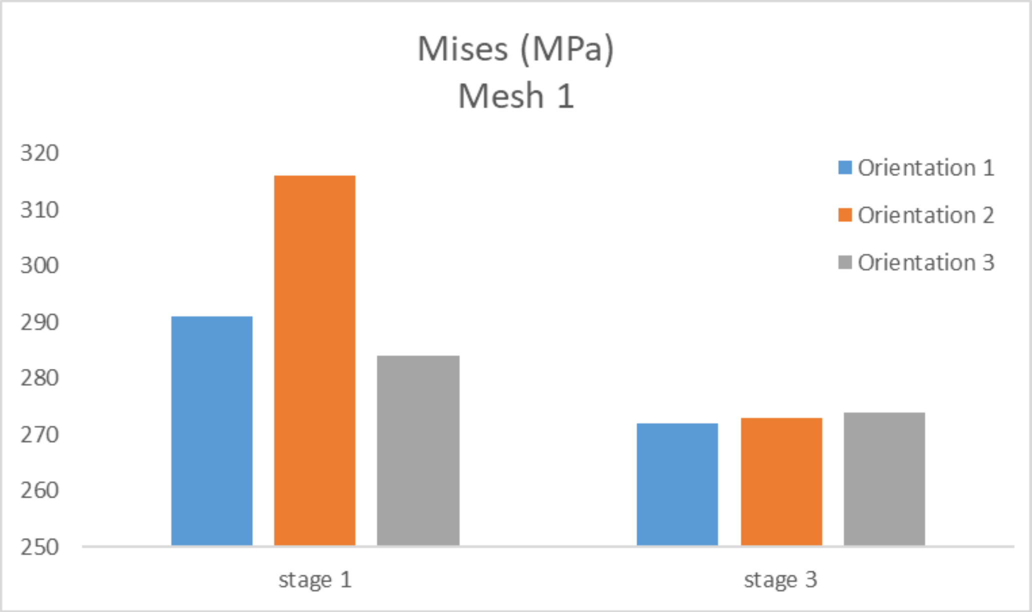

Figure 71 -Von Mises maximum stress value for mesh 1, for each orientation and for stage 1 and 3

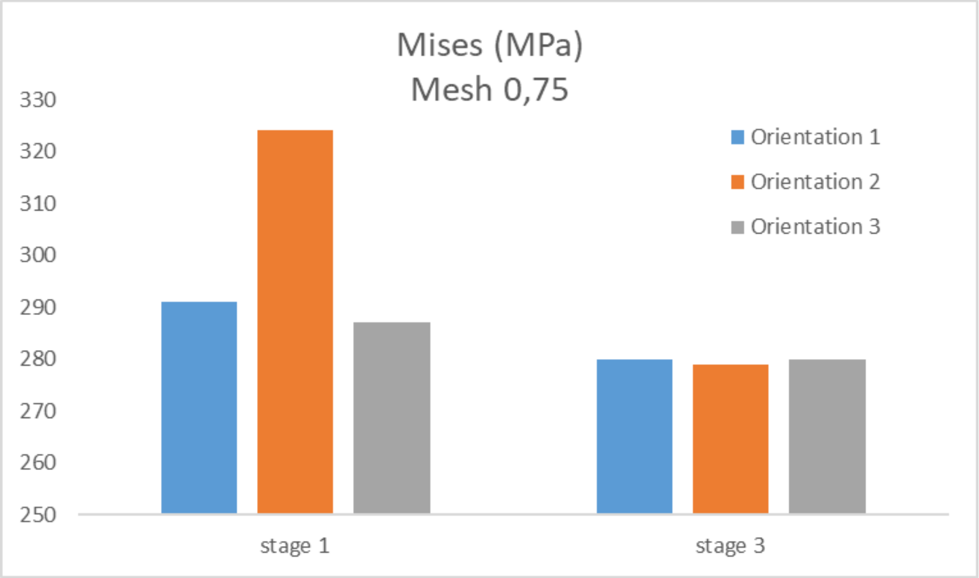

Figure 72-Von Mises maximum stress value for mesh 0.75, for each orientation and for stage 1 and 3

The results of the maximum and minimum S_{xx} for each mesh, orientation and for stages 1 and 3 are presented in Figures 73,74 and 75.

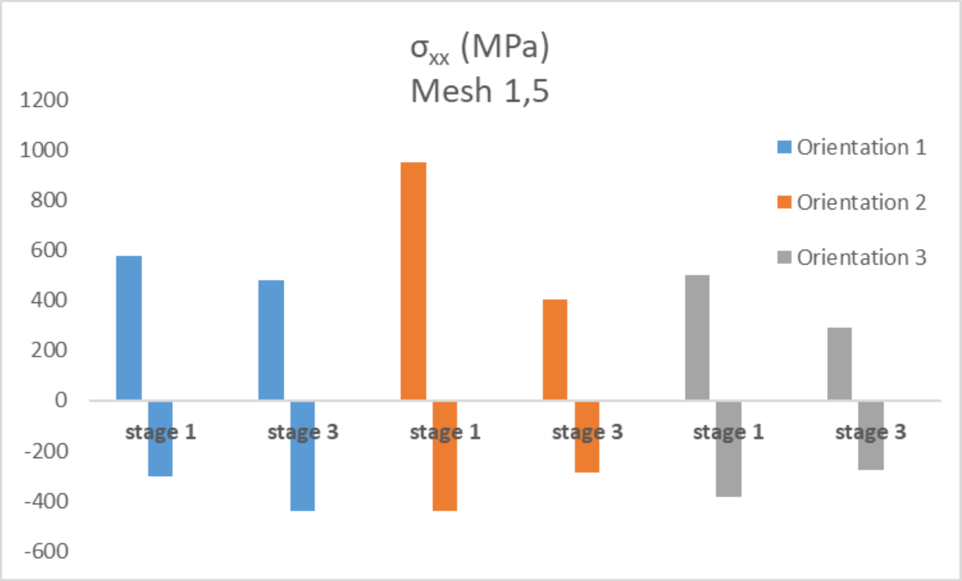

Figure 73 – S_{xx} maximum and minimum stress value for mesh 1.5, for each orientation and for stage 1 and 3

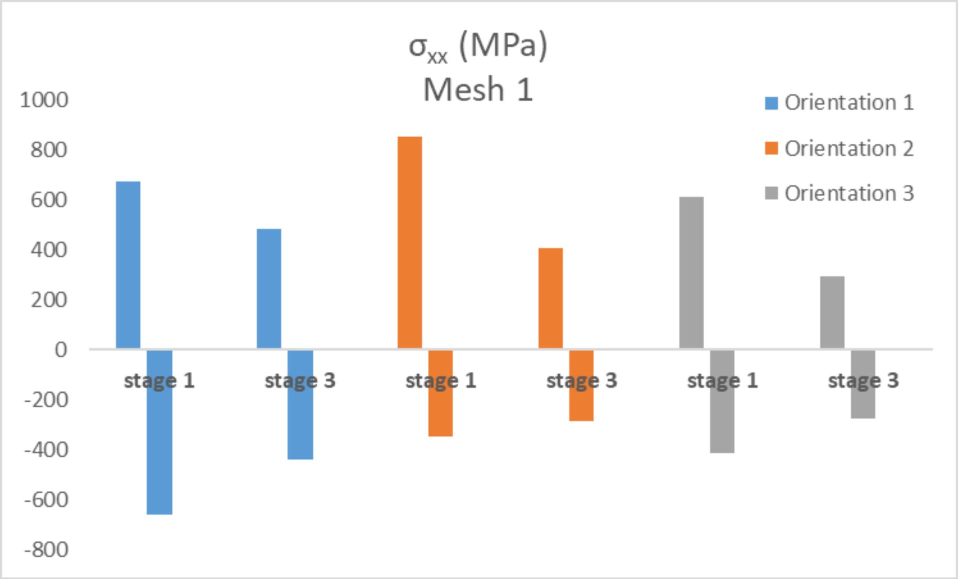

Figure 74 - Sxx maximum and minimum stress value for mesh 1, for each orientation and for stage 1 and 3

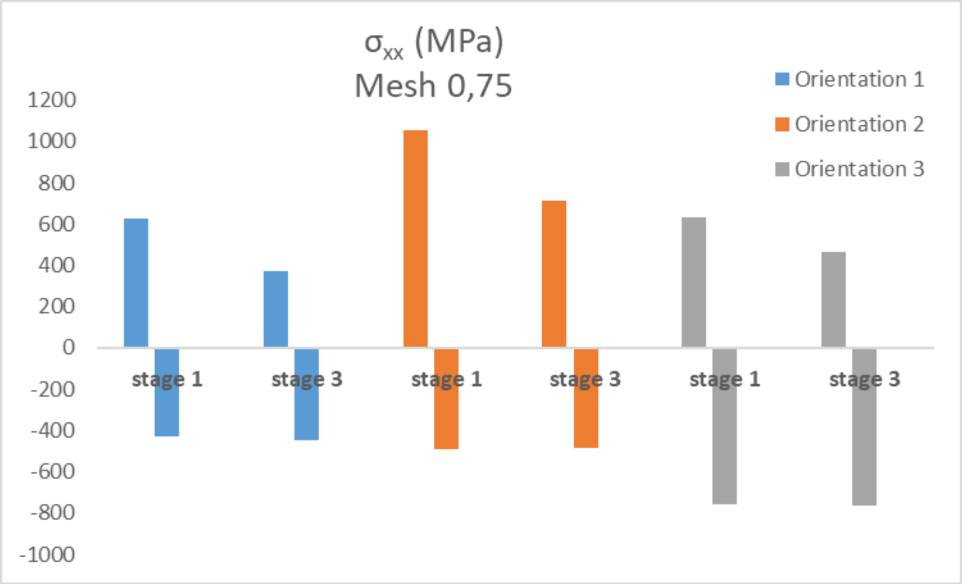

Figure 75 - Sxx maximum and minimum stress value for mesh 0.75, for each orientation and for stage 1 and 3

The results of the maximum and minimum S_{yy} for each mesh, orientation and for stages 1 and 3 are presented in Figures 76,77 and 78.

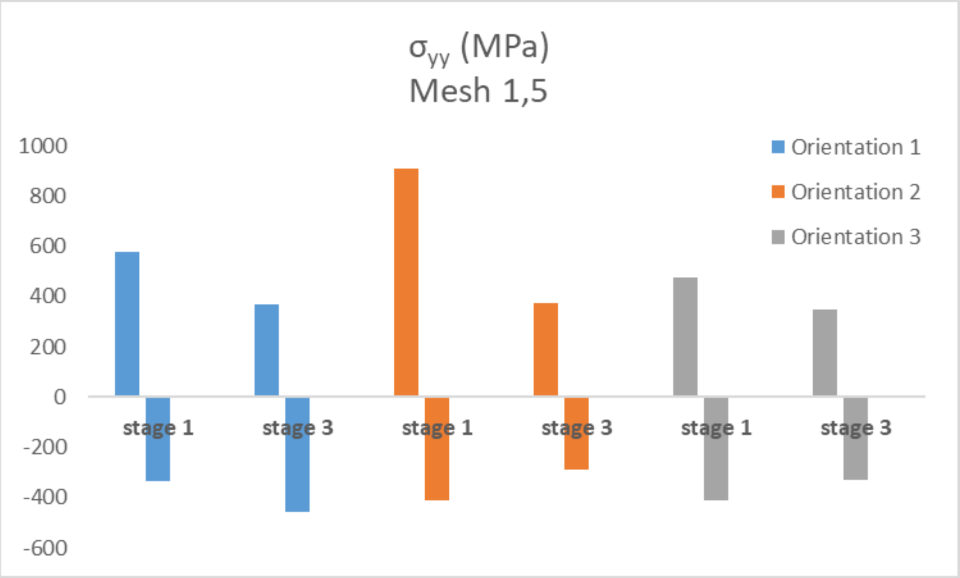

Figure 76 - Syy maximum and minimum stress value for mesh 1.5, for each orientation and for stage 1 and 3

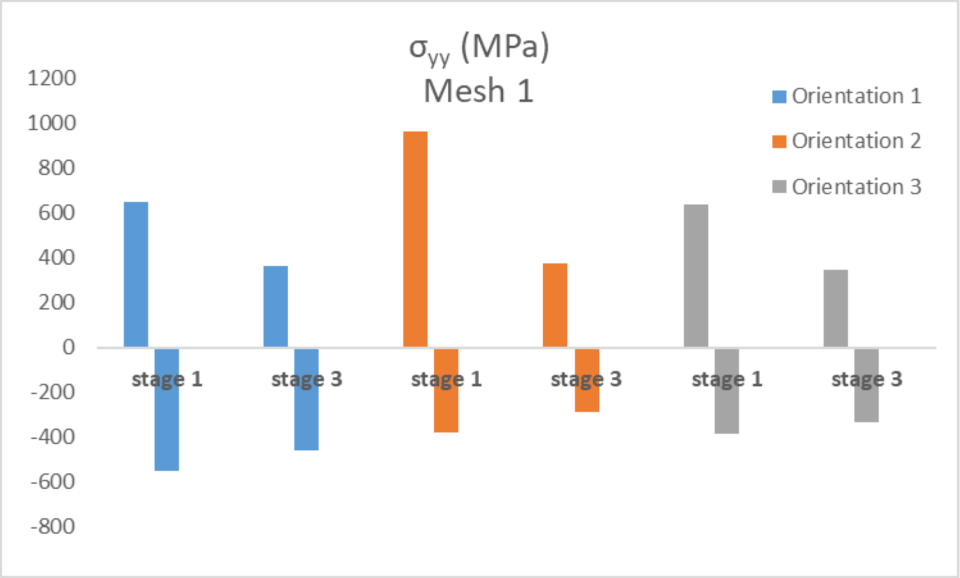

Figure 77 - Syy maximum and minimum stress value for mesh 1, for each orientation and for stage 1 and 3

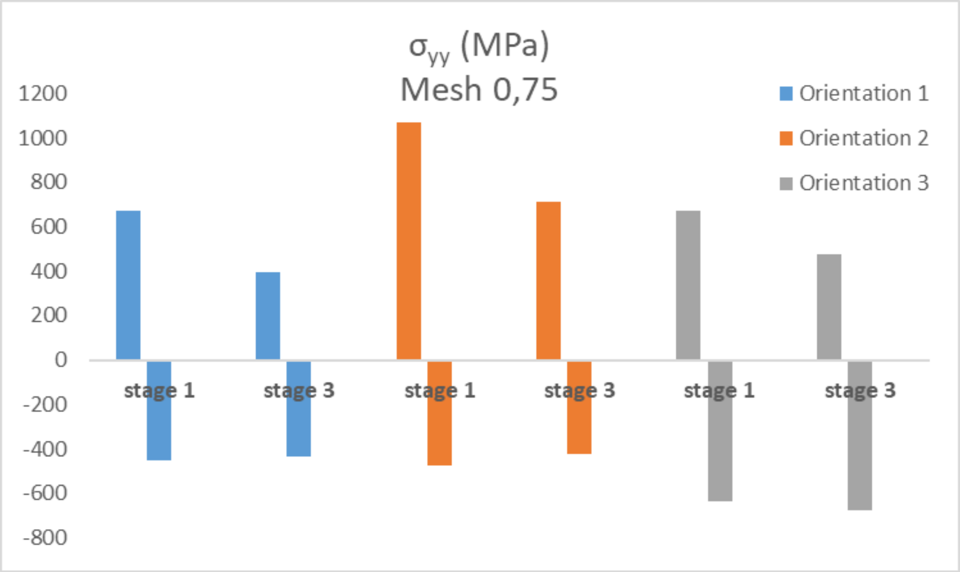

Figure 78 - Syy maximum and minimum stress value for mesh 0.75, for each orientation and for stage 1 and 3

The results of the maximum and minimum S_{zz} for each mesh, orientation and for stages 1 and 3 are presented in Figures 79,80 and 81.

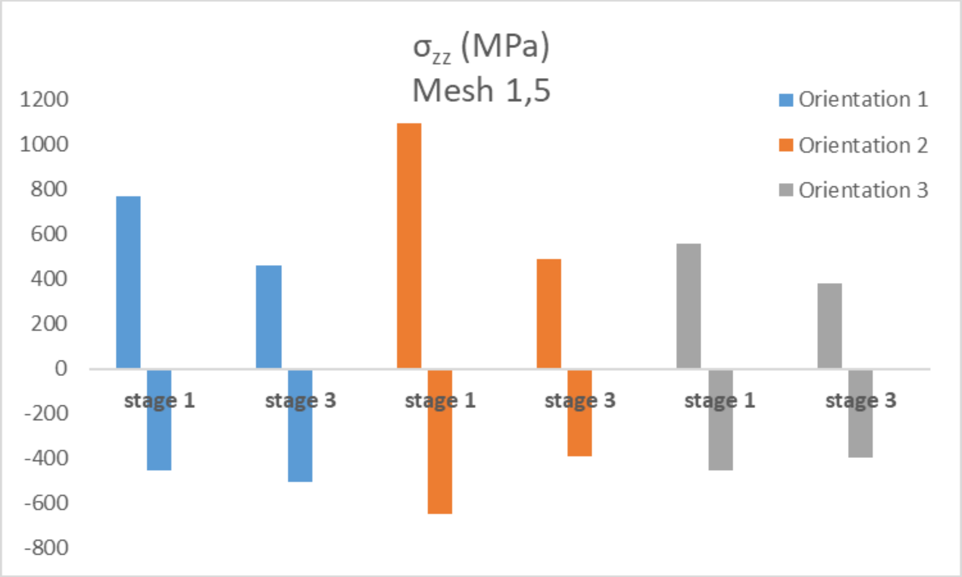

Figure 79 - Szz maximum and minimum stress value for mesh 1.5, for each orientation and for stage 1 and 3

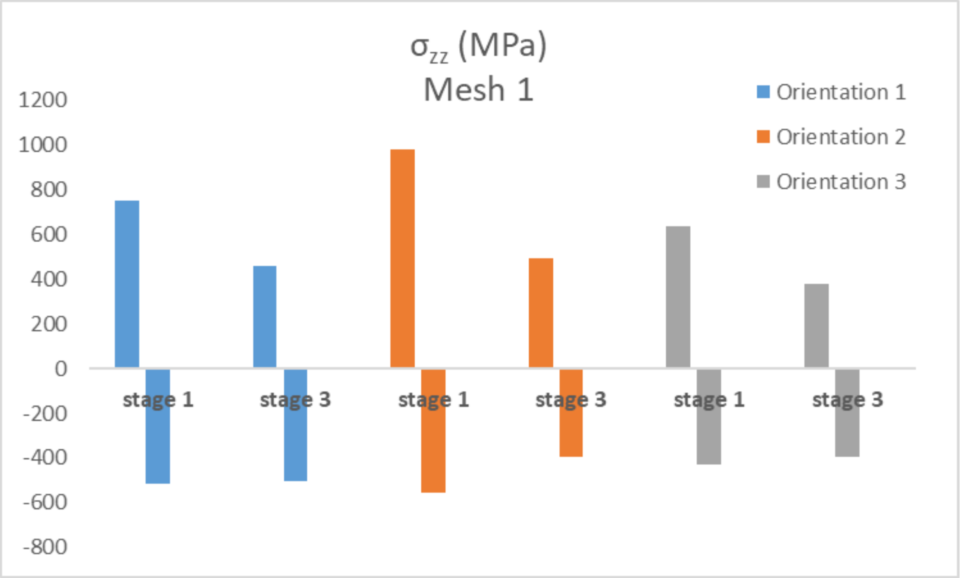

Figure 80 - Szz maximum and minimum stress value for mesh 1, for each orientation and for stage 1 and 3

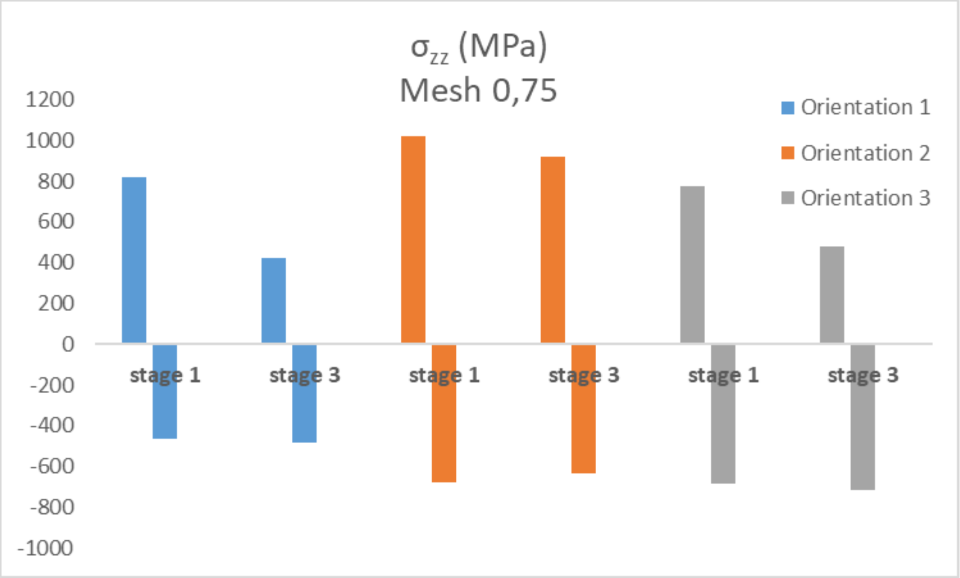

Figure 81 - Szz maximum and minimum stress value for mesh 0.75, for each orientation and for stage 1 and 3

APPENDIX C : FATIGUE RESULTS

The figure 82 gives a wide result of fatigue resistance for every point from every build orientation.

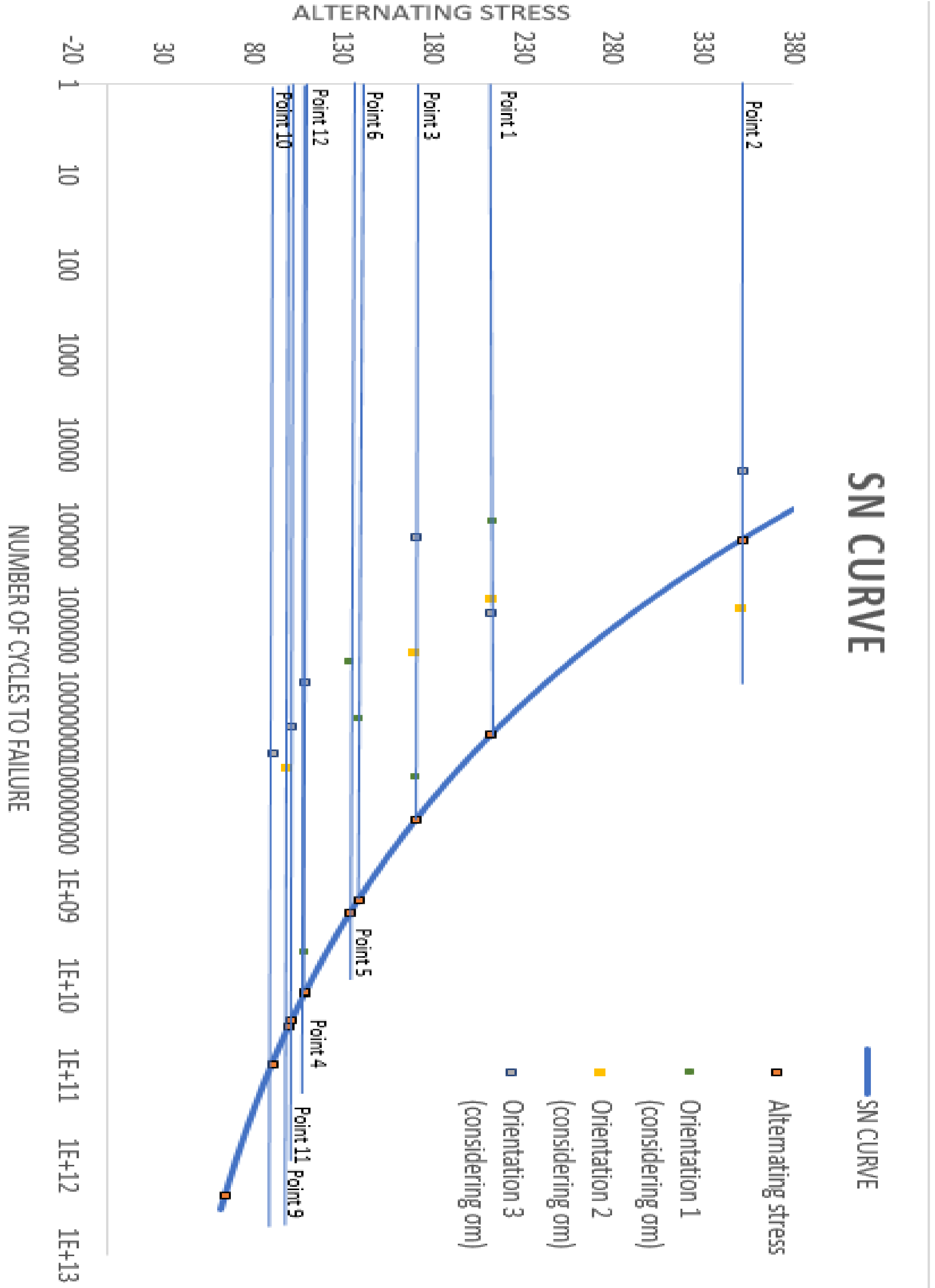

Figure 82 - Results of fatigue resitance